

South Dakota State University

# Open PRAIRIE: Open Public Research Access Institutional Repository and Information Exchange

---

Electronic Theses and Dissertations

---

2023

## Electrode and Electrolyte Design to Develop Advanced Battery Technologies for Large Scale Energy Storage

Wei He

South Dakota State University, hwdml@outlook.com

Follow this and additional works at: <https://openprairie.sdstate.edu/etd2>



Part of the [Power and Energy Commons](#)

---

### Recommended Citation

He, Wei, "Electrode and Electrolyte Design to Develop Advanced Battery Technologies for Large Scale Energy Storage" (2023). *Electronic Theses and Dissertations*. 612.

<https://openprairie.sdstate.edu/etd2/612>

This Dissertation - Open Access is brought to you for free and open access by Open PRAIRIE: Open Public Research Access Institutional Repository and Information Exchange. It has been accepted for inclusion in Electronic Theses and Dissertations by an authorized administrator of Open PRAIRIE: Open Public Research Access Institutional Repository and Information Exchange. For more information, please contact [michael.biondo@sdstate.edu](mailto:michael.biondo@sdstate.edu).

ELECTRODE AND ELECTROLYTE DESIGN TO DEVELOP ADVANCED  
BATTERY TECHNOLOGIES FOR LARGE SCALE ENERGY STORAGE

BY

WEI HE

A dissertation submitted in partial fulfillment of the requirements for the

Doctor of Philosophy

Major in Electrical Engineering

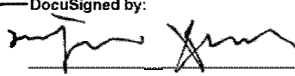
South Dakota State University

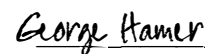
2023

DISSERTATION ACCEPTANCE PAGE

Wei He

This dissertation is approved as a creditable and independent investigation by a candidate for the Doctor of Philosophy degree and is acceptable for meeting the dissertation requirements for this degree. Acceptance of this does not imply that the conclusions reached by the candidate are necessarily the conclusions of the major department.

DocuSigned by:  
  
30DE3BA8C5E5409...  
Xiaojun Xian  
Advisor  
4/14/2023 | 14:27 CDT  
Date

DocuSigned by:  
  
E4BDFD86E9C94D0...  
George Hamer  
Department Head  
4/15/2023 | 07:01 PDT  
Date

DocuSigned by:  
  
E3BEAA596D57438...  
Nicole Lounsbery, PhD  
Director, Graduate School  
4/15/2023 | 15:51 CDT  
Date

## ACKNOWLEDGEMENTS

First and foremost, I would like to express my deepest gratitude to my advisors, Dr. Yue Zhou and Dr. Xiaojun Xian, who support throughout my PhD studies. Their unwavering dedication, passion, and guidance have been invaluable in shaping my research and my academic journey. I would also like to thank the committee members of Dr. Parashu Kharel and Dr. Ryan Samuel for their insightful feedback, constructive criticism, and their time and effort invested in my dissertation.

I would like to acknowledge the financial support from the Ph.D. program in the Department of EECS at SDSU, NSF (ECCS- 2144708, CBET- 2038082 and CBET- 2038083), South Dakota Governor's Research Center and EDA University Center Program (ED18DEN3030025).

I would like to express my appreciation to my research group members of Dr. Ke Chen, Dr. Pathak, Rajesh, Jyotshna Pokharel, Buddhi Sagar Lamsal, Yuhe Mu and Zhongjiu Yang. They have been my companions throughout my journey. I am grateful for their support, encouragement, and enthusiasm for science, which have kept me motivated and driven to excel. I want to thank Yao Ren for assisting me with the DFT calculation.

I want to thank my parent of Jiasheng He and Taorong Xu and my sister Ningning He for their unwavering love, support, and encouragement. Their sacrifices, understanding, and patience have been my driving force, and without them, this achievement would not have been possible. I would like to extend a special thank you to my beautiful wife, Mengling Ding, and my daughter, Claire He, who have been a constant source of love and support throughout my PhD studies.

## CONTENTS

LIST OF FIGURES .....	viii
LIST OF TABLES .....	xvii
ABSTRACT.....	xviii
Chapter 1 Introduction: sodium-ion batteries and aqueous zinc-ion batteries.....	1
1.1 Background.....	1
1.2 Sodium-ion batteries .....	5
1.2.1 A brief history of SIBs.....	5
1.2.2 Working principle of SIBs.....	8
1.2.3 The challenges of SIBs .....	9
1.2.4 Recent advances in the high-performance anodes.....	11
1.3 Aqueous zinc-ion batteries.....	17
1.3.1 A brief history of AZIBs.....	17
1.3.2 Working principle of AZIBs.....	18
1.3.3 The challenges of AZIBs .....	20
1.3.4 Recent advances in the electrolyte additives .....	21
1.4 Motivation and objectives.....	24
1.4.1 Motivation.....	24
1.4.2 Objectives and outline.....	24
Chapter 2 Experimental procedures.....	27

2.1 Materials and preparation .....	27
2.1.1 Preparation of the Free-Standing Sn@CFC electrode .....	27
2.1.2 Synthesis of SnP <sub>2</sub> O <sub>7</sub> @C .....	28
2.1.3 Preparation of SnS/Sb <sub>2</sub> S <sub>3</sub> @SNC.....	29
2.1.4 Preparation of the electrolyte for AZIBs .....	30
2.2 Electrochemical measurements.....	30
2.2.1 Anode electrode fabrication for SIBs.....	30
2.2.2 Cell assembly and testing for SIBs .....	30
2.2.3 Cell assembly and testing for AZIBs .....	31
2.3 Material characterizations.....	31
2.4 Density functional theory simulations .....	32
Chapter 3 Material Engineering of the Sn-based anodes for sodium-ion batteries .....	33
3.1 Free-standing Sn@CFC anode.....	33
3.1.1 Introduction.....	33
3.1.2 Material characterizations of Sn@CFC .....	34
3.1.3 Electrochemical characterizations of Sn@CFC.....	38
3.1.4 Conclusions of the Sn@CFC project.....	48
3.2 The SnP <sub>2</sub> O <sub>7</sub> @C anode with high pseudocapacitance .....	49
3.2.1 Introduction.....	49
3.2.2 Material characterizations of SnP <sub>2</sub> O <sub>7</sub> @C .....	51

3.2.3 Electrochemical properties of SnP <sub>2</sub> O <sub>7</sub> @C.....	56
3.2.4 Conclusions of the SnP <sub>2</sub> O <sub>7</sub> @C project .....	67
3.3 Heterostructure SnS/Sb <sub>2</sub> S <sub>3</sub> @SNC anode with engineered porous structure .....	68
3.3.1 Introduction.....	68
3.3.2 Material characterizations of SnS/Sb <sub>2</sub> S <sub>3</sub> @SNC .....	69
3.3.3 Electrochemical performance of SnS/Sb <sub>2</sub> S <sub>3</sub> @SNC.....	74
3.3.4 Conclusions of the SnS/Sb <sub>2</sub> S <sub>3</sub> @SNC project .....	81
3.4 Conclusions.....	81
Chapter 4 Tetrahydrofuran electrolyte additive for highly reversible aqueous zinc-ion batteries .....	82
4.1 Introduction.....	82
4.2 Results and analysis .....	83
4.2.1 DFT simulation and electrolyte characterization.....	83
4.2.2 Electrochemical performance of the Zn  Cu asymmetrical Cell and Zn symmetrical cell .....	88
4.2.3 Cycled Zn electrode characterizations .....	100
4.2.4 Full cell evaluation.....	106
4.3 Conclusions.....	108
Chapter 5 Conclusion and Future Work .....	110
5.1 Conclusions.....	110

5.2 Significance.....	113
5.3 Future work.....	113
Reference .....	115
CURRICULUM VITAE.....	142



## LIST OF FIGURES

<b>Figure 1. 1</b> CO <sub>2</sub> emissions from the fuel use [1].	1
<b>Figure 1. 2</b> The types of the renewable energy resources [9].	2
<b>Figure 1. 3</b> Cost-effective storage can provide many benefits to the electric grid (From DOE website).	3
<b>Figure 1. 4</b> Comparison with lithium and sodium [14].	4
<b>Figure 1. 5</b> Classification of Na–Me–O layered materials with sheets of edge-sharing MeO <sub>6</sub> octahedra and phase transition processes induced by sodium extraction [21].	6
<b>Figure 1. 6</b> (a) Unit cell of the original PB, (b) PBA of Na <sub>x</sub> MnFe(CN) <sub>6</sub> structure [29].	7
<b>Figure 1. 7</b> The schematic roadmap of SIBs over years, highlighting the discovery of key materials and the relevant prototypes [30].	8
<b>Figure 1. 8</b> Working principles of SIBs, in which the cathode materials and anode materials are represented by layered NaMnO <sub>2</sub> and hard carbon, respectively [33].	9
<b>Figure 1. 9</b> Schematic illustration of the differences in ion storage between graphite and HC [44].	10
<b>Figure 1. 10</b> Schematic illustration of the structural evolution of Sn nanoparticles during the sodiation [47].	11
<b>Figure 1. 11</b> Schematic drawing of the elementary setup for electrospinning [49].	12
<b>Figure 1. 12</b> Schematic illustration of the synthesis process for the SnS/C nanofibers [51].	13
<b>Figure 1. 13</b> XRD pattern of the ultralong Sb <sub>2</sub> Se <sub>3</sub> nanowires (a); digital photographs of the Sb <sub>2</sub> Se <sub>3</sub> ultralong nanowire-based membrane (front view (b) and side view (c)); front view SEM images (d, e) and cross-section view SEM image (f) of the achieved	

membrane; TEM images (g, h) and HRTEM image (i) of Sb <sub>2</sub> Se <sub>3</sub> ultralong nanowires [52]. .....	14
<b>Figure 1. 14</b> (a) Schematic illustration of the formation of an SMS/C composite, (b, c) SEM, (d) TEM, (e, f) HRTEM, (g) EDX elemental mapping images, and XPS spectra of (h) Sn 3d, (i) Mn 2p, and (j) C 1s for the SMS/C composite [54]. .....	15
<b>Figure 1. 15</b> Theoretical study of the role of the Co vacancies at the atomically thin interface in promoting the Na <sup>+</sup> storage performance. (a, b) Top views of the optimized CoSe <sub>2</sub> /GE and Co <sub>1-x</sub> Se <sub>2</sub> /GE structures with green Se, blue Co, and brown C. (c, d) Side views of the most stable Na (yellow) adsorption positions at the interfaces of CoSe <sub>2</sub> /GE and Co <sub>1-x</sub> Se <sub>2</sub> /GE. (e) Na adsorption energies. (f-i) Top and side views of Na diffusion pathways at the interfaces of CoSe <sub>2</sub> /GE and Co <sub>1-x</sub> Se <sub>2</sub> /GE. (j) Na diffusion energy barriers [56]. .....	16
<b>Figure 1. 16</b> A brief development history of rechargeable ZIBs [71]. .....	18
<b>Figure 1. 17</b> (a) Multi-angle comparison of ZIBs and LIBs. (b) Schematic illustration of the working principle of the rechargeable ZIBs [71]. .....	18
<b>Figure 1. 18</b> (a) Schematic representation of the deposition/stripping processes of the Zn anode in AZIBs. (b) Schematic illustration of the Zn dendrite and interface side reactions of the Zn anode [82]. .....	21
<b>Figure 1. 19</b> (a) Schematic illustration of fabricating ultrathin graphene layers on the Zn foil. (b) Optical images of bare Zn foil and NGO@Zn. (c) SEM images of NGO@Zn sample, and the inset image represents the side-views of NGO@Zn. (d) N 1s XPS spectrum of NGO@Zn. The dashed gray and red lines represent the raw and fitted data,	

respectively. (e) O 1s XPS spectrum of NGO@Zn. The dashed gray and red lines represent the raw and fitted data [78].	23
<b>Figure 2. 1</b> Schematic illustration of the synthesis of the free-standing Sn@CFC electrode.	27
<b>Figure 2. 2</b> Schematic illustration of the synthesis of the SnP <sub>2</sub> O <sub>7</sub> @C anode.	28
<b>Figure 2. 3</b> Schematic illustration of the synthesis processes of SnS/Sb <sub>2</sub> S <sub>3</sub> @SNC.	29
<b>Figure 3. 1</b> Morphology characterization of Sn@CFC. (a-c) SEM images, (d, e) TEM images, (f) high-resolution TEM image.	35
<b>Figure 3. 2</b> STEM image with the corresponding EDS elemental mappings of Sn@CFC.	35
<b>Figure 3. 3</b> (a) XRD pattern, (b) Raman spectra and (c) TGA curve of Sn@CFC.	36
<b>Figure 3. 4</b> XPS spectra of Sn@CFC.	37
<b>Figure 3. 5</b> CV curves of Sn@CFC at a scan rate of 0.1 mV s <sup>-1</sup> .	39
<b>Figure 3. 6</b> (a) Galvanostatic discharge/charge profiles at the first cycle. (c) Ex situ XRD patterns of Sn@CFC at different charge-discharge states.	40
<b>Figure 3. 7</b> (a) Cycling performance at 50 mA g <sup>-1</sup> . (b) Galvanostatic discharge/charge profiles at 50 mA g <sup>-1</sup> .	41
<b>Figure 3. 8</b> Rate performance of Sn@CFC at various rates (50–1000 mA g <sup>-1</sup> ).	42
<b>Figure 3. 9</b> Long-term cycling performance at 200 mA g <sup>-1</sup> with high mass loading of 5.5 mg cm <sup>-2</sup> .	43

<b>Figure 3. 10</b> Schematic illustration of the structure revolution of the free-standing Sn@CFC electrode. ....	44
<b>Figure 3. 11</b> Photographs of the free-standing Sn@CFC electrode after 200 cycles. ....	45
<b>Figure 3. 12</b> XRD of Sn@CFC after 200 cycles (charge to 1.0 V). ....	45
<b>Figure 3. 13</b> SEM images of the Sn@CFC electrode after 200 cycles. ....	46
<b>Figure 3. 14</b> The electrochemical kinetic properties of the Sn@CFC anode. (a) CV curves at various scan rate from $0.1 \text{ mV s}^{-1}$ to $1 \text{ mV s}^{-1}$ . (b) The corresponding curves $\log i$ versus $\log v$ for the cathodic and anodic peak. (c) CV curve and the capacitive contribution (shaded area) at $0.5 \text{ mV s}^{-1}$ . (d) The capacitive contribution in percentage at different scan rates. ....	48
<b>Figure 3. 15</b> The FESEM image (a) and TEM image (b) of $\text{SnP}_2\text{O}_7$ . ....	51
<b>Figure 3. 16</b> The morphologies and microstructures of $\text{SnP}_2\text{O}_7@\text{C}$ , (a–d) FESEM images, and (e–h) TEM images. ....	52
<b>Figure 3. 17</b> STEM image with the EDS elemental mappings. ....	52
<b>Figure 3. 18</b> The XRD pattern of (a) $\text{Sn}(\text{HPO}_4)_2 \cdot \text{H}_2\text{O}$ and (b) $\text{SnP}_2\text{O}_7@\text{C}$ . ....	53
<b>Figure 3. 19</b> (a) The RTIR spectra of $\text{SnP}_2\text{O}_7$ and $\text{SnP}_2\text{O}_7@\text{C}$ , and (b) Raman spectra of $\text{SnP}_2\text{O}_7@\text{C}$ . ....	54
<b>Figure 3. 20</b> TGA profile of $\text{SnP}_2\text{O}_7@\text{C}$ in air. ....	55
<b>Figure 3. 21</b> (a–f) XPS spectra of $\text{SnP}_2\text{O}_7@\text{C}$ . ....	56
<b>Figure 3. 22</b> CV curves of the (a) $\text{SnP}_2\text{O}_7$ and (b) $\text{SnP}_2\text{O}_7@\text{C}$ electrodes at a scan rate of $0.1 \text{ mV s}^{-1}$ . ....	57
<b>Figure 3. 23</b> HRTEM image of $\text{SnP}_2\text{O}_7@\text{C}$ after full charged to 2 V. ....	58

<b>Figure 3. 24</b> Discharge/charge profiles of the SnP <sub>2</sub> O <sub>7</sub> and SnP <sub>2</sub> O <sub>7</sub> @C electrodes at 200 mA g <sup>-1</sup> .....	58
<b>Figure 3. 25</b> (a) Discharge/charge curves of SnP <sub>2</sub> O <sub>7</sub> @C. (b) <i>Ex-situ</i> XRD patterns of SnP <sub>2</sub> O <sub>7</sub> @C at selected discharge-charge states.....	59
<b>Figure 3. 26</b> (a) Cycling performance, and (b) Rate performance of the SnP <sub>2</sub> O <sub>7</sub> @C and SnP <sub>2</sub> O <sub>7</sub> electrodes. ....	60
<b>Figure 3. 27</b> (a) Long-term cycling performance of SnP <sub>2</sub> O <sub>7</sub> @C at 1000 mA g <sup>-1</sup> , and (b) corresponding discharge/charge profiles. ....	61
<b>Figure 3. 28</b> EIS spectra of the SnP <sub>2</sub> O <sub>7</sub> @C electrodes. ....	63
<b>Figure 3. 29</b> Schematic illustration for the cycling process of the SnP <sub>2</sub> O <sub>7</sub> @C and SnP <sub>2</sub> O <sub>7</sub> electrodes. ....	64
<b>Figure 3. 30</b> (a-b) TEM images of SnP <sub>2</sub> O <sub>7</sub> @C after 100 cycles at 200 mA g <sup>-1</sup> . (c) The SnP <sub>2</sub> O <sub>7</sub> particle size distribution diagram of before cycle (upper) and after 100 cycles (lower).....	64
<b>Figure 3. 31</b> EIS spectra of the SnP <sub>2</sub> O <sub>7</sub> @C electrode before and after 100 cycles. ....	65
<b>Figure 3. 32</b> (a) CV curves of the SnP <sub>2</sub> O <sub>7</sub> @C electrode at various scan rate. (b) Calculation of the b values based on the curves of log i vs. log v.....	66
<b>Figure 3. 33</b> (a) CV curves of the SnP <sub>2</sub> O <sub>7</sub> electrode at various scan rate. (b) The corresponding curves of log i versus log v for cathodic and anodic peaks of the SnP <sub>2</sub> O <sub>7</sub> electrode.....	66
<b>Figure 3. 34</b> (a) Capacitive-controlled behavior at 0.4 mV s <sup>-1</sup> . (b) The capacitive contribution at different scan rates.....	67
<b>Figure 3. 35</b> The SEM images of SnS/Sb <sub>2</sub> S <sub>3</sub> @C.....	70

<b>Figure 3. 36</b> SEM images of the SnS/Sb <sub>2</sub> S <sub>3</sub> heterostructure.....	70
<b>Figure 3. 37</b> Selected SnS/Sb <sub>2</sub> S <sub>3</sub> @C particle for the EDS mapping, and the corresponding EDS elemental mappings.....	71
<b>Figure 3. 38</b> BET analysis of SnS/Sb <sub>2</sub> S <sub>3</sub> @SNC. (a) The nitrogen adsorption-desorption isotherm, and (b) the pore-size distribution curves.....	71
<b>Figure 3. 39</b> (a) XRD pattern, (b) Raman spectra, and (c) TGA curve of SnS/Sb <sub>2</sub> S <sub>3</sub> @C. ....	72
<b>Figure 3. 40</b> XPS spectra of SnS/Sb <sub>2</sub> S <sub>3</sub> @C, (a) survey, (b) Sn 3d, (c) Sb 3d, (d) S 2p, (e) C 1s, (f) N 1s.....	74
<b>Figure 3. 41</b> CV curves of SnS/Sb <sub>2</sub> S <sub>3</sub> @SNC at a scan rate of 0.1 mV s <sup>-1</sup> . ....	75
<b>Figure 3. 42</b> (a) Galvanostatic discharge/charge profiles, and (b) Cycling performance of the SnS/Sb <sub>2</sub> S <sub>3</sub> @SNC electrode at 200 mA g <sup>-1</sup> .....	76
<b>Figure 3. 43</b> The charge/discharge curves of the SnSb <sub>x</sub> and SnS/Sb <sub>2</sub> S <sub>3</sub> electrodes. ....	76
<b>Figure 3. 44</b> Schematic illustration of the micro-electric field at the SnS/Sb <sub>2</sub> S <sub>3</sub> heterointerfaces. ....	77
<b>Figure 3. 45</b> The Nyquist plots of the (a) SnS/Sb <sub>2</sub> S <sub>3</sub> and SnS/Sb <sub>2</sub> S <sub>3</sub> @SNC electrodes before cycle, and (b) the SnS/Sb <sub>2</sub> S <sub>3</sub> @SNC electrode before and after 10 cycles. ....	78
<b>Figure 3. 46</b> (a) Rate performance of SnS/Sb <sub>2</sub> S <sub>3</sub> @SNC and SnS/Sb <sub>2</sub> S <sub>3</sub> at various rates (50–5000 mA g <sup>-1</sup> ), and (b) Long-term cycling performance of the SnS/Sb <sub>2</sub> S <sub>3</sub> @SNC anode at 500 mA g <sup>-1</sup> . ....	79
<b>Figure 3. 47</b> The electrochemical kinetic properties of SnS/Sb <sub>2</sub> S <sub>3</sub> @SNC. (a) CV curves at various scan rates from 0.1 to 1 mV s <sup>-1</sup> . (b) The corresponding curves log i versus log v for the cathodic and anodic peaks. (c) CV curve and the capacitive contribution (shaded	

area) at $0.8 \text{ mV s}^{-1}$ . (d) The capacitive contribution in percentage at different scan rates. .....	80
<b>Figure 4. 1</b> The molecular formula of (a) $\text{H}_2\text{O}$ and (b) THF molecules. ....	83
<b>Figure 4. 2</b> Optimized solvation structure and the corresponding solvation energy with the THF additive in the DFT calculations.....	83
<b>Figure 4. 3</b> The optimized structures of (a) 6 $\text{H}_2\text{O}$ molecule clusters with 7 hydrogen bonds (as represented by the grey dashed lines); and (b) 5 $\text{H}_2\text{O}$ and 1 THF molecule cluster with 10 hydrogen bonds. ....	86
<b>Figure 4. 4</b> (a) Raman spectra, and (b) FTIR spectra of the baseline 2 M $\text{ZnSO}_4$ and 2 M $\text{ZnSO}_4/\text{THF}$ 5% electrolytes.....	86
<b>Figure 4. 5</b> Digital images of the electrolytes in vials at the initial state and after 30 days. (a, b) Baseline 2 M $\text{ZnSO}_4$ , and (c, d) 2 M $\text{ZnSO}_4/\text{THF}$ 5%. ....	87
<b>Figure 4. 6</b> Contact angle measurement of (a) 2 M $\text{ZnSO}_4$ and (b) 2 M $\text{ZnSO}_4/\text{THF}$ 5% on the Zn electrode.....	88
<b>Figure 4. 7</b> (a-c) The electrochemical stability window of the aqueous electrolytes measured using the polarization scanning at $1 \text{ mV s}^{-1}$ on the non-active Ti electrodes between -0.5 V and 3.0 V versus $\text{Zn}^{2+}$ .....	89
<b>Figure 4. 8</b> (a) Current-time plots of the Zn symmetric cell with the 2 M $\text{ZnSO}_4$ electrolyte after the application of a constant potential (25 mV) and the corresponding impedance spectra before and after polarization; (b) Current-time plots of the Zn symmetric cell with the $\text{ZnSO}_4/\text{THF}$ 5% electrolyte after the application of a constant	

potential (25 mV) and the corresponding impedance spectra before and after polarization.  
 ..... 90

**Figure 4. 9** Comparison of the Tafel plots representing corrosion behavior of the Zn electrodes under different electrolyte systems..... 91

**Figure 4. 10** (a) Zn plating/stripping CE of the Zn||Cu cells with the different electrolytes. (b) Voltage profiles in the 2 M ZnSO<sub>4</sub> and 2 M ZnSO<sub>4</sub>/THF 5% electrolytes at the initial two cycles. (c, d) Voltage profiles of the Zn plating/stripping processes at selected cycles in the ZnSO<sub>4</sub>/THF 5% electrolyte..... 92

**Figure 4. 11** (a) CE of the Zn||Cu cells with the ZnSO<sub>4</sub>/THF 10% electrolyte. (b) profiles of the Zn plating/stripping processes at selected cycles. .... 93

**Figure 4. 12** (a) Galvanostatic Zn plating/stripping in the Zn symmetrical cell at 0.5 mA cm<sup>-2</sup> and 0.5 mA h cm<sup>-2</sup>. (b) Voltage profiles of the Zn symmetric cells at 0.5 mA cm<sup>-2</sup> and 0.5 mA h cm<sup>-2</sup>. (c) The corresponding overpotential of Zn symmetric cells at 0.5 mA cm<sup>-2</sup>. .... 94

**Figure 4. 13** (a-d) Galvanostatic Zn plating/stripping in the Zn symmetrical cell at 0.5 mA cm<sup>-2</sup> and 0.5 mA h cm<sup>-2</sup>..... 95

**Figure 4. 14** (a) The equivalent circuit of the EIS tests based on the Zn symmetrical cell, and (b, c) Nyquist plots of the baseline 2 M ZnSO<sub>4</sub> electrolyte and the 2 M ZnSO<sub>4</sub>/THF 5% electrolytes..... 96

**Figure 4. 15** Galvanostatic Zn plating/stripping in the Zn symmetrical cell at (d) 1 mA cm<sup>-2</sup> and 1 mA h cm<sup>-2</sup> and (e) at 5 mA cm<sup>-2</sup> and 1 mA h cm<sup>-2</sup>. .... 97

**Figure 4. 16** Overcharging test of the Zn symmetric cells at 1 mA cm<sup>-2</sup>..... 98



<b>Figure 4. 17</b> Illustration of surface evolution mechanism with and without the THF additive.....	100
<b>Figure 4. 18</b> XRD patterns of the Zn foil after 100 cycles at $0.5 \text{ mA cm}^{-2}$ and $0.5 \text{ mA h cm}^{-2}$ .....	101
<b>Figure 4. 19</b> Volume expansion comparison of (a-c) $2 \text{ M ZnSO}_4$ , (d-f) $2 \text{ M ZnSO}_4/ \text{THF } 5\%$ symmetric cells after 100 cycles.....	101
<b>Figure 4. 20</b> Photograph of the home-built devices for in situ monitoring of the $\text{H}_2$ evolution. ....	102
<b>Figure 4. 21</b> (a, b) <i>In-situ</i> optical microscopy of the $\text{H}_2$ generation in $2 \text{ M ZnSO}_4$ and $2 \text{ M ZnSO}_4/\text{THF } 5\%$ in the symmetrical cells at a current density of $10 \text{ mA cm}^{-2}$ .....	103
<b>Figure 4. 22</b> The optical images of the Zn electrodes in (a) $2 \text{ M ZnSO}_4$ and (b) $2 \text{ M ZnSO}_4/\text{THF } 5\%$ after 100 cycles. ....	104
<b>Figure 4. 23</b> (a-c) The SEM images of the Zn electrode before plating. ....	104
<b>Figure 4. 24</b> SEM images of (c, d) Zn electrode after 100th plating in $2 \text{ M ZnSO}_4$ , and (e) corresponding EDS mapping. SEM images of (f, g) Zn electrode after 100th plating in $2 \text{ M ZnSO}_4/\text{THF } 5\%$ , and (h) corresponding EDS mapping. ....	105
<b>Figure 4. 25</b> Electrochemical performance of the $\text{Zn}  \text{MnO}_2$ cells in the different electrolytes. (a) CV at a scan rate of $0.1 \text{ mV s}^{-1}$ . (b) Charge-discharge profiles. (c) EIS spectra. (d) Rate performance. (e) Cyclic stability at $500 \text{ mA g}^{-1}$ . ....	107
<b>Figure 4. 26</b> Charge-discharge profiles at selected cycles of the $\text{Zn}  \text{MnO}_2$ cells in the $2 \text{ M ZnSO}_4/\text{THF } 5\%$ electrolyte. ....	108

## LIST OF TABLES

<b>Table 3. 1</b> Performance of the common mix-reaction type anode materials for SIBs. ....	62
<b>Table 4. 1</b> The total energy of the two solvation structures ( $E_{total}$ ), the energy of the H <sub>2</sub> O/H <sub>2</sub> O+THF molecule clusters ( $E_{H_2O/THF+H_2O}$ ), and the energy of the isolated Zn <sup>2+</sup> ion ( $E_{Zn^{2+}}$ ). The corresponding solvation energies ( $E_{sol}$ ) for the two-solvation structure are calculated based on Eq. 2-1. ....	85
<b>Table 4. 2</b> The comparison of the plating/stripping hours in AZIBs with other previous works.....	98

## ABSTRACT

ELECTRODE AND ELECTROLYTE DESIGN TO DEVELOP ADVANCED  
BATTERY TECHNOLOGIES FOR LARGE SCALE ENERGY STORAGE

WEI HE

2023

Large-scale energy storage devices play a key role in regulating the renewable energy to build a carbon-free sustainable future, but the widely used lithium-ion batteries cannot meet the demands because of the limited lithium resource and high cost. Thus, it is urgent to develop next-generation battery technologies with low cost and high safety.

Sodium-ion battery is considered as a promising candidate due to the abundant sodium resources and low cost. Its practical application, however, is hindered by the absence of the advanced electrode materials. The tin-based anodes deliver high theoretical capacities and show great promise for the sodium-ion batteries, but the large volume expansion upon cycling can damage the structure and lead to short cycling life. In this dissertation, three tin-base anodes have been developed. First, a free-standing Sn@CFC electrode was synthesized *via* the electrospinning method. The carbon fiber and Sn nanoparticles together provide fast ions and electrons pathway, enabling a dominant pseudocapacitance contribution. Moreover, the facile manufacturing technique yields the Sn@CFC electrode with a high mass loading. Second, a novel anode was designed with a pomegranate-like structure that the SnP<sub>2</sub>O<sub>7</sub> nanoparticles dispersed in the robust N-doped carbon matrix. The carbon matrix forms strong interaction with the SnP<sub>2</sub>O<sub>7</sub> nanoparticles, leading to a stable structure without any particle aggregation. Third, a SnS/Sb<sub>2</sub>S<sub>3</sub> heterostructure was

prepared and encapsulated in the sulfur and nitrogen co-doped carbon matrix with engineered porous structure. The porous structure can provide void space to alleviate the volume expansion upon cycling, guaranteeing excellent structural stability. The unique heterostructure and the S, N co-doped carbon matrix together facilitate fast-charge transport to improve reaction kinetics.

Aqueous zinc-ion batteries show great promise in large-scale energy storage. However, the decomposition of water molecules leads to severe side reactions, resulting in the limited lifespan of the zinc-ion batteries. Here, the tetrahydrofuran additive was introduced into the zinc sulfate electrolyte to reduce the water activity by modulating the solvation structure of the Zn hydration layer. Thus, in an optimal 2 M ZnSO<sub>4</sub>/THF (5% by volume) electrolyte, the hydrogen evolution reaction and byproduct precipitation can be suppressed, which greatly improves the cycling stability and Coulombic efficiency.

# Chapter 1 Introduction: sodium-ion batteries and aqueous zinc-ion batteries

## 1.1 Background

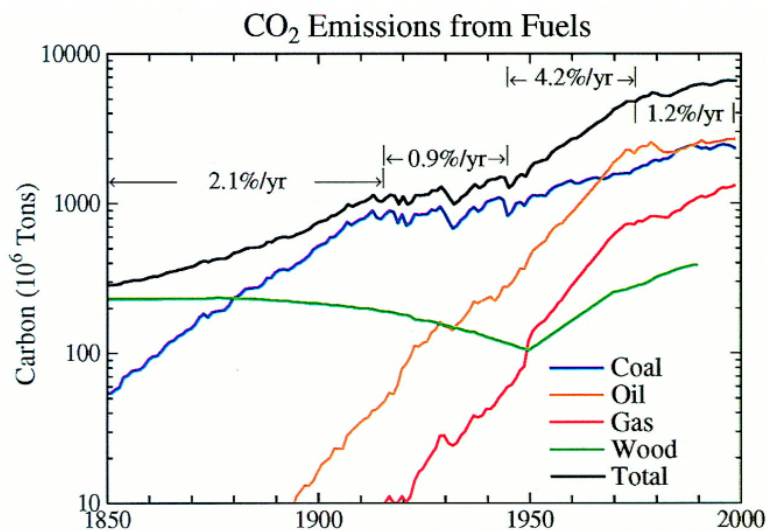


**Figure 1. 1** CO<sub>2</sub> emissions from the fuel use [1].

The use of the traditional fossil fuels such as coal and oil can generate billions of tons of carbon dioxide (CO<sub>2</sub>) annually (**Figure 1.1**) [1]. CO<sub>2</sub> is the leading greenhouse gas and is widely recognized as a key contributor to climate change [2, 3]. The effects of climate change on human beings are profound and far-reaching. Extreme weather events and rising sea level are just a few of the ways that climate change impacts our lives [4, 5]. These changes can have significant consequences for public health[6], food security[7], and economic stability[8]. For example, damage from extreme weather events such as hurricanes and floods can result in billions of dollars in economic losses, while rising sea

levels threaten to inundate low-lying coastal areas, displacing millions of people and disrupting economic activity.

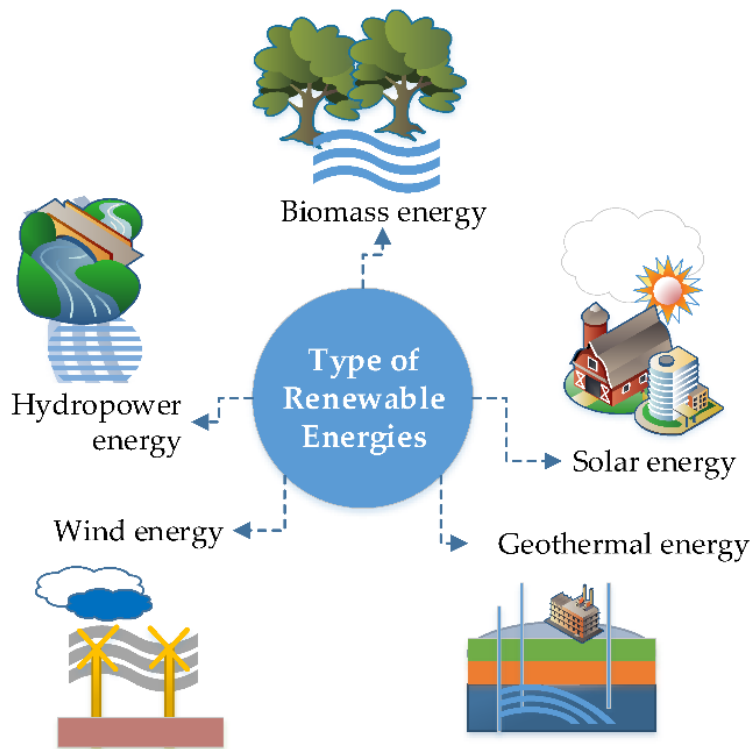


**Figure 1. 2** The types of the renewable energy resources [9].

Climate change is one of the most pressing issues facing humanity today, and reducing the amount of CO<sub>2</sub> is critical in addressing this problem. To do this, we need to shift away from fossil fuels and develop renewable sources of energy, such as wind, hydropower, biomass, and solar power. These sources of energy do not produce greenhouse gases and can also help reduce air pollution. Additionally, investing in renewable energy can diversify our energy supply, reduce our dependence on imported fuels, and create jobs in manufacturing, installation, and maintenance. However, there are some challenges associated with using renewable energy. One of the biggest challenges is the cost, which can be higher than traditional fossil fuel sources. Additionally, advanced

technology may not be available in all areas, and certain geographical barriers may make it difficult to harvest energy from renewable sources in certain locations. For example, wind energy may vary throughout different seasons, and the sun may not be always available due to cloudy weather or nighttime. To address these challenges, it is crucial to develop large-scale energy storage (LSES) devices that can store the energy from harvested renewable sources. This can ensure that there is a regular and consistent supply of energy, regardless of fluctuations in weather conditions or energy demand. By investing in energy storage technology, we can maximize the potential of renewable energy and ensure that it is a reliable and sustainable source of power for years to come. **Figure 1.3** shows the use of the LSES solution to regulate the renewable energy of wind and solar.

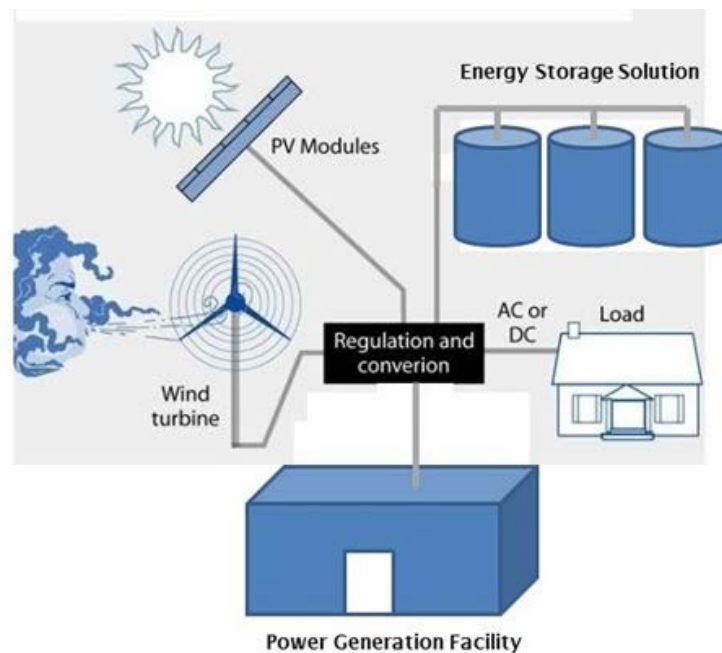


**Figure 1.3** Cost-effective storage can provide many benefits to the electric grid (From DOE website).

Lithium-ion batteries (LIBs) have revolutionized the way we live since their first commercialization. LIBs are lightweight with high energy densities, which makes them ideal for the use in the electronics and electric vehicles. However, the limited lithium resources result in the high cost of LIBs, and the safety risks generating from the use of organic electrolytes have limited their further application in the LSES devices. To meet the ever-growing demand for LSES, researchers are working on developing next-generation batteries that can overcome these limitations. These new batteries could have high energy density, long cycle life, and low cost, making them more practical for the use in LSES. The most promising candidates are the sodium-ion batteries (SIBs) [10, 11] and aqueous zinc-ion batteries (AZIBs) [12, 13] because of their potential to provide a cheaper and more abundant alternative to the popular LIBs. These advancements will pave the way for a more sustainable and reliable energy future. **Figure 1.4** shows the comparison with lithium and sodium that the sodium is much cheaper than the lithium.

	lithium	sodium
ratio of reserves	1	1,000
cost (for carbonate)	\$ 5,000/t	\$ 150/t
atomic weight	6.9 g/mol	23 g/mol
ionic volume	1.84 Å <sup>3</sup>	4.44 Å <sup>3</sup>
theoretical capacity	3,829 mAh/g	1,165 mAh/g
normal electrode potential vs. SHE	-3.045 V	-2.714 V

**Figure 1. 4** Comparison with lithium and sodium [14].



## 1.2 Sodium-ion batteries

### 1.2.1 A brief history of SIBs

The idea of using sodium as a battery material can date back to early 20th century in the high-temperature sodium-based battery technologies such as sodium-chlorine (Na/NaCl [15]) battery and sodium-sulfur (Na/S [16]) battery. However, the high operating temperatures of the Na/NaCl and Na/S batteries and the safety concerns limited their further applications in LSES. In 1980, Newman and L. Klemann from Exxon Research and Engineering Company tried to employ the  $\text{Na}^+$  as the intercalating ion using titanium sulfides ( $\text{TiS}_2$ ) as the host structure at room temperature [17]. In the same year, Delmas et al. presented the structural classification and characteristics of the  $\text{A}_x\text{MO}_2$  layered oxide, where A represents alkali metals and M denotes transition metals [18]. They categorized these oxides into three types, namely O3, P2, and P3, based on the Na crystallographic site and the stacking sequence of  $\text{MO}_2$  slabs in  $\text{Na}_x\text{MO}_2$  (As shown in **Figure 1.5**). This classification system continues to be widely used in the present day [19]. The same team subsequently reported  $\text{Na}_x\text{CoO}_2$  ( $0.5 \leq x \leq 1$ ) layered oxide for the first time, which showed great promise for SIBs [20].

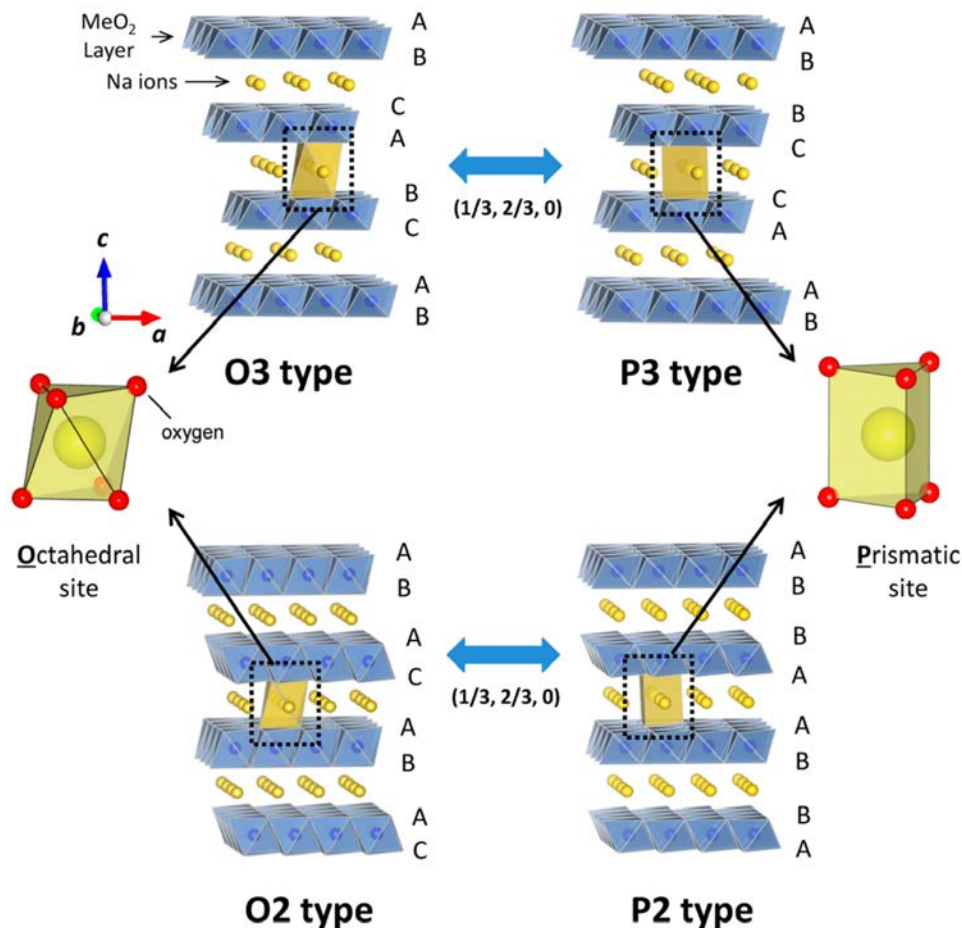


**Figure 1. 5** Classification of Na–Me–O layered materials with sheets of edge-sharing MeO<sub>6</sub> octahedra and phase transition processes induced by sodium extraction [21].

In the anode side, the early research has demonstrated that the graphite anode, which is widely used in the LIBs, fails in SIBs because Na<sup>+</sup> cannot be intercalated into graphite [22, 23]. Thus, Dahn et al. introduced hard carbon (HB, non-graphitizable carbon) as an advanced anode material in 2000 [24, 25]. Since then, SIBs have attracted more and more attention in both academia and industry. Hitachi Ltd. developed the first full-cell model for SIBs with P2-Na<sub>x</sub>CoO<sub>2</sub> as cathode and sodium-lead alloy as anode in the 1980s. The first non-aqueous SIB system was introduced by Faradion Limited in 2015. After that, the

most promising cathodes of Prussian blue (PB,  $\text{Fe}[\text{Fe}(\text{CN})_6] \cdot n\text{H}_2\text{O}$ ) and Prussian blue analogues (PBAs,  $\text{Na}_{2-x}\text{M}[\text{Fe}(\text{CN})_6]_{1-y}\square_y \cdot n\text{H}_2\text{O}$ ,  $x = 0-2$ , M are transition metals,  $\square$  signify the vacancies, **Figure 1.6**) was first reported in 2015 [26, 27]. The rigid open framework and small interaction with interstitial cations make PBAs become remarkable cathodes for the SIBs [28]. Today, several companies are working to commercialize SIBs with PB as cathode and HB as anode. One of the leading companies in this field is Contemporary Amperex Technology Co., Ltd. (CATL) in China, which is developing a range of SIBs for use in electric vehicles. The schematic roadmap of SIBs over years is shown in **Figure 1.7**.

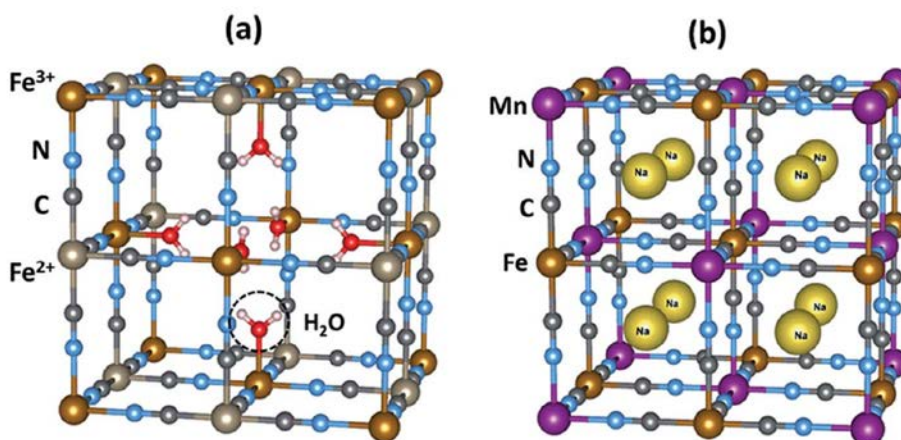


**Figure 1.6** (a) Unit cell of the original PB, (b) PBA of  $\text{Na}_x\text{MnFe}(\text{CN})_6$  structure [29].

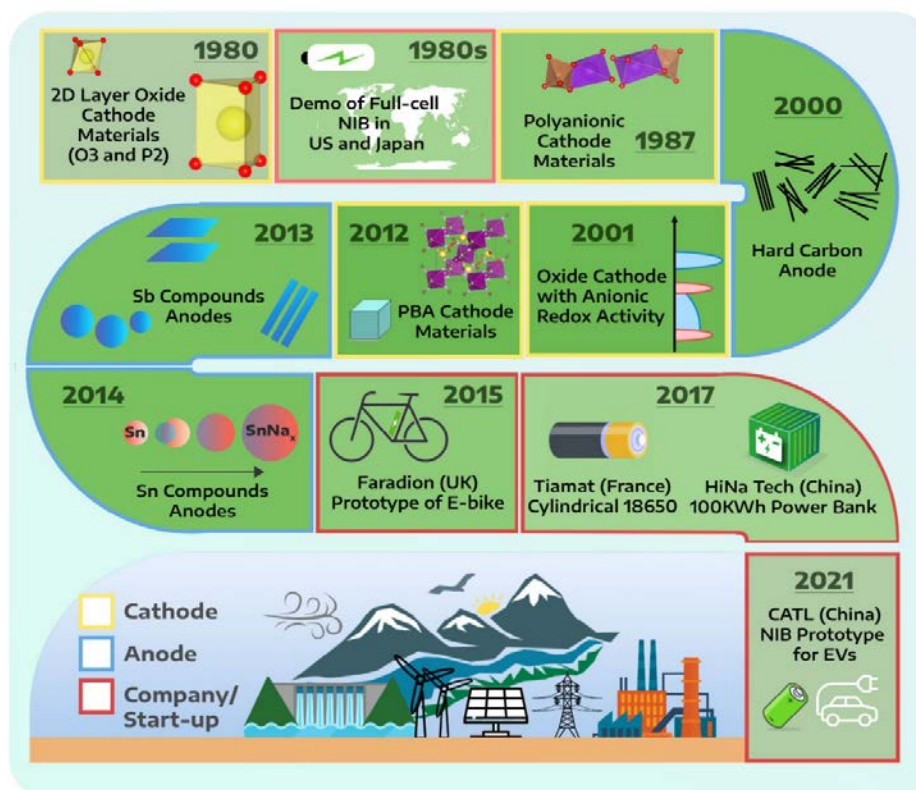


**Figure 1. 7** The schematic roadmap of SIBs over years, highlighting the discovery of key materials and the relevant prototypes [30].

### 1.2.2 Working principle of SIBs

SIBs are similar in many ways to LIBs, but they use sodium ions ( $\text{Na}^+$ ) rather than lithium ions ( $\text{Li}^+$ ) as the charge carriers [21]. This makes them an attractive alternative because sodium is more abundant and less expensive than lithium and could potentially enable more widespread adoption of energy storage systems [31]. The working principle of SIBs is based on the movement of the  $\text{Na}^+$  between the cathode and anode electrodes [32]. During charging,  $\text{Na}^+$  are extracted from the cathode material and move through the electrolyte to the anode, where they are stored. At the same time, electrons are released from the cathode and flow through an external circuit to provide power. During discharge,

the process is reversed, with the  $\text{Na}^+$  moving back through the electrolyte to the cathode, while the electrons flow through the external circuit to provide power. The cathode and anode materials used in SIBs are typically different from those used in LIBs. The chemical reactions involved in this process can be represented by the equations in **Figure 1.8** based on layered  $\text{NaMnO}_2$  as cathode and HB as anode.

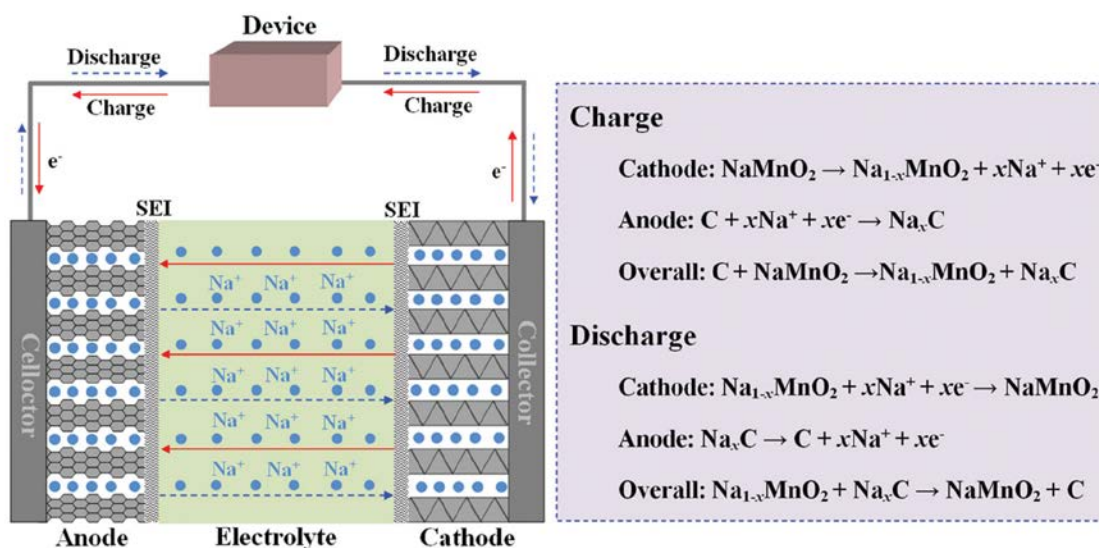


**Figure 1. 8** Working principles of SIBs, in which the cathode materials and anode materials are represented by layered  $\text{NaMnO}_2$  and hard carbon, respectively [33].

### 1.2.3 The challenges of SIBs

SIBs are the promising candidate for the LSES device due to their low cost and abundance. However, SIBs still face several challenges that must be addressed before they can be commercially viable. These challenges include low energy density, lack of suitable electrode materials, cycling stability, low power density, safety concerns, and commercialization issues [34]. The biggest challenge of SIBs is to develop advanced electrode materials with high capacity and long cycling life to meet the ever-growing

demand of the LSES devices [35, 36]. The radius of  $\text{Na}^+$  is larger than that of the  $\text{Li}^+$  (0.102 nm vs 0.076 nm), which directly affects the mass transport and storage in the electrochemical process as well as cause structural changes in the electrode materials over time, showing poor cycling stability [37-40]. Thus, the advanced anode materials for LIBs fail in the SIB system [38]. The graphite, for example, which is widely used in LIBs as an anode, forms the  $\text{NaC}_{64}$  compound in SIBs with a low capacity of  $64 \text{ mA h g}^{-1}$  [41, 42]. Therefore, another carbon material of HC has been developed as anode for SIBs, which has an enlarged interlayer lattice distance to boost  $\text{Na}^+$  ion intercalation [43]. The Schematic illustration of the differences in ion storage between graphite and HC is shown in **Figure 1.9**.

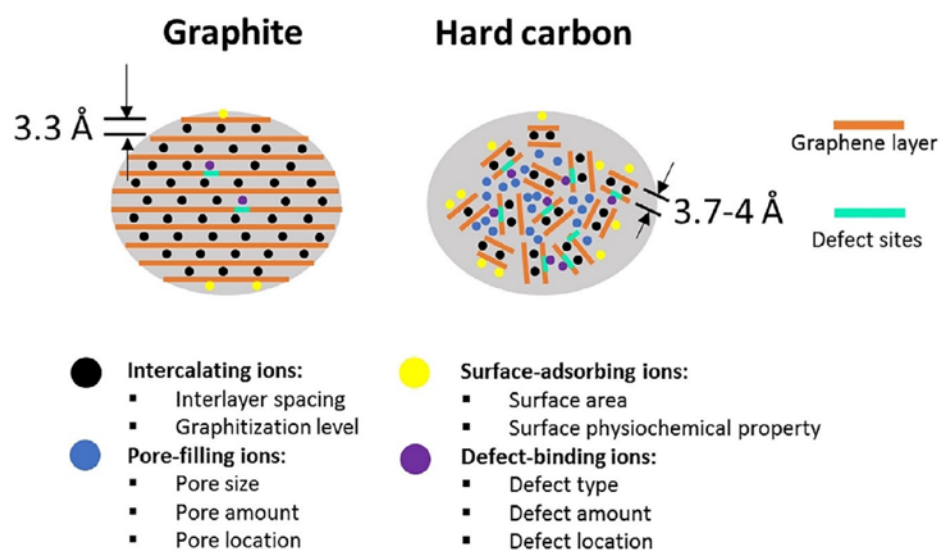


**Figure 1. 9** Schematic illustration of the differences in ion storage between graphite and HC [44].

Alloy-type anodes such as tin (Sn), bismuth (Bi) and antimony (Sb) can deliver high capacities. Sn is considered a promising anode due to its high theoretical capacity of 847

mA h g<sup>-1</sup>, as well as its low cost and environmental friendliness [45]. However, the metallic Sn electrode suffers a 420% expansion during the sodiation process, resulting in continuous pulverization of active materials and then the loss of electrical contact with the current collector (**Figure 1.10**) [46]. That will lead to a fast capacity fading and prevent its practical application in SIBs. SIBs also face challenges related to their commercialization. While SIBs have the potential to be low-cost, they still face competition from established LIBs, which have a well-established supply chain and manufacturing infrastructure. Additionally, the performance of SIBs still needs to be improved before they can compete with LIBs in terms of energy density, power density, and cycling stability.

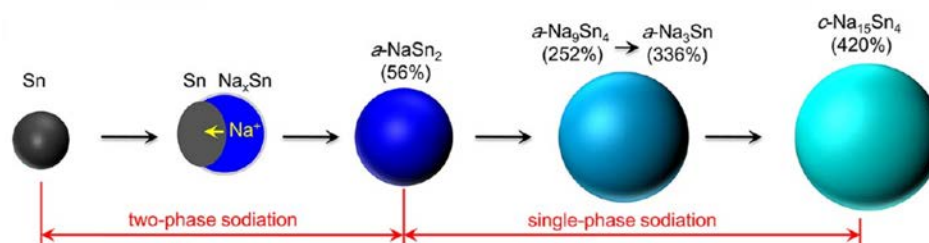


**Figure 1. 10** Schematic illustration of the structural evolution of Sn nanoparticles during the sodiation [47].

#### 1.2.4 Recent advances in the high-performance anodes

Nano-sized materials can boost the charge transfer because of the shortened diffusion pathway for Na<sup>+</sup> and electrons in SIBs [48]. For high-capacity alloying anodes, the nanoparticles can alleviate strain during the large volume changes and improve the cycling stability. The nanomaterials can be further modified by coating with protective materials especially carbon materials, which act as a buffer layer to mitigate fracture

during volume changes, enhance mechanical integrity, and improve electrical conductivity. However, the nanoparticles are easy to aggregate upon cycling, which can deteriorate the battery performance. In addition, it is very hard to improve the mass loading of the nanoparticles. Thus, it is very important to develop new technologies to prepare nano-sized anode materials with high mass loading and good electrochemical performance.

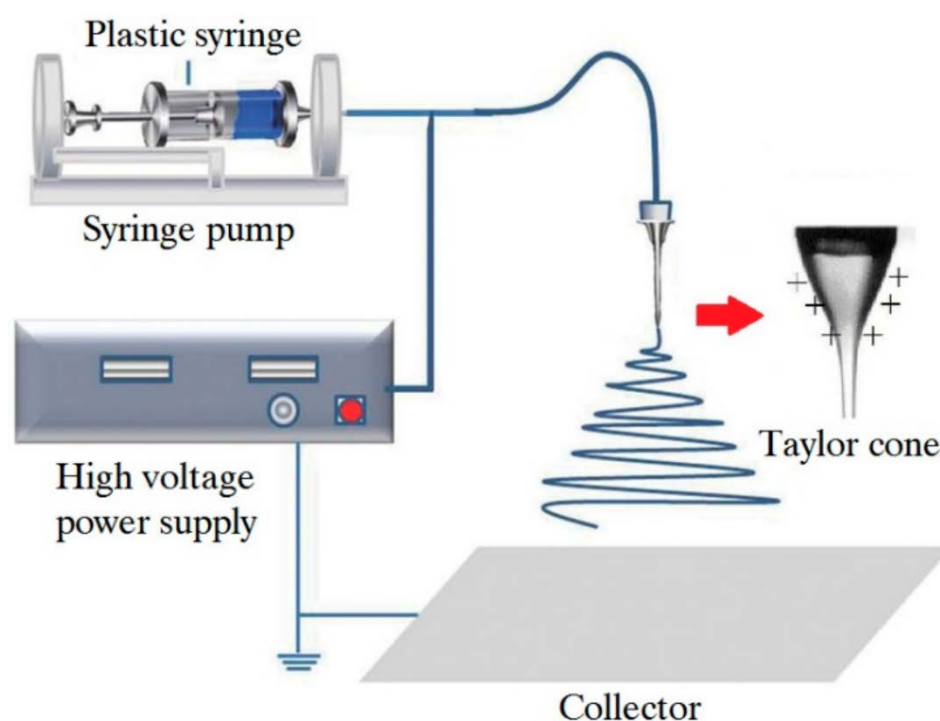


**Figure 1. 11** Schematic drawing of the elementary setup for electrospinning [49].

Electrospinning is a fiber production method that uses electric force to draw charged threads of polymer solutions or polymer melts up to fiber diameters in the order of some hundred nanometers (**Figure 1.11**) [50]. The precursors can include salts or nanoparticles in the polymer solutions. The as-prepared polymer fiber can be further carbonized to carbon fiber (CF) in which the salts will generate nanoparticles embedded in the carbon



fiber. For example, Xia et al. reported the SnS/C nanofibers film prepared by electrospinning and subsequent calcination (**Figure 1.12**). The SnS/C nanofibers are ultra-robust and has outstanding electrochemical performance when used as a free-standing electrode in LIBs and SIBs.

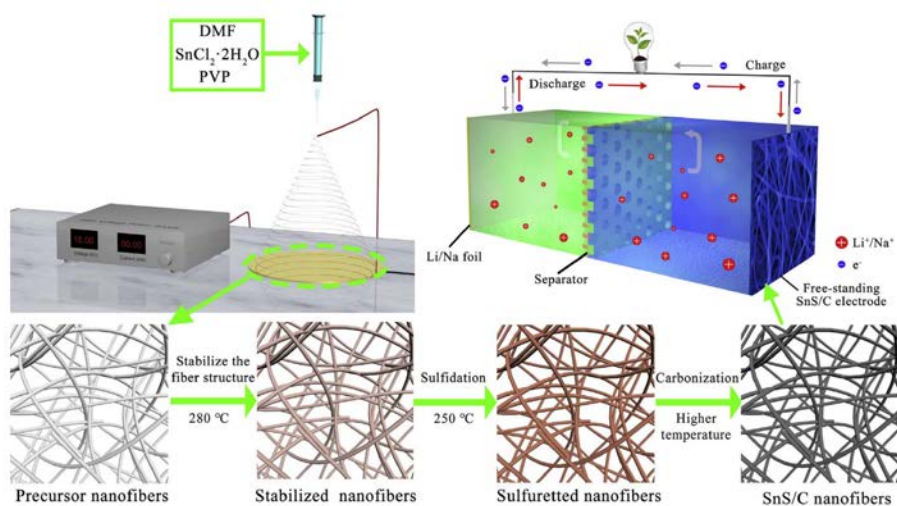


**Figure 1. 12** Schematic illustration of the synthesis process for the SnS/C nanofibers [51].

Many other methods can be used to prepare free-standing electrodes too. Mai Group fabricated a free-standing membrane based on ultralong Sb<sub>2</sub>Se<sub>3</sub> nanowires via hydrothermal synthesis and vacuum filtration treatment [52]. The freestanding membrane constructed by pure Sb<sub>2</sub>Se<sub>3</sub> nanowires has demonstrated favorable flexibility and structural soundness as shown in **Figure 1.13**. When used as an anode for SIBs, it delivers a reversible capacity of 360 mA h g<sup>-1</sup> at 100 mA g<sup>-1</sup>, retaining 289 mA h g<sup>-1</sup> after 50 cycles. Yousaf et al. used a simple wet-chemistry technique combined with thermally induced selenization to create a framework in which core-shell nanostructures of FeSe<sub>2</sub>/C are embedded in carbon nanotubes (CNTs) [53]. The 3 dimensional (3D)

continuous pathways provided by the CNT framework facilitate electronic/ionic transfer, while the macropores allow for high mass loading of FeSe<sub>2</sub>/C.

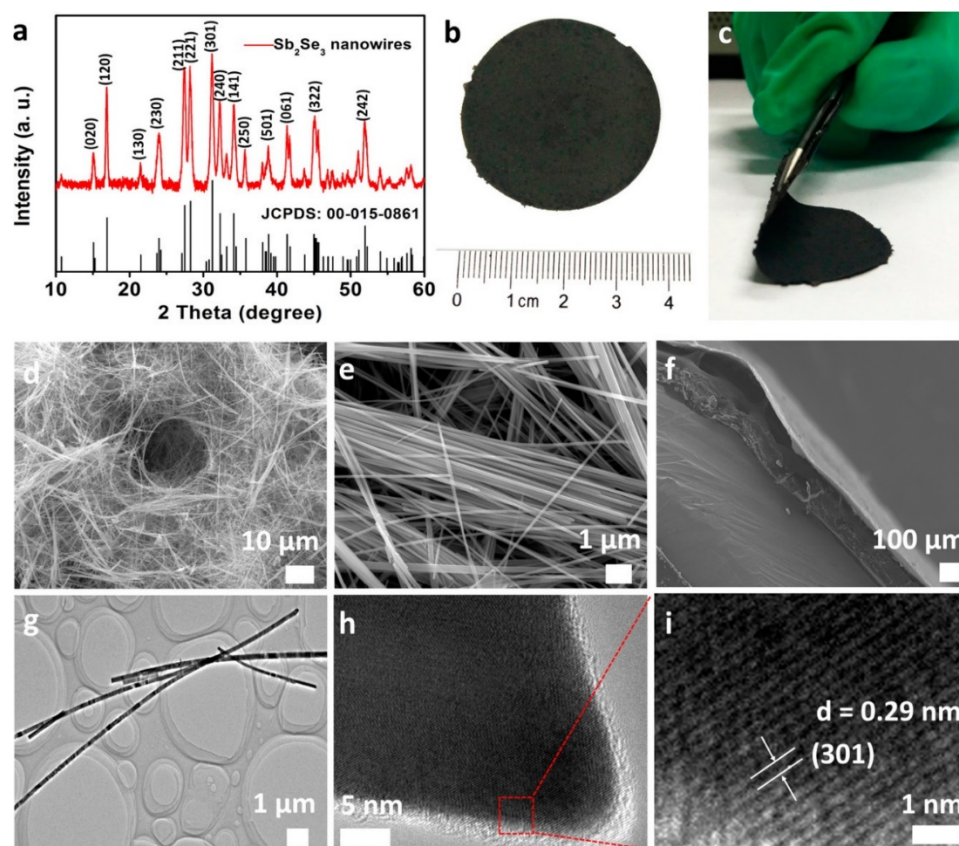


**Figure 1.13** XRD pattern of the ultralong Sb<sub>2</sub>Se<sub>3</sub> nanowires (a); digital photographs of the Sb<sub>2</sub>Se<sub>3</sub> ultralong nanowire-based membrane (front view (b) and side view (c)); front view SEM images (d, e) and cross-section view SEM image (f) of the achieved membrane; TEM images (g, h) and HRTEM image (i) of Sb<sub>2</sub>Se<sub>3</sub> ultralong nanowires [52].

Building heterostructure is another way to improve the performance of the anode materials for SIBs. The heterostructures will generate internal electric fields, which have an enhanced charge-transfer capability [54, 55]. The Liu group has developed a new anode material for SIBs using heterostructured SnS<sub>2</sub>/Mn<sub>2</sub>SnS<sub>4</sub>/carbon nanoboxes (SMS/C NBs) prepared through a facile wet-chemical method (**Figure 1.14**) [54]. The

$\text{SnS}_2/\text{Mn}_2\text{SnS}_4$  heterojunctions have a stabilizing effect on the reaction products  $\text{Sn}$  and  $\text{Na}_2\text{S}$ , preventing the coarsening of nanosized  $\text{Sn}^0$ , and promoting the reversible conversion-alloying reaction.

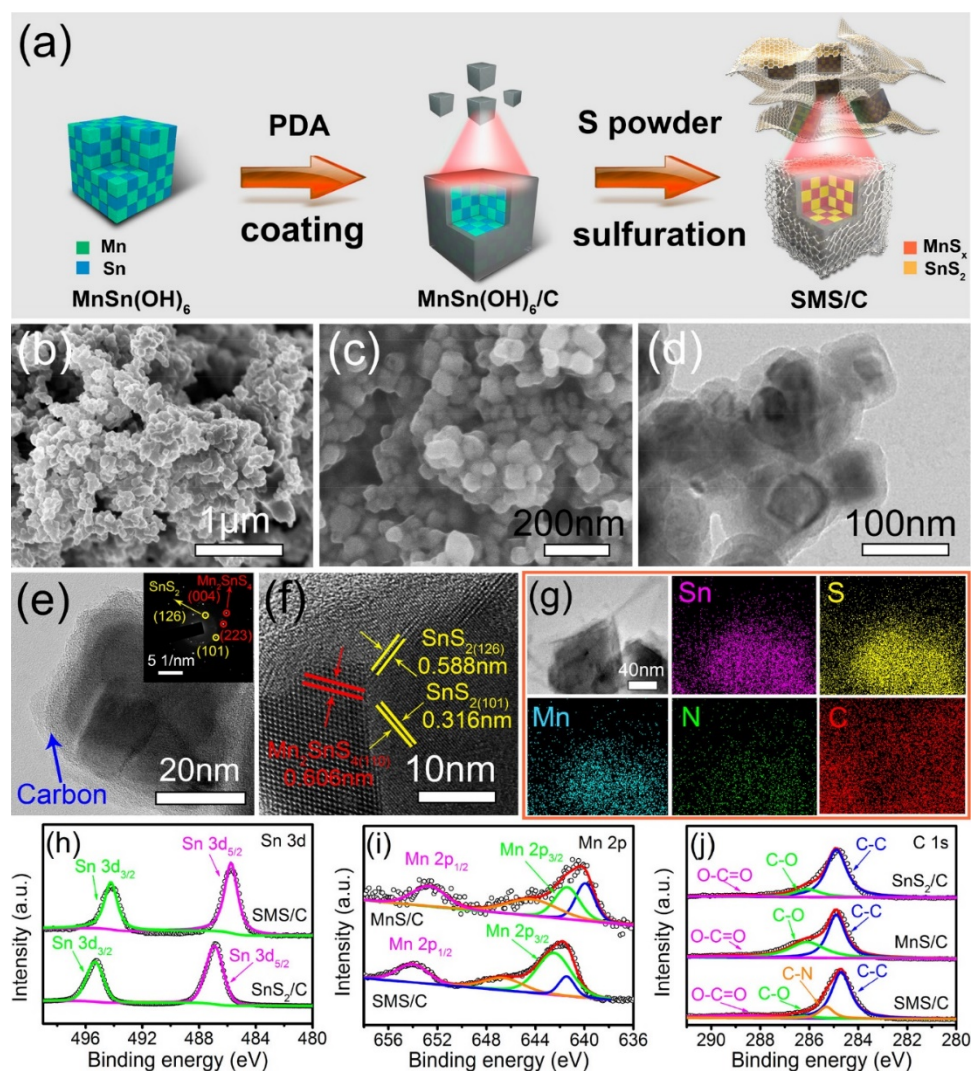


**Figure 1.14** (a) Schematic illustration of the formation of an SMS/C composite, (b, c) SEM, (d) TEM, (e, f) HRTEM, (g) EDX elemental mapping images, and XPS spectra of (h) Sn 3d, (i) Mn 2p, and (j) C 1s for the SMS/C composite [54].

Yuan et al. developed Co vacancies at the interface of an  $\text{CoSe}_2/\text{graphene}$  heterostructure, where the  $\text{Co}_{1-x}\text{Se}_2/\text{graphene}$  heterostructure shows significant  $\text{Na}^+$  intercalation

pseudocapacitance [56]. Density functional theory (DFT) calculations suggest that the introduction of the Co vacancy dramatically increases the  $\text{Na}^+$  adsorption energy and significantly reduces the  $\text{Na}^+$  diffusion barrier (**Figure 1.15**).

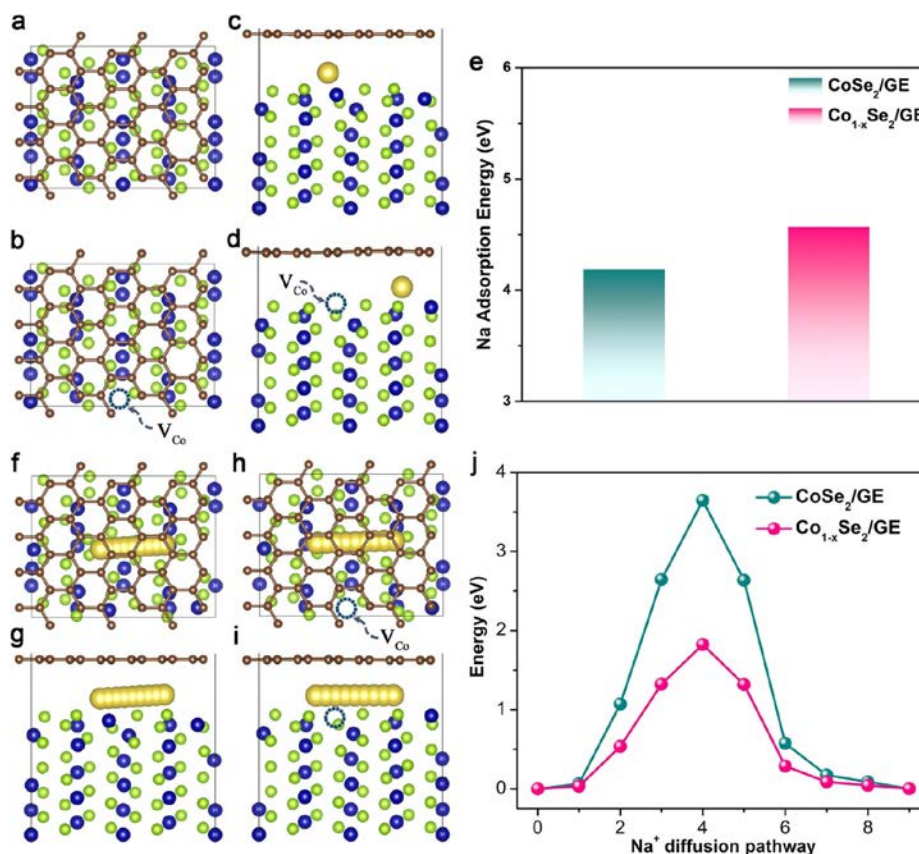


**Figure 1. 15** Theoretical study of the role of the Co vacancies at the atomically thin interface in promoting the  $\text{Na}^+$  storage performance. (a, b) Top views of the optimized  $\text{CoSe}_2/\text{GE}$  and  $\text{Co}_{1-x}\text{Se}_2/\text{GE}$  structures with green Se, blue Co, and brown C. (c, d) Side views of the most stable Na (yellow) adsorption positions at the interfaces of  $\text{CoSe}_2/\text{GE}$  and  $\text{Co}_{1-x}\text{Se}_2/\text{GE}$ . (e) Na adsorption energies. (f–i) Top and side views of Na diffusion pathways at the interfaces of  $\text{CoSe}_2/\text{GE}$  and  $\text{Co}_{1-x}\text{Se}_2/\text{GE}$ . (j) Na diffusion energy barriers [56].

### 1.3 Aqueous zinc-ion batteries

Zinc metal is a promising anode material because of its high theoretical capacity (5855 mA h mL<sup>-1</sup> and 820 mA h g<sup>-1</sup>) and low redox potential (−0.76 V vs the standard hydrogen electrode, SHE) [57-60]. Moreover, zinc's abundance and availability on earth, and its compatibility with nonflammable aqueous electrolytes make zinc batteries safe, environmentally friendly, and cost-effective [61, 62]. Therefore, AZIBs are considered an alternative to LIBs in large-scale energy storage [63, 64].

#### 1.3.1 A brief history of AZIBs

The concept of using zinc as an electrode in a battery has been around for over a century in primary batteries such as Zn-air and Zn-MnO<sub>2</sub> in the alkaline electrolyte system, which shows limited rechargeability. In 2011, Kang et al. reported the reversible Zn<sup>2+</sup> insertion into the tunnel structure of the MnO<sub>2</sub> host used as the cathode in a ZIB for the first time [65]. The team demonstrated that this design could deliver high energy density and power density while maintaining low costs and excellent safety. Since then, research efforts have focused on optimizing the performance of the AZIBs by improving the electrode materials, electrolyte, and battery architecture. In 2017, Wang' group reported the MnO<sub>2</sub> cathode with a consequent H<sup>+</sup> and Zn<sup>2+</sup> insertion/extraction process with high reversibility and cycling stability for the first time [66]. In the same year, a paper published in Nature Communications reported a highly reversible zinc/sodium vanadate (NaV<sub>3</sub>O<sub>8</sub>·1.5H<sub>2</sub>O) system, where NaV<sub>3</sub>O<sub>8</sub>·1.5H<sub>2</sub>O nanobelts serve as positive electrode and zinc sulfate (ZnSO<sub>4</sub>) aqueous solution with sodium sulfate (Na<sub>2</sub>SO<sub>4</sub>) additive is used as electrolyte [67]. Wang et al. reported a crystalline single-ion Zn<sup>2+</sup> solid-state electrolyte (SSE) in 2018, which is designed based on a post-synthetic modified metal–

organic framework (MOF) to improve the performances of AZIBs [68]. In 2020, A MOF was constructed by Zhou's group as front surface layer to maintain a super-saturated electrolyte layer on the Zn anode [69]. Our group has developed a tetrahydrofuran (THF) additive in the  $\text{ZnSO}_4$  electrolyte to decrease the water activity in 2023, which enables highly reversible Zn electrode [70]. The development history of AZIBs has been summarized in **Figure 1.16**.

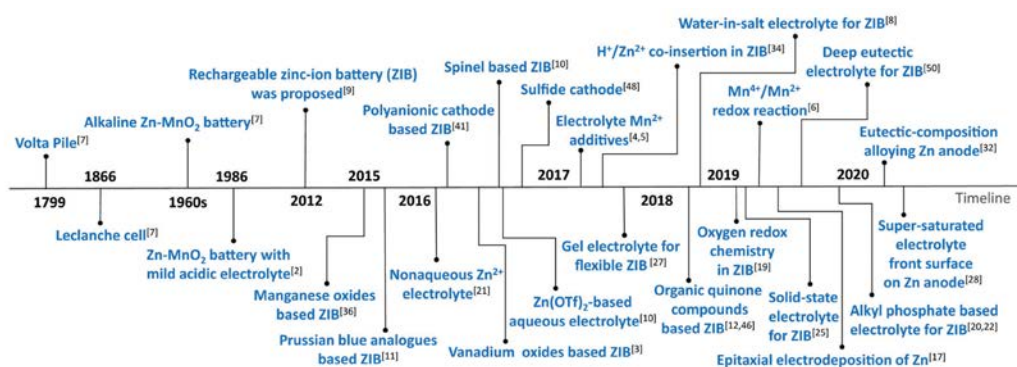


**Figure 1. 16** A brief development history of rechargeable ZIBs [71].

### 1.3.2 Working principle of AZIBs

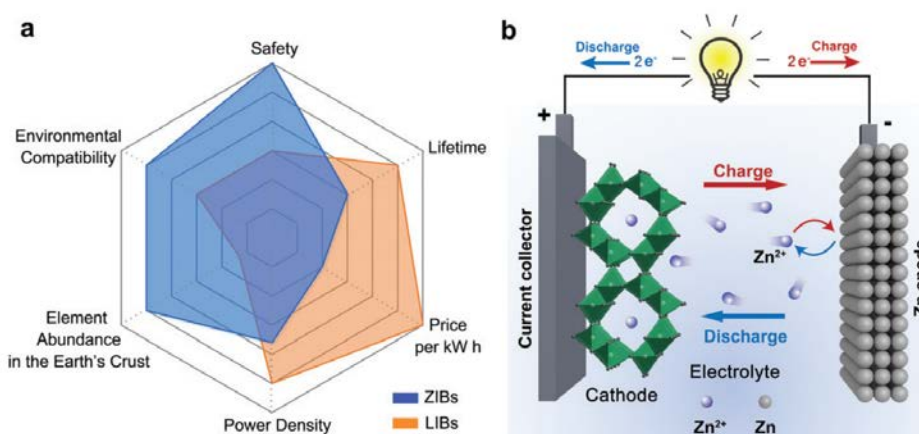
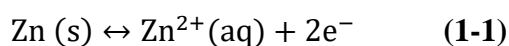


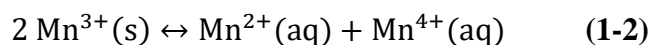
**Figure 1. 17** (a) Multi-angle comparison of ZIBs and LIBs. (b) Schematic illustration of the working principle of the rechargeable ZIBs [71].

The basic components of AZIBs are two electrodes (anode and cathode), an electrolyte and a separator, which is similar to LIBs as shown in **Figure 1.17**. The anode is typically made of metallic Zn, During the charging process, the anode is oxidized to release  $Zn^{2+}$  and electrons. The chemical reaction is shown in **equation (1-1)**. The cathode can be made of various materials such as  $MnO_2$  [72], vanadium oxide ( $V_2O_5$ ) [73], or polyaniline (PANI) [74]. During the charging process,  $Zn^{2+}$  are inserted into the cathode, which results in a reduction of the cathode material. Taking  $MnO_2$  for example, the chemical reaction is shown in **equation (1-2)**. The electrolyte is usually a solution of zinc salts (such as  $ZnSO_4$ ) in water. When the battery is charged, the  $Zn^{2+}$  are oxidized at the anode, releasing electrons that flow through an external circuit to the cathode. At the same time, water is electrolyzed at the anode, producing hydrogen gas and hydroxide ions. The hydroxide ions migrate to the cathode, where they react with the cathode material and the electrons from the anode to form water. During discharge, the reverse process occurs. The  $Zn^{2+}$  from the electrolyte are reduced at the cathode, accepting electrons to form metallic zinc, while the hydroxide ions from the cathode react with the anode to produce water. The overall reaction can be represented as follows:[75]

Anode:



Cathode:

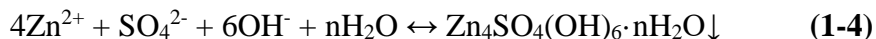


### 1.3.3 The challenges of AZIBs

The aqueous electrolyte can corrode Zn metal electrode during the charging/discharging processes or static state, resulting in poor cycling stability and low coulombic efficiency (CE) [76, 77]. This challenge stems from the interaction between the Zn metal and the aqueous electrolytes as shown in **Figure 1.18**, which causes the decomposition of water to generate hydrogen (H<sub>2</sub>) and produce inactive byproducts on the surface of the Zn electrode [78, 79]. The corrosion mechanism originates from the lower standard electrode potential of Zn<sup>2+</sup>/Zn compared to H<sup>+</sup>/H<sub>2</sub> (0 V vs SHE), thus the hydrogen evolution reaction (HER) occurs easily on the surface of zinc metal electrode in aqueous electrolytes as shown in **equation (1-3)** [80]:



This HER process is accelerated during the zinc deposition process in AZIBs because the potential of the Zn electrode is pushed to more negative values. The HER process also can increase the PH locally in the electrolyte due to the consumption of the protons, thus the byproducts will be generated on the surface of the Zn metal electrode [81]. Taking ZnSO<sub>4</sub> electrolyte as an example, the equation can be explained as follow:



As shown in **equation (1-4)**, the formation of the byproducts can consume the electrolyte salt to change the concentration of the Zn salts, leading to the unstable cycling stability of AZIBs. Moreover, the byproducts on the surface of the Zn electrode show a loose structure with many sheets being stacked together, which can also increase the charge transfer resistance to lower the charge/discharge efficiency, especially at a high current



density. Besides, the byproducts cannot prevent the contact between the Zn electrode and the electrolytes that all the above-mentioned reactions will continue to occur. The side reactions can occur in AZIBs no matter whether the batteries are in use or just at rest, which will greatly deteriorate the electrochemical performance of AZIBs.

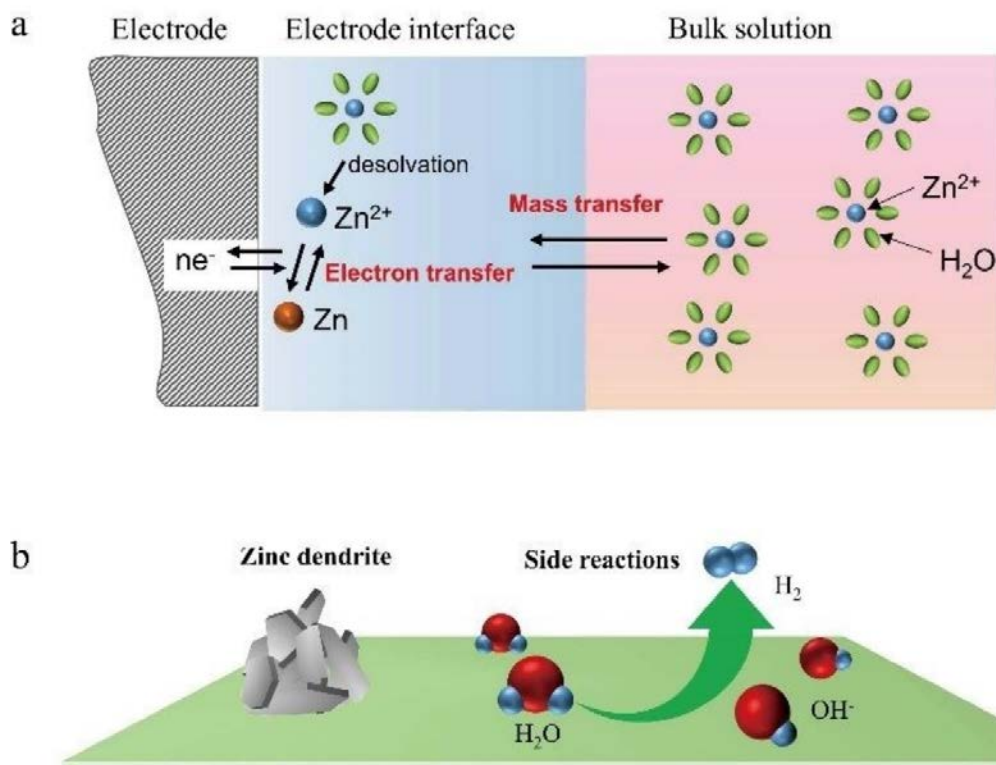


**Figure 1.18** (a) Schematic representation of the deposition/stripping processes of the Zn anode in AZIBs. (b) Schematic illustration of the Zn dendrite and interface side reactions of the Zn anode [82].

### 1.3.4 Recent advances in the electrolyte additives

Many strategies have been proposed to address the issues to improve the electrochemical performance of AZIBs. One idea is to construct the protective layers on the surface of Zn metal electrode, which can provide physical shielding to prevent the Zn electrode from

exposing to the electrolyte [83]. The protective films can also guide homogeneous  $\text{Zn}^{2+}$  diffusion, thus the growth of Zn dendrite will be suppressed. Up to now, many materials have been developed as interfacial films, including organic polymer materials (e.g., polyamide [84], poly (ethylene glycol) [85], polyacrylonitrile [86]), and inorganic materials (e.g., MXene [87],  $\text{TiO}_2$  [88],  $\text{ZrO}_2$  [89],  $\text{MoS}_2$  [90]). For example, Chen et al. reported an artificial interface film of nitrogen-doped graphene oxide (NGO) on the metallic Zn electrode, which was prepared in one step by a Langmuir–Blodgett method (**Figure 1.19**) [78]. The NGO with a parallel and ultrathin structure can suppress the HER and passivation, resulting in a good electrochemical performance. However, the construction of the protective films will add cost and decrease the energy density of AZIBs, which will impede their practical application. Water-in-salt electrolytes (WISEs) with a high molality can reduce the reactivity of the water molecules and extend the electrochemical stability window [91, 92]. Thus, the WISEs can improve the cycling stability and boost Zn electrode reversibility. For example, Gao et al. reported a  $\text{ZnCl}_2/\text{ZnBr}_2/\text{Zn}(\text{OAc})_2$  aqueous electrolyte with record super solubility with a high molality of 75 m attributed to the formation of acetate-capped water salt oligomers bridged by the  $\text{Br}^-/\text{Cl}^--\text{H}$  and  $\text{Br}^-/\text{Cl}^-/\text{O}-\text{Zn}^{2+}$  interactions [93]. This super soluble electrolyte enabled a high reversible capacity and a good CE. However, accompanied by favorable electrochemical behaviors, the WISEs would also cause high cost and high viscosity, resulting in the application being held up. Another line of thought is to introduce the organic/inorganic additives into the electrolytes. Some additives will modulate the solvation structure of the Zn hydration layer to decrease the number of active water molecules [94-97]. Some small organic molecules can partially replace the

water molecule in the solvation sheath to mitigate water decomposition during cycling [57, 98-100]. Wang's group developed a dilute electrolyte by adding dimethyl sulfoxide (DMSO) to suppress water reduction and Zn dendrite growth [95]. The finding showed that DMSO replaces the H<sub>2</sub>O in the Zn<sup>2+</sup> solvation sheath to form a strong H<sub>2</sub>O-DMSO interaction, inhibiting the decomposition of solvated H<sub>2</sub>O. Other additives can form an SEI layer on the surface of zinc metal upon cycling.

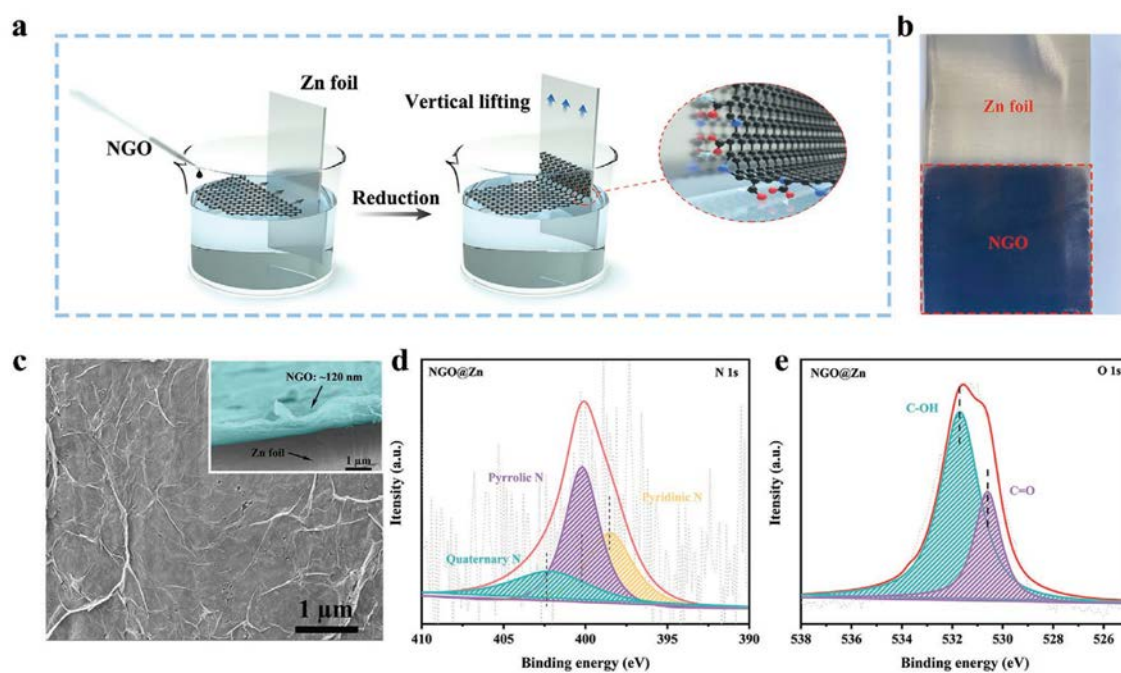


**Figure 1. 19** (a) Schematic illustration of fabricating ultrathin graphene layers on the Zn foil. (b) Optical images of bare Zn foil and NGO@Zn. (c) SEM images of NGO@Zn sample, and the inset image represents the side-views of NGO@Zn. (d) N 1s XPS spectrum of NGO@Zn. The dashed gray and red lines represent the raw and fitted data, respectively. (e) O 1s XPS spectrum of NGO@Zn. The dashed gray and red lines represent the raw and fitted data [78].

## **1.4 Motivation and objectives**

### **1.4.1 Motivation**

To meet the every-growing demands for the LSES, high energy and high safety SIBs and AZIBs are needed to bridge the gap. However, the anodes used in LIBs, including graphite and silicon, fail in SIBs. Thus, the novel anodes with high capacity and good stability need to be developed with facile and scalable methods, and their sodium ions storage mechanism should be clarified. On the other hand, the water-induced side reactions damage the Zn electrode, resulting in limited life span of AZIBs. Screening functional additives for the aqueous electrolytes, which can decrease the water activity and regulate the  $\text{Zn}^{2+}$  solvation structure, are an important strategy to improve the performance of AZIBs.

### **1.4.2 Objectives and outline**

The objective of this dissertation is to create high-capacity Sn-based anodes for SIBs, along with an effective electrolyte additive for AZIBs, that can deliver long cycle life and meet the requirements for the LSES applications. Three different Sn-based anode materials will be prepared and studied in this research. Electrospinning will be used to synthesize CF with high conductivity, where the Sn nanoparticles are embedded inside to form a free-standing electrode. High-temperature synthesis combined with ball-milling process will be conducted to create unique pomegranate structure of the novel  $\text{SnP}_2\text{O}_7$  nanoparticles embedded in the carbon matrix. In addition, the heterostructure  $\text{SnS}/\text{Sb}_2\text{S}_3$  will be prepared and then encapsulated in the S, N co-doped carbon with the engineered porous structure. THF as an additive in aqueous electrolyte will be systematically studied

in AZIBs. The electrochemical performance of the Sn-based anodes for SIBs and electrolyte additives for AZIBs are studied and discussed.

Chapter 2 introduces the preparation of the materials and electrolytes. The material properties will be examined by many characterization methods such as X-ray crystallography (XRD), X-ray photoelectron spectroscopy (XPS), scanning electron microscope (SEM), Fourier-transform infrared spectroscopy (FTIR), thermogravimetric analysis (TGA), Raman spectroscopy, and Brunauer-Emmett-Teller (BET) analysis. The fabrication of the anode electrodes will be introduced and further be used as the working electrode in the cells. This chapter will also introduce the battery test methods such as electrochemical impedance spectroscopy (EIS), cyclic voltammetry (CV), linear polarization, and chronoamperometry (CA).

In chapter 3, three projects of the Sn-based anodes for SIBs will be discussed. A facile and scalable electrospinning method will be used to prepare high-mass-loading free-standing Sn-based anode that the metallic Sn nanoparticles will be uniformly embedded in CF. A novel anode material of  $\text{SnP}_2\text{O}_7$  will be introduced, which can store sodium ions through conversion and alloying reactions. A bimetallic sulfide of  $\text{SnS/Sb}_2\text{S}_3$  will be synthesized to form heterostructure, and then it will be encapsulated in S, N co-doped carbon with the engineered porous structure. The material properties and electrochemical performance of these Sn-based anodes will be investigated.

In chapter 4, the electrolyte design will be used to boost the performance of AZIBs. The organic additive of THF will be added to the  $\text{ZnSO}_4$  electrolyte. The comparison of the baseline  $\text{ZnSO}_4$  electrolyte and the optimized  $\text{ZnSO}_4/\text{THF}$  5% electrolyte will provide the advantages of the THF additive. The ex-situ XRD and SEM characterizations will

demonstrate that the THF additive have the ability to suppress the water-induced side reactions.

Chapter 5 summarizes the findings and significance of this dissertation. Future works are proposed that may make the project more advanced. Strategies to fabricate advanced electrode materials for SIBs and screening new electrolyte additives for AZIBs are also proposed.

## Chapter 2 Experimental procedures

### 2.1 Materials and preparation

#### 2.1.1 Preparation of the Free-Standing Sn@CFC electrode

Firstly, 474 mg of tin (II) chloride ( $\text{SnCl}_2$ , Sigma Aldrich) was dissolved into 5 mL of N, N-dimethylformamide (DMF). Then, 265 mg of sodium carbonate ( $\text{Na}_2\text{CO}_3$ , Sigma Aldrich) was added slowly to the solution followed by stirring 1 h. After that, 300 mg of polyacrylonitrile (PAN, Sigma Aldrich) was dispersed into the obtained light-yellow solution to form a homogeneous  $\text{SnO}/\text{PAN}$  mixture under vigorous stirring for 10 h. The mixture was stood still for another 1 h and the as-obtained supernatant was used as the precursor for electrospinning.

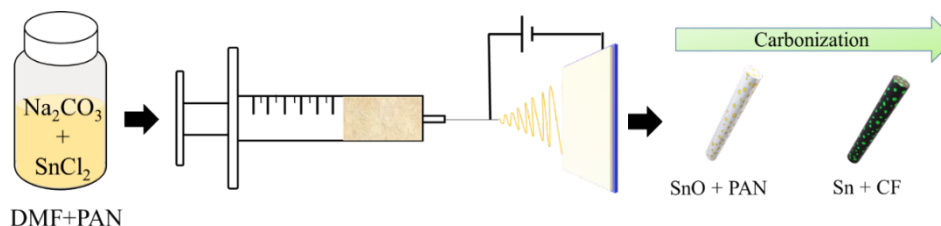


**Figure 2. 1** Schematic illustration of the synthesis of the free-standing Sn@CFC electrode.

The precursor solution was loaded into a 3 mL syringe pump with a flattop stainless-steel needle and spun at a rate of  $0.5 \text{ mL h}^{-1}$ . A voltage of 10 kV and a distance of 10 cm between the needle and the aluminum substrate was applied for the electrospinning process. Then, the resultant fibers were further stabilized in a tube furnace at  $200 \text{ }^\circ\text{C}$  with a heating rate of  $5 \text{ }^\circ\text{C min}^{-1}$  in the air for 30 mins, followed by annealing at  $600 \text{ }^\circ\text{C}$  for 3 hours with a heating rate of  $5 \text{ }^\circ\text{C min}^{-1}$  under argon (Ar) atmosphere. The product was

washed three times by deionized water to remove the impurities. After being dried at 60 °C under vacuum overnight, the final desired Sn@CFC sample was obtained. **Figure 2.1** schematically illustrates the synthesis processes of the Sn@CFC sample.

### 2.1.2 Synthesis of SnP<sub>2</sub>O<sub>7</sub>@C

The precursor of Sn(HPO<sub>4</sub>)·2H<sub>2</sub>O was prepared by a hydrothermal method. Typically, 4 mL of H<sub>3</sub>PO<sub>4</sub> (85%), 6.8 g of sucrose, and 7 g of SnCl<sub>4</sub>·5H<sub>2</sub>O were added to 40 mL distilled water under stirring. Next, a 100 mL Teflon-lined autoclave was used to carry out the hydrothermal reaction at 180 °C for 24 h. The viscous and black product was collected by centrifugation. Then the distilled water and ethanol were used to wash the product three times. Finally, the white SnP<sub>2</sub>O<sub>7</sub> sample was obtained by calcining Sn(HPO<sub>4</sub>)·2H<sub>2</sub>O in air at 800 °C for 5 h. Then, two grams of the as-synthesized SnP<sub>2</sub>O<sub>7</sub> sample was mixed with 2 g of PAN by ball-milling at 400 rpm for 12 h to disperse the SnP<sub>2</sub>O<sub>7</sub> nanoparticles in the PAN matrix. Thereafter, the SnP<sub>2</sub>O<sub>7</sub>@PAN mixture was heated at 600 °C for 3 h in Ar atmosphere with a heating rate of 5 °C min<sup>-1</sup> to get the composite SnP<sub>2</sub>O<sub>7</sub>@C sample. **The processes are shown in Figure 2.2.**

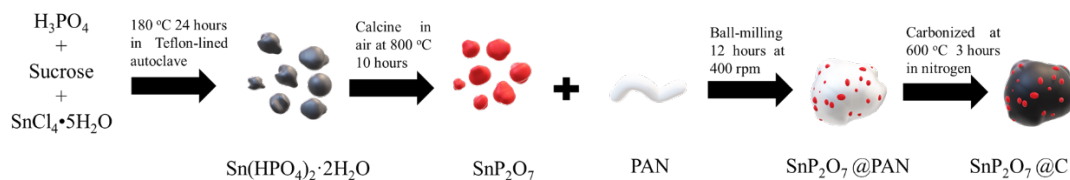


**Figure 2. 2** Schematic illustration of the synthesis of the SnP<sub>2</sub>O<sub>7</sub>@C anode.



### 2.1.3 Preparation of SnS/Sb<sub>2</sub>S<sub>3</sub>@SNC

The ultrafine SnSb<sub>x</sub> alloy was synthesized by a chemical precipitation method. Typically, 3.8 g of SnCl<sub>2</sub>, 1.52 g antimony trichloride (SbCl<sub>3</sub>), and 19 g of trisodium citrate dihydrate were dissolved in 500 mL of deionized water to form a solution A. 2 g of sodium hydroxide (NaOH) and 2 g of sodium borohydride (NaBH<sub>4</sub>) were dissolved in 350 mL of deionized water to form solution B. Then solution B was added into solution A slowly under stirring and then the black product of SnSb<sub>x</sub> alloy was generated. The SnSb<sub>x</sub> nanoparticles were collected by vacuum filtration and further washed by deionized water three times and ethanol three times. After being dried in the vacuum oven at 100 °C 12 h, the desired product of the SnSb<sub>x</sub> alloy was obtained. After that, one gram of the as-prepared SnSb<sub>x</sub> particles were mixed with 1 g of PAN and 1 g of sulfur (S) to achieve composite SnSb<sub>x</sub>@PAN@S by a ball-milling process with a rotation speed of 400 rpm for 12 h. After that, the SnSb<sub>x</sub>@PAN@S mixture was calcined in the tube furnace under a nitrogen atmosphere at 600 °C for 3 h with a heating rate of 5 °C min<sup>-1</sup>. The final product of SnS/Sb<sub>2</sub>S<sub>3</sub>@SNC with porous structure was obtained after cooling down to the room temperature. **Figure 2.3** shows the whole synthesis processes.

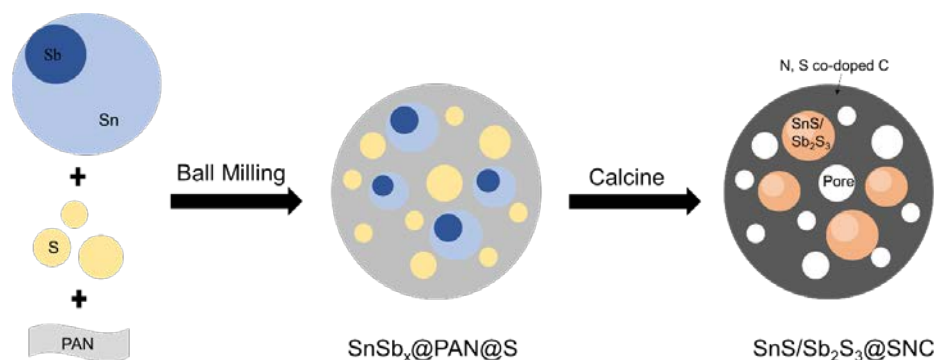


**Figure 2. 3** Schematic illustration of the synthesis processes of SnS/Sb<sub>2</sub>S<sub>3</sub>@SNC.

#### **2.1.4 Preparation of the electrolyte for AZIBs**

To prepare the baseline 2 M ZnSO<sub>4</sub> electrolyte, 11.5 g of ZnSO<sub>4</sub>·7H<sub>2</sub>O was dissolved in 14.96 mL of deionized water. For THF-based electrolytes, different amounts of THF were added and volume ratios of THF in the solvent are 2.5, 5, 7.5, and 10%. The relevant electrolytes were denoted as 2 M ZnSO<sub>4</sub>/THF 2.5%, 2 M ZnSO<sub>4</sub>/THF 5%, 2 M ZnSO<sub>4</sub>/THF 7.5% and 2 M ZnSO<sub>4</sub>/THF 10%, respectively.

### **2.2 Electrochemical measurements**

#### **2.2.1 Anode electrode fabrication for SIBs**

For the Sn@CFC sample, it can be used as electrode directly without adding binder and carbon black. The Sn@CFC sample was cut into a 12 mm circular disc as the working electrodes.

For the SnP<sub>2</sub>O<sub>7</sub>@C anode and the SnS/Sb<sub>2</sub>S<sub>3</sub>@SNC anode, the slurry method is used to prepare electrode. The working electrode was made by mixing anode materials, sodium carboxymethyl cellulose (CMC), and carbon black (Super-P) with a weight ratio of 8: 1: 1. After adding deionized water and stirring 24 h, the homogeneous slurry was cast uniformly on the copper (Cu) foil. After drying, the electrode was punched into 12 mm circular discs.

#### **2.2.2 Cell assembly and testing for SIBs**

The CR 2035-coin cells were assembled in an argon-filled glovebox with as-prepared electrode as working electrode, 12 mm sodium foil as the counter electrode, 1.0 M NaClO<sub>4</sub> in EC: DMC (1:1 v/v) with 5% FEC as the electrolyte, and a polypropylene film (Celgard-2325) was used as a separator. The electrochemical properties of the electrodes were studied with a multichannel battery-testing system (Neware CT-4008, Shenzhen

Neware Co., China). EIS was tested using a VSP (Bio-Logic SAS, France) electrochemical workstation at 25 °C with the frequency ranging from 1 MHz to 0.001 Hz and an AC signal of 10 mV in amplitude as the perturbation. CV was carried out using VSP (Bio-Logic SAS, France) electrochemical workstation.

### **2.2.3 Cell assembly and testing for AZIBs**

For the Zn symmetrical cell test, the CR-2035 cell was assembled in the air with two Zn chips with a diameter of 12 mm, 100  $\mu$ L of the electrolyte, and glass fiber as a separator. The CE was measured in a Zn||Cu cell with Cu foil as the counter electrode, performed at 1 mA  $\text{cm}^{-2}$  with a capacity of 1 mA h  $\text{cm}^{-2}$ . For the Zn||MnO<sub>2</sub> full cell, the cell was assembled into CR-2035-type cells in the air with a zinc chip as the counter electrode. 0.1 M MnSO<sub>4</sub>, which can balance the dissolution loss of MnO<sub>2</sub>, was added to the electrolytes. The galvanostatic Zn plating/stripping in the Zn symmetrical cell, Zn||Cu half-cell, and Zn||MnO<sub>2</sub> full cell was tested using a Neware CT-4008 battery-testing system. The CV, EIS, linear polarization, and CA measurements were carried out on the electrochemical workstation (Bio-Logic SAS).

### **2.3 Material characterizations**

The XRD was conducted by a Rigaku SmartLab diffractometer, and the Raman spectrum was carried out by LabRAM HR (HORIBA, 532 nm UV laser). TGA was performed with a Perkin Elmer DSC 6000 System instrument. The morphology characterization (SEM, TEM and EDS elemental mapping) was performed using scanning electron microscopy (FESEM, Hitachi, S-4700) and transmission electron microscopy (JEM-2100 LaB<sub>6</sub>, JEOL). XPS was characterized on an X-ray Photoelectron Spectrometer (Thermo Scientific). FTIR spectra were recorded on an infrared instrument of Nicolet 6700

(Thermo Scientific). BET was conducted by the ASAP 2460 surface area and porosimetry analyzer. The contact angle was measured using the VCA2000 video contact angle system. For the in-situ optical observation, the Nikon Eclipse TS2 optical microscope was used.

## 2.4 Density functional theory simulations<sup>1</sup>

All calculations in this study are performed by Vienna Ab Initio Simulation Package (VASP), which is a plane wave-based density functional theory (DFT) code.[101, 102] Projector Augmented Wave (PAW) approach is used to describe the electron-ion interaction, and Perdew-Burke-Ernzerhof (PBE) functional with Generalized Gradient Approximation (GGA) is used for exchange correlation.[103] The size of the supercell is chosen to be  $20\text{\AA}\times 20\text{\AA}\times 20\text{\AA}$ , while the k-points sampling is set as  $(2\times 2\times 2)$  with an automatically generated mesh in the first Brillouin Zone.[104] Cutoff energy of 400eV is used for all the calculations and the energy convergence criterion for the structural optimization is  $10^{-6}$  eV. Van der Waals correction has been considered in all calculations. The solvation energy ( $E_{sol}$ ) of the  $\text{Zn}^{2+}$  ion in an aqueous electrolyte with/without the addition of THF is calculated as follows:[105]

$$E_{sol} = E_{total} - E_{\text{H}_2\text{O}/\text{THF}+\text{H}_2\text{O}} - E_{\text{Zn}^{2+}} \quad (2-1)$$

where  $E_{total}$  is the total energy of the  $\text{Zn}^{2+}$  solvation structures configured with  $\text{H}_2\text{O}$  and THF molecules.  $E_{\text{H}_2\text{O}/\text{THF}+\text{H}_2\text{O}}$  and  $E_{\text{Zn}^{2+}}$  are the energies of the  $\text{H}_2\text{O}/\text{H}_2\text{O}+\text{THF}$  molecule clusters and the isolated  $\text{Zn}^{2+}$  ion, respectively.

---

<sup>1</sup> This part was conducted by Yao Ren, and Yao Ren and Wei He write the manuscript.

## Chapter 3 Material Engineering of the Sn-based anodes for sodium-ion batteries

### 3.1 Free-standing Sn@CFC anode<sup>2</sup>

#### 3.1.1 Introduction

Downsizing the Sn particles to the nanoscale has been demonstrated to be an effective way to alleviate strain during the large volume changes and improve the cycling stability [106-108]. The nano-size Sn materials can be further modified by coating with carbon materials, which act as a buffer layer to mitigate fracture during volume changes, enhance mechanical integrity, and improve electrical conductivity. However, it is still a big challenge to employ conventional methods to fabricate nano-size Sn/C with high mass loading although it is significant for high gravimetric or volumetric energy density based on the whole cell. It is noted that the reported mass loading of the common anode of SIBs in the state-of-art (SOA) literature is smaller than  $2 \text{ mg cm}^{-2}$  [109-112]. Second, Sn/C electrodes fabricated by the traditional roll-to-roll coating process are easily delaminated from the current collector due to their weak adhesion [113, 114]. Moreover, it is difficult for the electrolyte to diffuse into the electrode with a high mass, resulting in a considerable increase in the cell impedance and the loss of energy efficiency [114, 115]. Therefore, it is desired to develop scalable manufacturing techniques to synthesize nano-

---

<sup>2</sup> This section in full is a reprint of the paper “High-mass-loading Sn-based anode boosted by pseudocapacitance for long-life sodium-ion batteries.” as it appears in the *Chemical Engineering Journal* **414: 128638**, Wei He was the primary investigator and first author of this paper.

size Sn/C without a current collector by reducing manufacturing steps and costs, enabling applications for large-scale energy storage systems.

In this project, we developed an advanced anode with nano-sized metallic Sn nanoparticles finely decorated on the carbon fiber cloth (Sn@CFC) by a scalable electrospinning method. This unique process produces Sn@CFC electrode with an extremely high mass loading of  $5.5 \text{ mg cm}^{-2}$  and homogeneous nanomorphology. The ultrasmall Sn particles can shorten the diffusion pathway of ions and electrons and can alleviate strain during sodiation/desodiation. Moreover, the carbon fibers with nitrogen doping not only provide the electrons and ions transfer path to dramatically enhance the conductivity but also act as the buffer layer to keep the structure of metallic Sn particles stable during the volume variation.

### 3.1.2 Material characterizations of Sn@CFC

**Figure 2.1** schematically illustrates the synthesis processes of the Sn@CFC sample. **Figure 3.1 a-c** shows SEM images of the as-prepared Sn@CFC sample. As shown in **Figure 3.1 a**, the Sn@CFC sample exhibits a 3D cross-linked structure. In addition, Sn@CFC is freestanding and flexible (**inset of Figure 3.1 a**), which can be directly used as an electrode material without a binder and a current collector. From **Figure 3.1 c-d**, the fiber in the Sn@CFC sample has a uniform diameter around 300 nm, and the surface of the Sn@CFC sample is rough with Sn nanoparticles successfully embedded in CF. The microstructure of Sn@CFC is further investigated by TEM, as shown in **Figure 3.1 d-f**. From the **Figure 3.1 d-e**, the images further confirm the structure of the Sn@CFC sample and agree with the SEM results that the diameter of the fibers are almost the same and Sn nanoparticles can be observed both on the surface and inside of the fiber. The particle

size of metallic Sn is around 10 nm from the HRTEM image of **Figure 3.1f**. The EDS elemental mapping is shown in **Figure 3.2** that the Sn and C element are overlapping very well, suggesting that Sn nanoparticles are evenly distributed in CF.

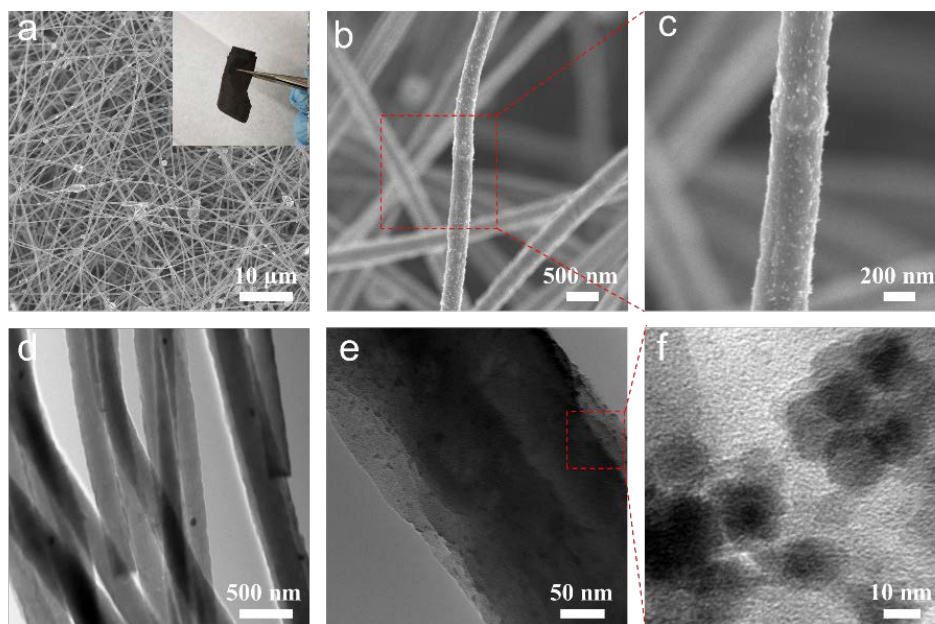


**Figure 3. 1** Morphology characterization of Sn@CFC. (a-c) SEM images, (d, e) TEM images, (f) high-resolution TEM image

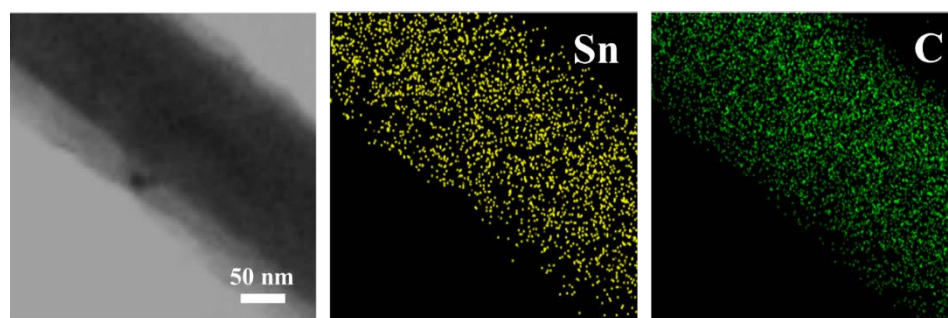


**Figure 3. 2** STEM image with the corresponding EDS elemental mappings of Sn@CFC.

The crystal structure of Sn@CFC was characterized by XRD measurement. As shown in **Figure 3.3 a**, all the intense and instinct peaks can be indexed into tetragonal phase of the

metallic Sn ( $\beta$ -Sn, JCPDS card no.04-0673), and a weak broad peak between  $20^\circ$  to  $30^\circ$  is attributed to the amorphous carbon material. No other peaks of the impurities are detected in the XRD pattern, indicating that the final product is made by metallic Sn and amorphous carbon. The amorphous carbon was further confirmed and studied by Raman spectra. **Figure 3.3 b** shows two peaks located at  $1341\text{ cm}^{-1}$  and  $1590\text{ cm}^{-1}$  in the Raman spectra, corresponding to D and G bands of amorphous carbon fiber, respectively.  $I_D/I_G$ , the intensity ratio of D band and G band that represented the defect quantity for CF was calculated as 1.49. The high ratio of  $I_D/I_G$  indicates a large number of defects in the carbon material, which are capable of improving the electrochemical performance by adsorbing more  $\text{Na}^+$  to increase capacity. To detect the weight content of Sn in the composite, TGA was performed in air from  $25$  to  $800^\circ\text{C}$ . The TGA curve of Sn@CFC in **Figure 3.3 c** shows an upward trend and over 100% until  $420^\circ\text{C}$ , which is attributed to the oxidation of the metallic Sn ( $\text{Sn} + \text{O}_2 \rightarrow \text{SnO}_2$ ). After that, the CF start to decompose to  $\text{CO}_2$  ( $\text{C} + \text{O}_2 \rightarrow \text{CO}_2$  (gas)), and the TGA curve displays a general trend of decrease. According to the calculation, the content of Sn is 46.7 wt.%.

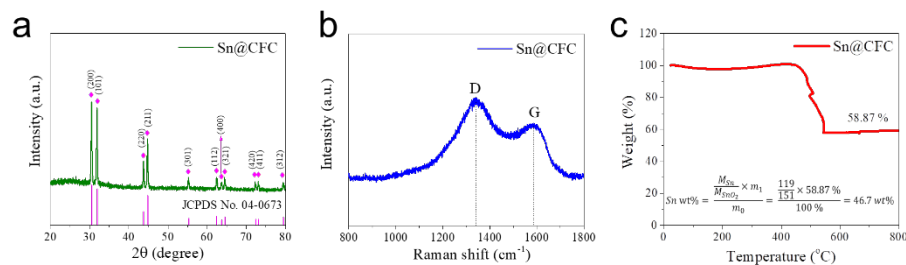


**Figure 3.3** (a) XRD pattern, (b) Raman spectra and (c) TGA curve of Sn@CFC.



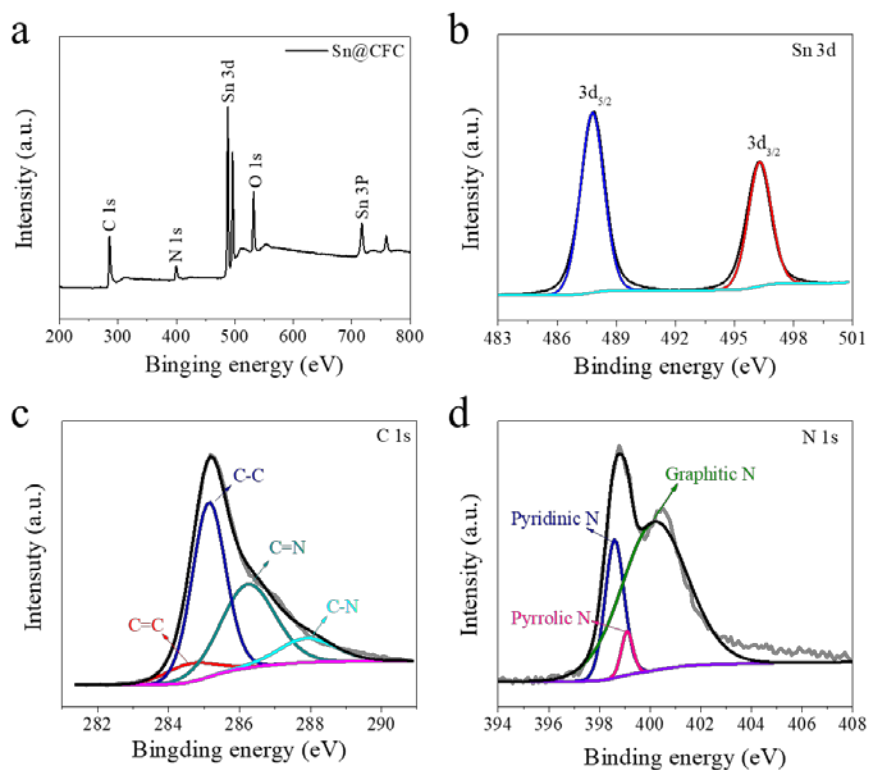


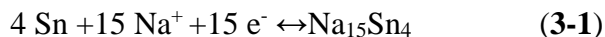
**Figure 3. 4** XPS spectra of Sn@CFC.

The chemical bonding situation of the Sn@CFC sample was analyzed by XPS. The survey XPS spectrum in **Figure 3.4 a** suggests the existence of the Sn, C, N and O elements in the sample. The high-resolution C 1s spectrum (**Figure 3.4 c**) can be fitted into four peaks at 284.6, 285.2, 286.3 and 287.9 eV originating from C=C, C-C, C=N and C-N, respectively, demonstrating the successful doping of the N atoms in CF. The N-doping is also confirmed by the high-resolution N 1s spectrum (**Fig. 3.4 d**), which shows the existence of the pyridinic N (398.5 eV), pyrrolic N (399.1 eV) and graphitic N (400.2 eV). The nitrogen doping is expected to improve the conductivity of CF to optimize its charge transfer kinetics. As shown in **Figure 3.4 b**, there is a pair of characteristic peaks in the high-resolution Sn 3d spectrum at 496.3 and 487.8 eV from Sn

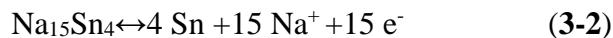
$3d_{3/2}$  and Sn  $3d_{5/2}$ , respectively. The binding energy of Sn $3d_{3/2}$  mainly ascribes to Sn $^{4+}$ , indicating that the surface of the Sn nanoparticles is oxidized due to the exposure in air.

### 3.1.3 Electrochemical characterizations of Sn@CFC

The electrochemical properties of the Sn@CFC electrode for SIBs were systematically studied. The CV curves of the initial three cycles at  $0.1 \text{ mV s}^{-1}$  are shown in **Figure 3.5** with a voltage range from 0.01 - 2 V. In the first cathodic scan, there is a board peaks between 1.2 V to 0.6 V, which could be ascribed to the formation of the solid electrolyte interphase (SEI) layer at the electrode/electrolyte interface. During the subsequent cathodic process, a sharp redox peak below 0.5 V corresponds to the formation of the Na $_{15}$ Sn $_4$  phase.



By comparison, the anodic peak at 0.8 V is observed, suggesting the reversible desodiation reaction of Na $_{15}$ Sn $_4$  phase to the metallic Sn.



Both cathodic and anodic curves almost overlap in the following CV scans, indicating the high reversibility and good stability of the Sn@CFC electrode.

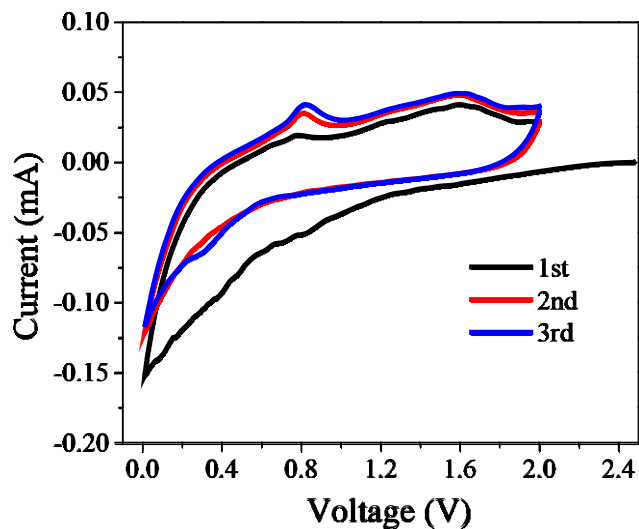


**Figure 3. 5** CV curves of Sn@CFC at a scan rate of  $0.1 \text{ mV s}^{-1}$ .

Ex situ XRD patterns of Sn@CFC at different charge-discharge states are used to further specify the electrochemical reactions. **Figure 3.6 a** shows the first discharge/charge voltage profile of the Sn@CFC electrode at a low current density of  $20 \text{ mA g}^{-1}$ . There is a small plateau around  $1.2 \text{ V}$  on the discharge curve, which can be attributed to the formation of SEI film, with the agreement of the CV curve above. The voltage of Sn@CFC electrode then rapidly drops to  $0.5 \text{ V}$  and enters into a long and flat voltage plateau to form the  $\text{Na}_{15}\text{Sn}_4$  phase. In the charge profile, two potential plateaus exhibited at  $0.3 \text{ V}$ ,  $0.8 \text{ V}$  are the dealloying processes from the  $\text{Na}_{15}\text{Sn}_4$  phase to metallic Sn. Ex situ XRD patterns of Sn@CFC at different charge-discharge states are shown in **Figure 3.6 b**. When the Sn@CFC electrode is discharged to  $0.5 \text{ V}$ , a new phase of  $\text{Na}_{15}\text{Sn}_4$  is observed, indicating the alloying reaction between the metallic Sn and  $\text{Na}^+$  occurs following **equation (3-1)**. After fully discharged to  $0.01 \text{ V}$ , all peaks belong to the  $\text{Na}_{15}\text{Sn}_4$  phase. When the electrode is charged back, the peaks of Sn reappear at  $0.5 \text{ V}$ ,

suggesting the dealloying process from  $\text{Na}_{15}\text{Sn}_4$  to Sn based on the **equation (3-2)**. No alloying phase of  $\text{Na}_{15}\text{Sn}_4$  can be detected after the electrode is charged to 1.5 V.

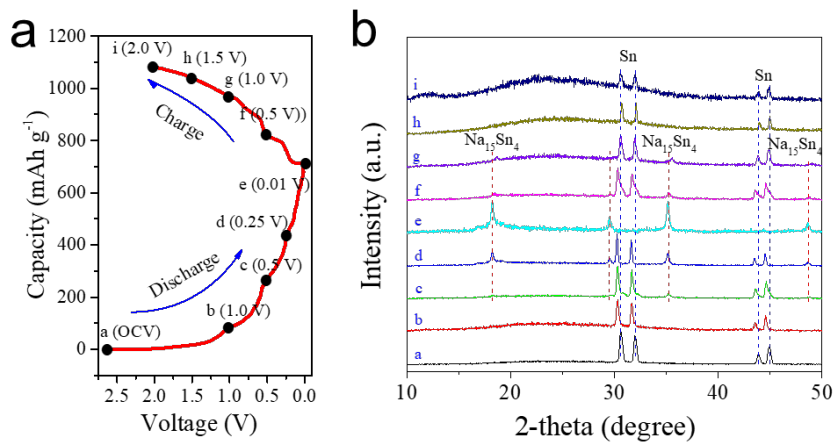


**Figure 3. 6** (a) Galvanostatic discharge/charge profiles at the first cycle. (c) Ex situ XRD patterns of Sn@CFC at different charge-discharge states.

**Figure 3.7 a** shows the electrochemical cycling performance of the Sn@CFC electrode at a current density of  $50 \text{ mA g}^{-1}$ . To demonstrate the excellent structure-property correlation of our Sn@CFC anode. The free-standing CFC electrode was prepared as same as Sn@CFC without metallic Sn for comparison. The first discharge capacity of Sn@CFC electrode is  $716 \text{ mA h g}^{-1}$  with initial CE of 42.25 %. However, after that, the CE rise quickly to 92% in the second cycle and top to about 100% in the tenth cycle. The large capacity loss during the first cycle may be due to the formation of an irreversible SEI layer on the surface of the electrode. The Sn@CFC electrode displays an excellent discharge capacity of  $255 \text{ mA h g}^{-1}$  after 200 cycles, with an excellent CE of 99.94%. In particular, the capacity retention is 83.7% from 2nd to 200th cycle, indicating the superior cyclic stability of the Sn@CFC anode. As a comparison, the CFC electrode shows poor cycling performances with a very low capacity. The low capacity of CFC

indicates that its contribution to the capacity of the Sn@CFC electrode can be negligible. It is noted that the advanced Sn@CFC electrode fully makes use of the huge synergies of the Sn nanoparticles and the cross-link CF, giving rise to the excellent electrochemical performances. Specifically, the Sn nanoparticles can alleviate the strain driving from the large volume change and cross-link CF can act as a buffer layer to keep the structure stable. In addition, the CF prevents the direct contact between the Sn nanoparticles and the electrolyte, reducing the repeated formation of SEI film upon cycling. **Figure 3.7 b** shows the 1st, 2nd, 20th and 200th charge/discharge voltage profiles of the Sn@CFC electrode at 50 mA g<sup>-1</sup>. The discharge/charge voltage plateaus of 2nd, 20th and 200th are nearly overlapped, revealing that the free-standing Sn@CFC anode has a stable and reversible electrochemical behavior.

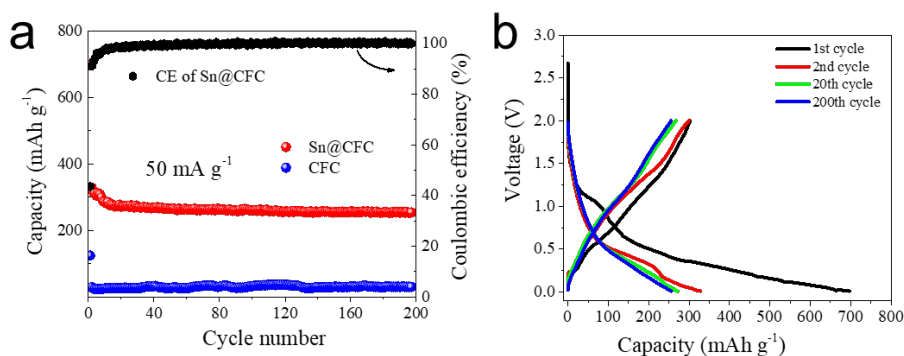


**Figure 3.7** (a) Cycling performance at 50 mA g<sup>-1</sup>. (b) Galvanostatic discharge/charge profiles at 50 mA g<sup>-1</sup>.

The cross-link CF also serves as a pathway to transport electrons and ions to increase the conductivity of the Sn@CFC electrode while Sn nanoparticles can shorten the diffusion pathway of the sodium ions, resulting in good rate capability as shown in **Figure 3.8**. The rate performance of Sn@CFC was tested at various current densities from 50 to 1000 mA

$\text{g}^{-1}$ . The Sn@CFC electrode provides a high discharge capacity of  $310 \text{ mA h g}^{-1}$  at  $50 \text{ mA g}^{-1}$ ,  $246 \text{ mA h g}^{-1}$  at  $200 \text{ mA g}^{-1}$ ,  $170 \text{ mA h g}^{-1}$  at  $500 \text{ mA g}^{-1}$ . Even at a very high current density of  $1000 \text{ mA g}^{-1}$ , the Sn@CFC anode still delivers a capacity of more than  $100 \text{ mA h g}^{-1}$ , holding the high potential for the fast-charging applications. Furthermore, a capacity of more than  $300 \text{ mA h g}^{-1}$  can be retained when the current density drops back to  $50 \text{ mA g}^{-1}$  after various current densities, indicating that the Sn@CFC anode has an excellent rate performance.

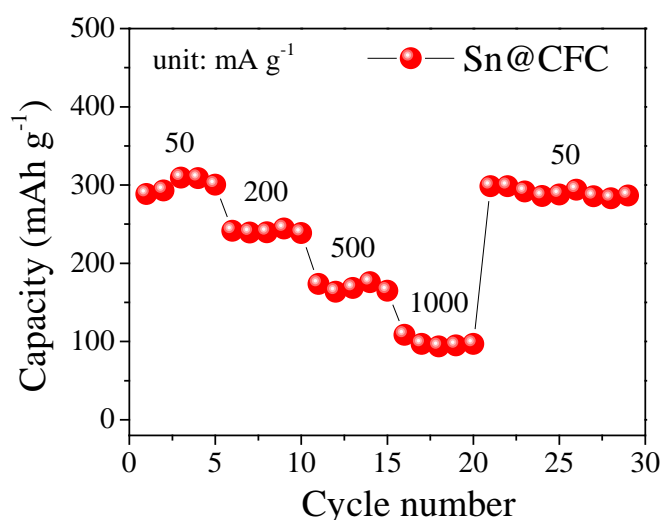


**Figure 3. 8** Rate performance of Sn@CFC at various rates (50–1000  $\text{mA g}^{-1}$ ).

SIBs are suitable for the LSES applications. Hence, it is essential to develop electrodes with both high mass loading and excellent electrochemical performance, especially for a long life span to meet the requirement of maintenance-free or maintenance-little energy storage devices. The as-prepared Sn@CFC electrodes without current collector based on our scalable manufacturing technique can achieve both high mass loading and long cycle life. The long-life performance of the Sn@CFC electrode with high mass loading of 5.5

$\text{mg cm}^{-2}$  is investigated at a high current density of  $200 \text{ mA g}^{-1}$  for 1000 cycles after the activation at a small current density of  $50 \text{ mA g}^{-1}$  for the initial two cycles. As shown in **Figure 3.9**, after cycling up to 1000 cycles, the Sn@CFC electrode delivers a high areal capacity of  $1 \text{ mA h cm}^{-2}$  and the capacity retention of the Sn@CFC electrode is more than 80% from 3rd to 1000th cycle, with an average loss over 1000 total cycles of only 0.02% per cycle, indicating excellent cycling stability.

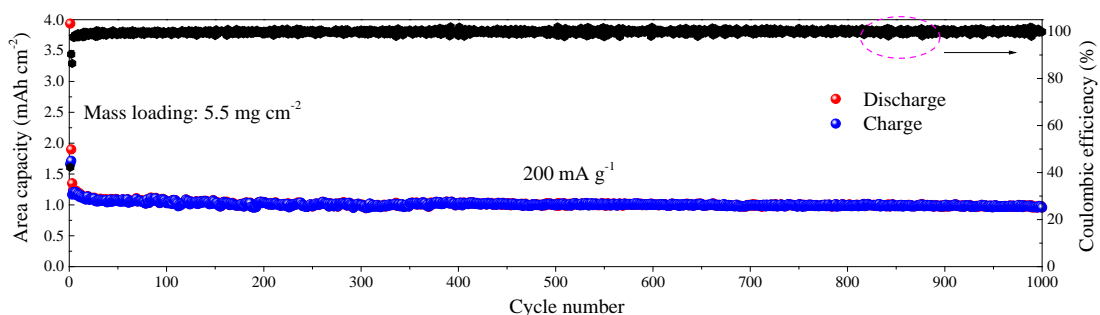


**Figure 3. 9** Long-term cycling performance at  $200 \text{ mA g}^{-1}$  with high mass loading of  $5.5 \text{ mg cm}^{-2}$ .

**Figure 3.10** shows the structure revolution schematic of the free-standing Sn@CFC electrode. The free-standing Sn@CFC electrode with high mass loading can keep the structure stable after long cycling life, profiting from the cross-link 3D structure and Sn nanoparticles. First, CF can act as the channels for both electrons and ions to greatly improve the conductivity of the electrode and diffusion speed of  $\text{Na}^+$ . Hence, it can significantly reduce the polarization effects to make sure more active materials involving electrochemical process in a thick electrode. Second, the CF skeleton has a cross-link 3D structure that can form strong adhesion between the fibers to prevent the electrode delamination, and the free-standing design can make electrolyte penetration through a

thick electrode easily. Third, the ultrasmall particle can mitigate the strain generated from the alloying and dealloying processes and CF can buffer the volume expansion, which in turn enable that the Sn nanoparticles embedded in CF do not crush and aggrerate to ensure excellent cycling performance. Hence, the Sn@CFC electrode prepared by the scalable electrospinning technique offers a promising route to synthesize high-mass-loading electrode for SIBs to satisfy the demand in the LSES application.

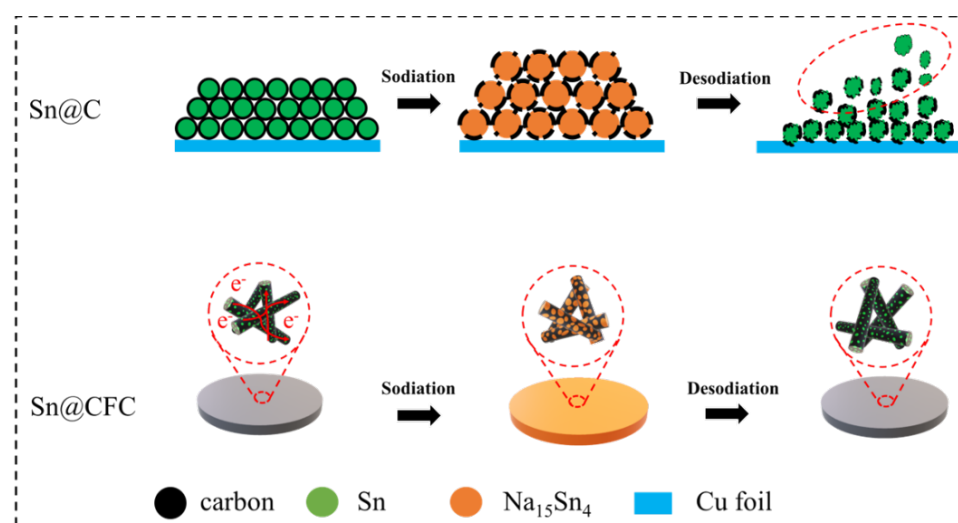


**Figure 3. 10** Schematic illustration of the structure revolution of the free-standing Sn@CFC electrode.

To better understand the structure stability of the Sn@CFC electrode after long cycling life, the electrode was taken out from the cell after 200 cycles at  $200 \text{ mA g}^{-1}$  with the battery charged to 1.0 V and washed by the DMC solution to clear the electrolyte coating on the surface of the electrode. The photographs of the free-standing Sn@CFC electrode after 200 cycles are provided in **Figure 3.11**. The electrode has an integrated structure without any crush compared to the electrode before the cycle, and it shows great flexibility.



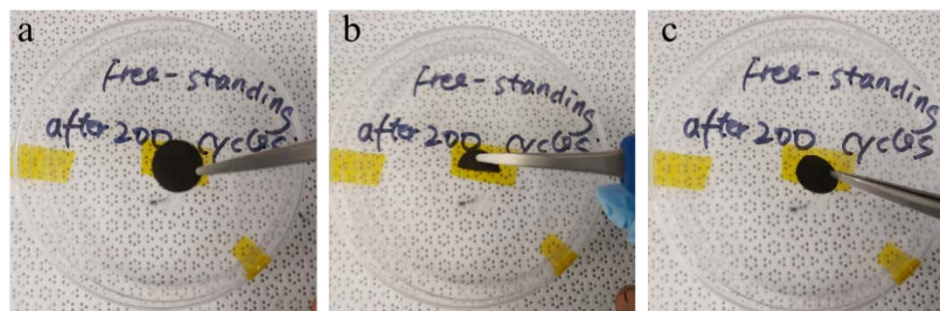


**Figure 3. 11** Photographs of the free-standing Sn@CFC electrode after 200 cycles.

The XRD pattern of the Sn@CFC electrode over 200 cycles has been provided in **Figure 3.12**. The phases of metallic Sn and alloying  $\text{Na}_{15}\text{Sn}_4$  are observed in the XRD pattern, indicating that the metallic Sn inside the carbon fiber is reversible during repeated sodiation/desodiation processes.

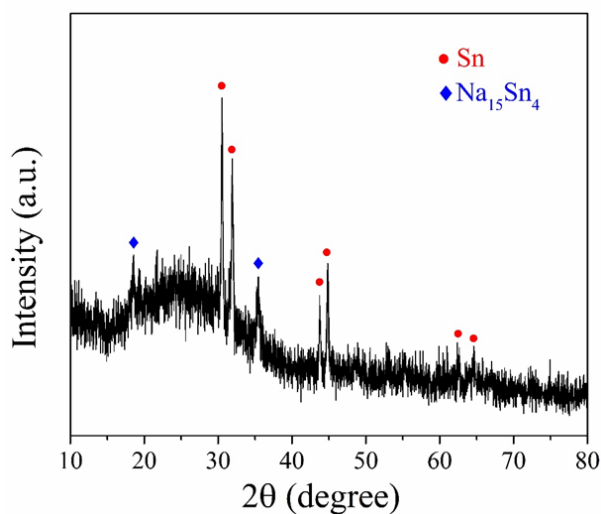


**Figure 3. 12** XRD of Sn@CFC after 200 cycles (charge to 1.0 V).

Moreover, the SEM images from **Figure 3.13** reveal that the structure of the Sn@CFC electrode remains almost the same compared with the images before cycle, demonstrating outstanding structure stability. Meanwhile, despite the expansion of the Sn after alloying

with sodium, there are no obvious crashing Sn particles in the electrode, indicating that the carbon as the buffer layer can significantly alleviate the strain driving from the volume change and prevent the pulverization of the Sn nanoparticles. Moreover, a thin and smooth SEI layer, which can protect the Sn particles to contact with the electrolyte, is found on the surface of the Sn@CFC electrode.

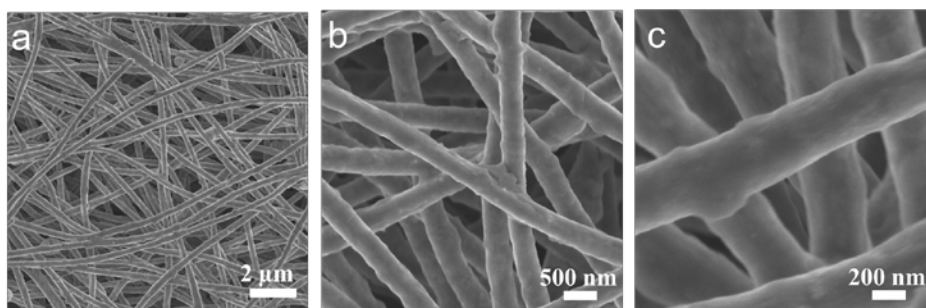


**Figure 3. 13** SEM images of the Sn@CFC electrode after 200 cycles.

Electrochemical kinetic properties of the Sn@CFC electrode were further studied by testing CV at various scan rates from 0.1 to 1  $\text{mV s}^{-1}$  to clarify the contributions from capacitive and diffusion-controlled behaviors. Capacitive-controlled behavior is also known as pseudocapacitance, which is defined as a faradaic charge transfer on the surface or near-surface region, exhibiting capacitor-like properties to achieve ultrafast charge storage. Pseudocapacitance can emerge when a battery material is engineered at the nanoscale with a large fraction of  $\text{Na}^+$  storage sites. **Figure 3.14 a** shows the CV curves at different scan rates. The CV curves display a similar shape while the peaks grow gradually with the increase of the scan rate. The relationship between the peak current ( $i$ ) and the sweep rate ( $v$ ) could be described by the power law as shown in **equation (3-3)**, where  $a$  and  $b$  are adjustable values [116, 117].

$$i = av^b \quad (3-3)$$

When the b value is 0.5, it indicates the diffusion-controlled behavior, while the surface-controlled capacitive reaction dominates for the value of 1. As shown in **Figure 3.14 b**, the b values of the cathodic peak and anodic peak are 0.68 and 0.78, respectively, according to the calculation by the slope of  $\log(i)$  versus  $\log(v)$  plots. The b values of both cathodic peak and anodic peak are between 0.5 and 1, indicating both diffusion-controlled behavior and capacitive reaction play important roles in contributing capacity. The ratio of the capacitive contribution is expressed by the **equation (3-4)**, in which  $k_1v$  is the capacitive contribution and  $k_2v^{1/2}$  is the contribution from diffusion-controlled processes ( $k_1$  and  $k_2$  are variable constants) [118, 119].

$$i = k_1v + k_2v^{1/2} \quad (3-4)$$

$$i(V)/v^{1/2} = k_1v^{1/2} + k_2 \quad (3-5)$$

If both sides of equation (5) are divided by  $v^{1/2}$  then it becomes **equation (3-5)**. By plotting the  $v^{1/2}$  versus  $i/v^{1/2}$  at different scan rates at a fixed voltage, the specific value of  $k_1$  and  $k_2$  were determined from the slope. **Figure 3.14 c** shows the CV curve and the capacitive contribution (shade area) at  $0.5 \text{ mV s}^{-1}$ , suggesting that the ratio of capacitive contribution is 87.1%. In the **Figure 3.14 d**, the ratio capacitive contribution displays a rising trend with the increase of scan rate, from 60.7% at  $0.1 \text{ mV s}^{-1}$  up to 87.1% at  $0.5 \text{ mV s}^{-1}$ , indicating that the capacitive contribution plays an important role at high rate of the Sn@CFC electrode. Therefore, the Sn@CFC electrode shows a good rate performance and delivers a high area capacity at a high current density.

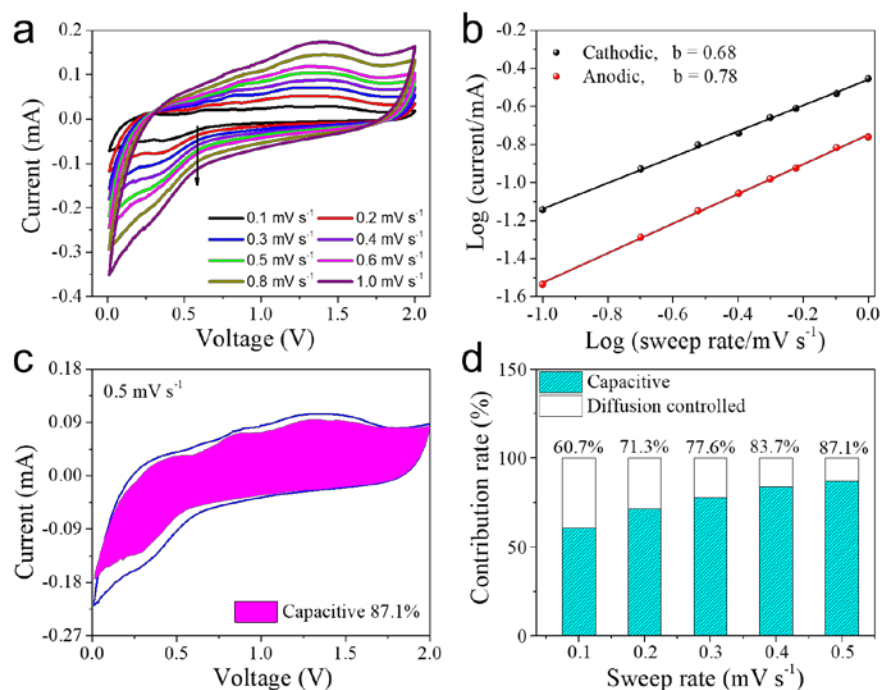


**Figure 3. 14** The electrochemical kinetic properties of the Sn@CFC anode. (a) CV curves at various scan rate from 0.1 mV s<sup>-1</sup> to 1 mV s<sup>-1</sup>. (b) The corresponding curves log  $i$  versus log  $v$  for the cathodic and anodic peak. (c) CV curve and the capacitive contribution (shaded area) at 0.5 mV s<sup>-1</sup>. (d) The capacitive contribution in percentage at different scan rates.

### 3.1.4 Conclusions of the Sn@CFC project

In summary, we performed a facile and scalable electrospinning method for a high-mass-loading free-standing Sn-based anode that metallic Sn nanoparticles are embedded in CF. The Sn@CFC electrodes deliver an ultra-long cycling life with high areal capacity and an improved rate capability due to the successful synergic effect of ultrasmall Sn nanoparticles and the N-doping 3D CF, which (1) the Sn nanoparticles significantly shorten the pathway of sodium ions and electrons; (2) the 3D crosslink CF act as buffer layer to mitigate the volume expansion and enhance the electronic conductivity. In

addition, the kinetic analyses indicate that the capacitive reactions play an important role in contributing capacity, leading to a good rate performance and delivers a high area capacity at a high current density. This work not only provides a highly simple and scalable method to fabricate an anode material with high areal capacity and high energy density but also sheds lights for effective design and development of advanced anodes for SIBs in further practical applications.

### **3.2 The SnP<sub>2</sub>O<sub>7</sub>@C anode with high pseudocapacitance<sup>3</sup>**

#### **3.2.1 Introduction**

Anode materials based on the conversion reactions or alloying process are attractive due to the high theoretical capacity and appropriate operating potential. To further improve the capacity, recent advances have developed electrode materials taking the advantage of both conversion and alloying reactions, featured as the mixed-reaction anodes such as Sb<sub>2</sub>S<sub>3</sub> and SnO<sub>2</sub> [120-124]. However, mixed-reaction anodes have large volume changes upon cycling, resulting in the electrode materials pulverization and severe degradation of the performance [125, 126]. To address this issue, many strategies have been proposed including structure engineering, robust material coating, novel binder addition, and using new types of electrolytes [39, 40, 127-132]. Nanocrystallization is widely considered as one of the most promising ways to mitigate the volume expansion of the mixed-reaction type anodes, since it can alleviate stress originating from the large volume changes and

---

<sup>3</sup> This section in full is a reprint of the paper “Achieving High Pseudocapacitance Anode by An In Situ Nanocrystallization Strategy for Ultrastable Sodium-Ion Batteries.” as it appears in ACS Appl. Mater. Interfaces 2021, 13, 19, 22577–22585, Wei He was the primary investigator and first author of this paper.

shorten the path for the ions and electrons, resulting in good cycling stability and rate performance [133]. In addition, the nanomaterials can boost the pseudocapacitance due to the large fraction of the  $\text{Na}^+$  storage sites to achieve ultrafast charging capability [134, 135]. Despite the improved electrochemical properties, the practical application of developing nanomaterials is still full of challenges owing to the complicated preparation process and the high cost. Moreover, nanoparticles are likely to aggregate upon cycling, resulting in inferior cycling stability. Thus, it is necessary to develop new methods to synthesize high-performance mixed-reaction type anode materials with ultrasmall particle size and a stable structure by a facile method to inhibit the aggregation and improve ionic/electronic conductivities.

In this project, a mixed-reaction type anode of  $\text{SnP}_2\text{O}_7$  was successfully synthesized and further dispersed in the robust N-doped carbon matrix to form a pomegranate-like  $\text{SnP}_2\text{O}_7@\text{C}$  sample by a scalable and economic method. Rather than restraining the pulverization of the  $\text{SnP}_2\text{O}_7$  particles, here, for the first time, we make use of the *in-situ* self-nanocrystallization process to generate ultrafine  $\text{SnP}_2\text{O}_7$  particles, leading to the success of addressing volume expansion upon cycling. A pomegranate-like structure is formed successfully with the homogeneous dispersion of those ultrafine particles in a robust carbon matrix and without particle aggregation upon cycling. The obtained self-nanocrystallization particles can improve the transport of ions and electrons to promote the electrochemical reaction while the N-doped carbon not only dramatically enhances the conductivity but also forms a strong interaction with  $\text{SnP}_2\text{O}_7$  to keep the self-nanocrystallization particles active during long-life cycles [132, 136, 137].

### 3.2.2 Material characterizations of SnP<sub>2</sub>O<sub>7</sub>@C

The SnP<sub>2</sub>O<sub>7</sub> nanoparticles were prepared directly through a hydrothermal method and was calcined in air, without the further carbon coating process. **Figure 3.15** shows the FESEM and TEM images of the SnP<sub>2</sub>O<sub>7</sub> particles, respectively, revealing that the size of as-prepared SnP<sub>2</sub>O<sub>7</sub> particles are just tens of nanometers.

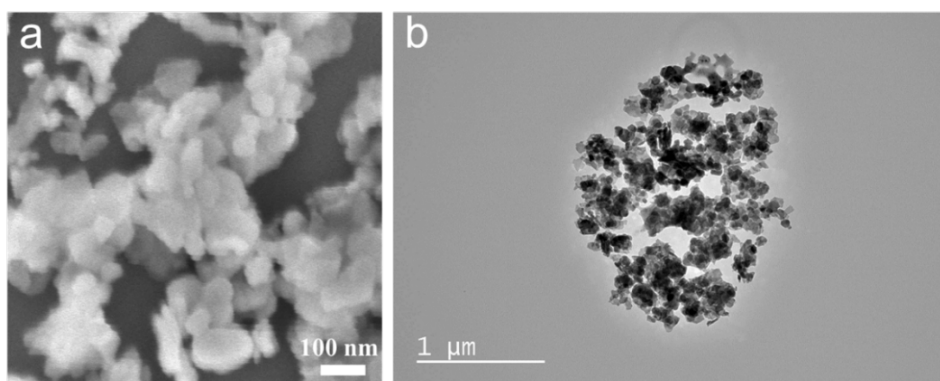


**Figure 3. 15** The FESEM image (a) and TEM image (b) of SnP<sub>2</sub>O<sub>7</sub>.

The microstructure and composition of SnP<sub>2</sub>O<sub>7</sub>@C are displayed in **Figures 3.16**. **Figures 3.16 a-d** show the SEM images of the SnP<sub>2</sub>O<sub>7</sub>@C particles. As shown in **Figure 3.16 a** and **Figure 3.16 b**, the SnP<sub>2</sub>O<sub>7</sub>@C particle shows a pomegranate-like structure with a size of about 1–5 μm. **Figure 3.16 c** and **Figure 3.16 d** show typical SEM images of SnP<sub>2</sub>O<sub>7</sub>@C in which there are many tiny primary particles of SnP<sub>2</sub>O<sub>7</sub> dispersed homogeneously in the robust carbon matrix. TEM is used to further investigate the microstructure of the SnP<sub>2</sub>O<sub>7</sub>@C material. **Figure 3.16 e** and **Figure 3.16 f** reveal that the SnP<sub>2</sub>O<sub>7</sub> nanoparticles are evenly distributed in the carbon matrix, which is consistent with the result of SEM. In **Figure 3.16 g**, the nanocrystal-SnP<sub>2</sub>O<sub>7</sub> is wrapped in the

amorphous carbon layer. As shown in **Figure 3.16 h**, the well-ordered lattice fringes with a distance of 0.399 nm agree well with the (200) plane of the cubic  $\text{SnP}_2\text{O}_7$ .

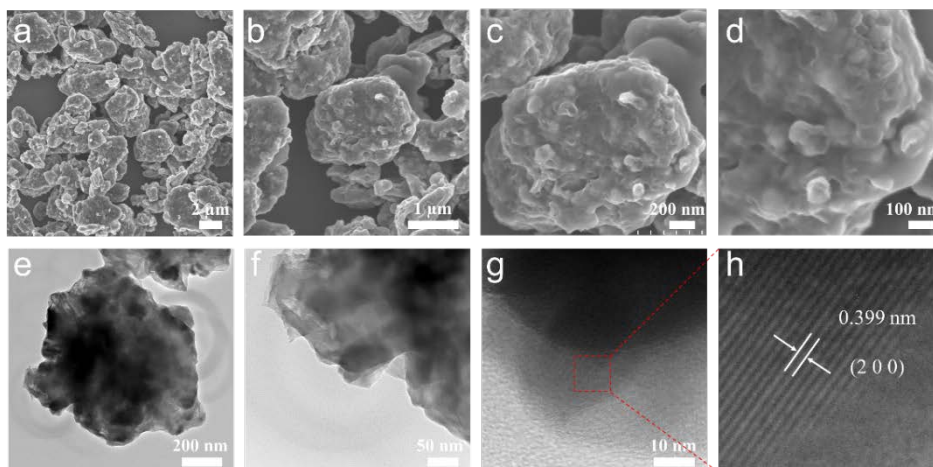


**Figure 3. 16** The morphologies and microstructures of  $\text{SnP}_2\text{O}_7@\text{C}$ , (a–d) FESEM images, and (e–h) TEM images.

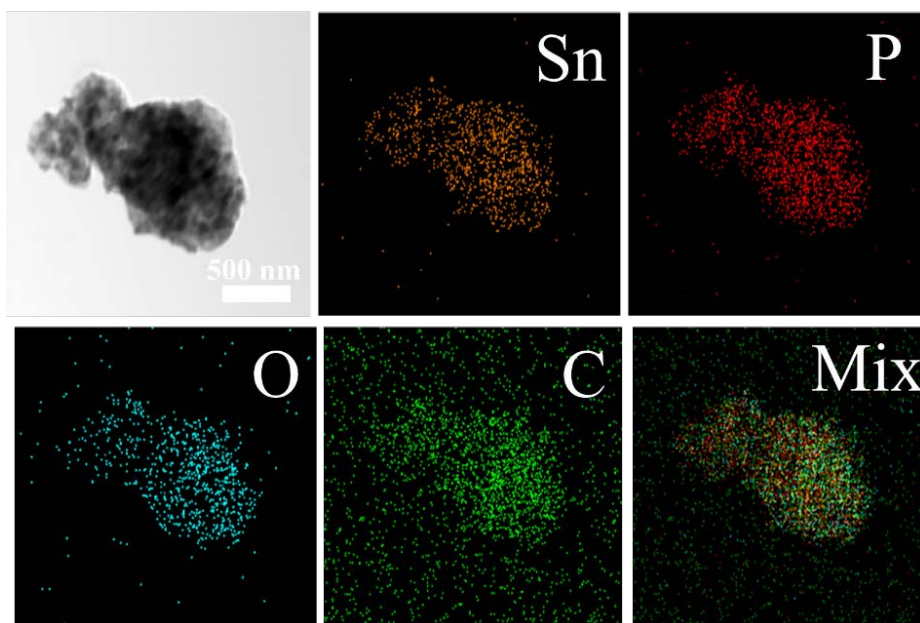


**Figure 3. 17** STEM image with the EDS elemental mappings.



The EDS elemental mapping of SnP<sub>2</sub>O<sub>7</sub>@C is shown in **Figure 3.17**. It can be confirmed that the elements of Sn, P, O, and C are evenly distributed, and no visible impurities are detected, demonstrating that the SnP<sub>2</sub>O<sub>7</sub> particles are homogeneously encapsulated in the carbon matrix.

The XRD measurement was carried out to study the crystal structure of as-prepared materials. **Figure 3.18 a** shows that the precursor phase of black hydrothermal product is Sn(HPO<sub>4</sub>)<sub>2</sub>·2H<sub>2</sub>O (JCPDS no. 31-1397). The XRD pattern for SnP<sub>2</sub>O<sub>7</sub>@C in **Figure 3.18 b** shows that all the intense and instinct peaks can be ascribed to a cubic phase of SnP<sub>2</sub>O<sub>7</sub> (JCPDS no. 29-1352). A broad peak between 20° to 30° in the XRD pattern is assigned to the amorphous carbon. The XRD pattern clearly demonstrates that the compound is made up of crystal SnP<sub>2</sub>O<sub>7</sub> and amorphous carbon.

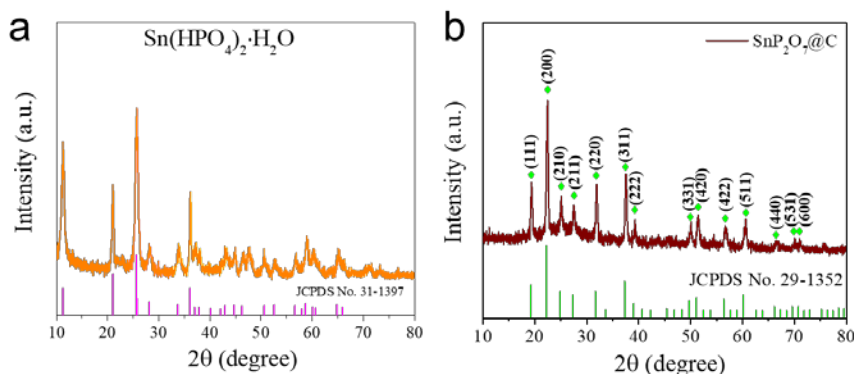


**Figure 3. 18** The XRD pattern of (a) Sn(HPO<sub>4</sub>)<sub>2</sub>·H<sub>2</sub>O and (b) SnP<sub>2</sub>O<sub>7</sub>@C.

In the FTIR spectroscopy profile (**Figure 3.19 a**), SnP<sub>2</sub>O<sub>7</sub> and SnP<sub>2</sub>O<sub>7</sub>@C show the main bands in the spectra from 1300 to 700 cm<sup>-1</sup>, fully consistent with the reported values for SnP<sub>2</sub>O<sub>7</sub> [138]. The characteristic IR peak at around 1150 cm<sup>-1</sup> was attributed to the asymmetric vibration mode  $\nu_s$  (PO<sub>3</sub>) of SnP<sub>2</sub>O<sub>7</sub>, and the bands at around 2980, 2350,

1550 and 1000  $\text{cm}^{-1}$  indicate the formation of amorphous carbon [139]. To gain insight into the amorphous carbon, the  $\text{SnP}_2\text{O}_7@\text{C}$  sample was evaluated through Raman spectroscopy. In **Figure 3.19 b**, two characteristic peaks are observed at 1364 and 1588  $\text{cm}^{-1}$  corresponding to D and G bands of carbon materials. The high intensity ratio of D band and G band ( $I_D/I_G = 1.46$ ) indicates many defects in the carbon matrix [140, 141], which can form strong interaction with the  $\text{SnP}_2\text{O}_7$  nanoparticles upon cycling [142, 143]. Hence, the carbon matrix can protect the particles against losing electrical contact with the current collector and enable a long-life cycle of the assembled cell. In addition, the highly disordered carbon matrix with abundant defects can significantly improve the surface redox reactions and provide more sodium ion adsorption sites.

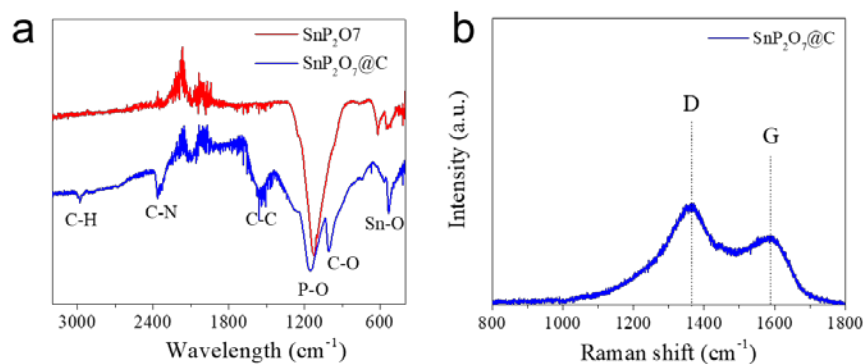


**Figure 3. 19** (a) The RTIR spectra of  $\text{SnP}_2\text{O}_7$  and  $\text{SnP}_2\text{O}_7@\text{C}$ , and (b) Raman spectra of  $\text{SnP}_2\text{O}_7@\text{C}$ .

TGA is conducted in air to investigate the content of  $\text{SnP}_2\text{O}_7$ .  $\text{SnP}_2\text{O}_7$  is very stable at high temperature because it is synthesized at 800  $^{\circ}\text{C}$  in the air. As shown in **Figure 3.20**, during the TGA test, the weight of  $\text{SnP}_2\text{O}_7$  is unchanged and the carbon matrix decomposes to  $\text{CO}_2$ , so the remainder is  $\text{SnP}_2\text{O}_7$ , and its weight content is 62.2%.

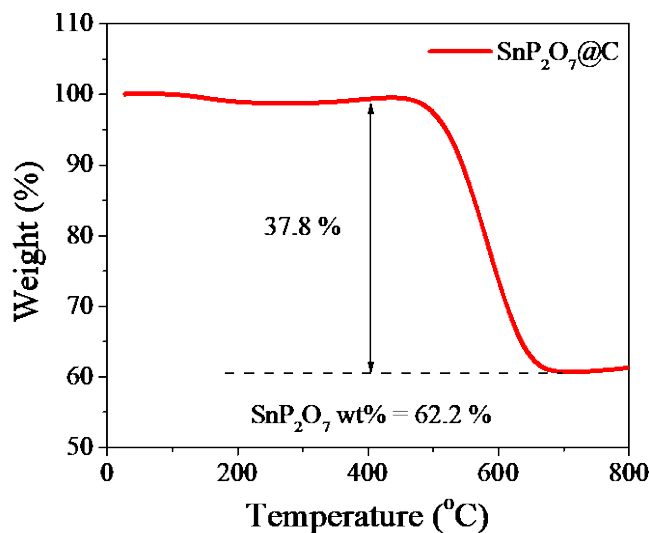


**Figure 3. 20** TGA profile of SnP<sub>2</sub>O<sub>7</sub>@C in air.

The chemical states of elements in SnP<sub>2</sub>O<sub>7</sub>@C are studied by XPS. The Sn, P, O, C and N elements are detected in the survey XPS spectrum of SnP<sub>2</sub>O<sub>7</sub>@C (**Figure 3.21 a**). In **Figure 3.21 b**, two dominate peaks at 496.1 and 487.8 eV in high-resolution Sn 3d spectrum correspond with Sn 3d<sub>3/2</sub> and Sn 3d<sub>5/2</sub> of Sn<sup>4+</sup>, respectively [144]. **Figure 3.21 c** shows one characteristic peak of P 2p at 134.1 eV. The high-resolution O 1s spectrum (**Figure 3.21 d**) can be fitted into two peaks, including a dominant peak at 532 eV assigned to the SnP<sub>2</sub>O<sub>7</sub> and another peak at 534 eV from O-C bonding [145]. The O-C bond suggests that the SnP<sub>2</sub>O<sub>7</sub> can form a strong interaction with the carbon matrix. In addition, according to the high-resolution C 1s spectrum (**Figure 3.21 e**), the peaks at 284.7, 285.9, 286.9 and 288.9 eV are related to the C=C/C-C, C=N, C-N and C=O, respectively [146, 147]. The high-resolution N 1s spectrum (**Figure 3.21 f**) shows three peaks of pyridinic N (398.6 eV), pyrrolic N (400.2 eV), and graphitic N (401.1 eV) [110]. The XPS results of C 1s and N 1s indicate the successful nitrogen doping in the carbon

matrix, which can enhance the conductivity of the composite SnP<sub>2</sub>O<sub>7</sub>@C anode [144, 147].

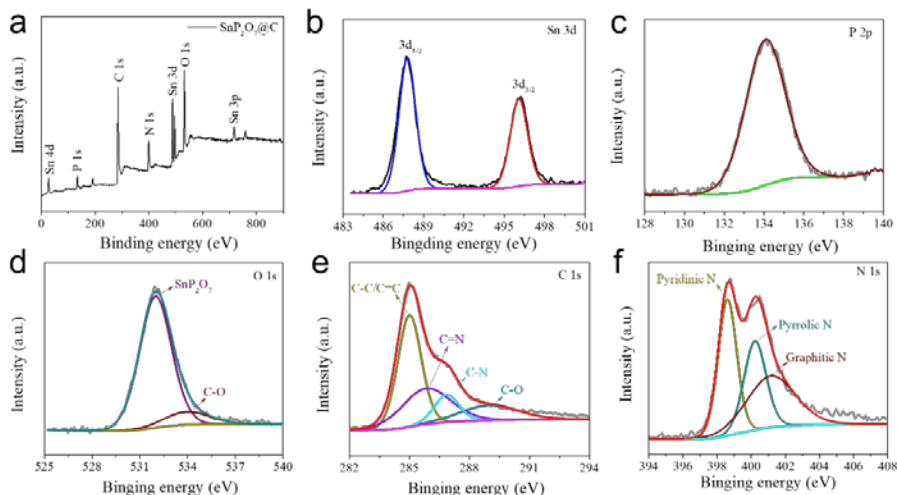
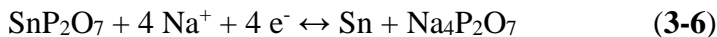


**Figure 3. 21** (a–f) XPS spectra of SnP<sub>2</sub>O<sub>7</sub>@C.

### 3.2.3 Electrochemical properties of SnP<sub>2</sub>O<sub>7</sub>@C

The CV curves are shown in **Figure 3.22**. For the SnP<sub>2</sub>O<sub>7</sub>@C electrode in **Figure 3.22 b**, a broad peak at around 1 V corresponds to the formation of SEI layer in the first cathodic sweep. A wide and sharp peak at around 0.4 V corresponds to the conversion reaction of SnP<sub>2</sub>O<sub>7</sub>, the formation of Na<sub>x</sub>Sn alloy, and the adsorption of sodium ions by carbon matrix [146, 148, 149]. This peak is more obvious than any other peaks. Another small cathodic peak below 0.2 V is observed, which is attributed to the alloying process of forming Na<sub>9</sub>Sn<sub>4</sub> [150]. In the anodic scan, a small broad anodic peak at 0.7 V is observed, corresponding to the dealloying process of Na<sub>x</sub>Sn [151]. The CV curves of the second cycle and third cycle overlap very well, demonstrating good reversibility and the stability of electrode. The sodiation/desodiation processes are described as follows:

Conversion reaction:



Alloying reaction:



The CV curves of  $\text{SnP}_2\text{O}_7$  are displayed in **Figure 3.22 a** with the same tested condition. It can be observed from the curves that the current of the  $\text{SnP}_2\text{O}_7$  anode is much smaller than that of  $\text{SnP}_2\text{O}_7@\text{C}$ . This difference derives from the addition of N-doped carbon that can absorb more sodium ions by the abundant defects.

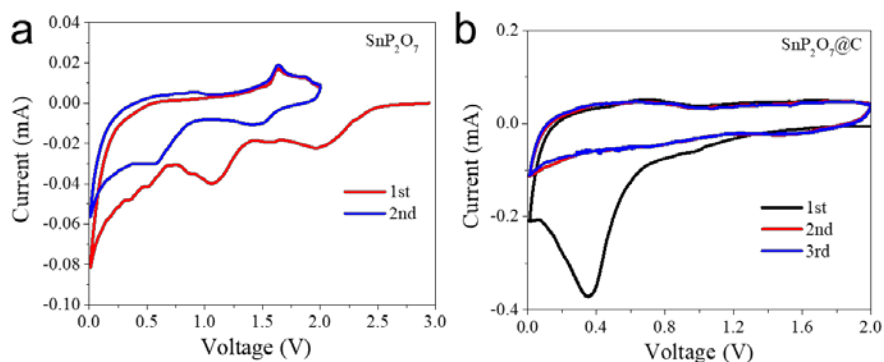


**Figure 3. 22** CV curves of the (a)  $\text{SnP}_2\text{O}_7$  and (b)  $\text{SnP}_2\text{O}_7@\text{C}$  electrodes at a scan rate of  $0.1 \text{ mV s}^{-1}$ .

HRTEM images in **Figure 3.23** shows that the  $\text{SnP}_2\text{O}_7$  phase can be formed again when the anode was charged to 2 V, demonstrating the good reversibility of the  $\text{SnP}_2\text{O}_7$  phase. The conversion reaction of  $\text{SnP}_2\text{O}_7$  and  $\text{Na}^+$  forms metallic Sn and  $\text{Na}_4\text{P}_2\text{O}_7$ , and the alloying reaction between Sn and  $\text{Na}^+$  can further release capacity, thus this mix-reaction mechanism can deliver high capacity.

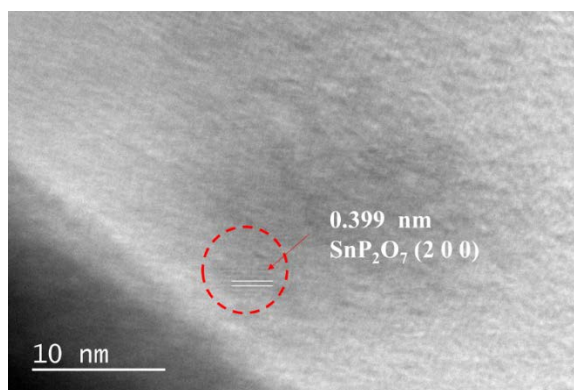


**Figure 3. 23** HRTEM image of SnP<sub>2</sub>O<sub>7</sub>@C after full charged to 2 V.

The charge/discharge curves of the SnP<sub>2</sub>O<sub>7</sub> and SnP<sub>2</sub>O<sub>7</sub>@C electrodes at 200 mA g<sup>-1</sup> are shown in **Figure 3.24**. The capacity of the SnP<sub>2</sub>O<sub>7</sub> anode decays fast from 596 mA h g<sup>-1</sup> to only 86 mA h g<sup>-1</sup> at the first cycle. This huge capacity fading is due to the particle pulverization of the SnP<sub>2</sub>O<sub>7</sub> particles caused by large volume changes. In contrast, the first discharge capacity of the novel SnP<sub>2</sub>O<sub>7</sub>@C electrode is 1140 mA h g<sup>-1</sup> and charge capacity is 403 mA h g<sup>-1</sup>. The relatively low CE is because of the formation of the SEI layer on the anode's surface and the trapping of sodium ions in the carbon matrix [152, 153]. The CE rises dramatically to over 99% in the fifth cycle.

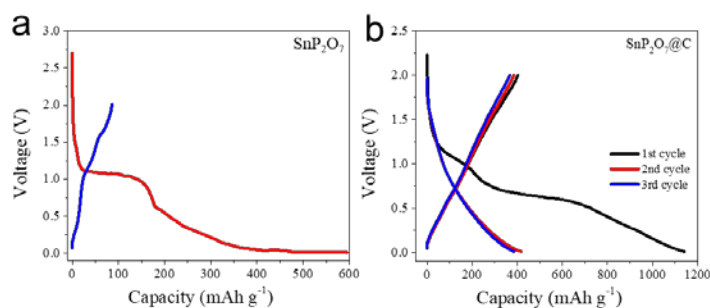


**Figure 3. 24** Discharge/charge profiles of the SnP<sub>2</sub>O<sub>7</sub> and SnP<sub>2</sub>O<sub>7</sub>@C electrodes at 200 mA g<sup>-1</sup>.

Moreover, the *ex-situ* XRD was conducted to investigate the phase evolution of the SnP<sub>2</sub>O<sub>7</sub>@C electrode during the first discharging and charging process (**Figure 3.25**). **Figure 3.25 b** reveals that the instinct peaks of the cubic SnP<sub>2</sub>O<sub>7</sub> phase gradually decrease until they fully disappear when the coin cell discharges from 2 to 0.01 V. However, after the cell charges back to 2 V, there is no peak assigned to cubic SnP<sub>2</sub>O<sub>7</sub> phase. This may be due to the ambiguous diffraction peaks due to the self-nanocrystallization of the SnP<sub>2</sub>O<sub>7</sub> particles to ultrasmall size, which has been reported on other conversion/alloying anodes [146, 154].

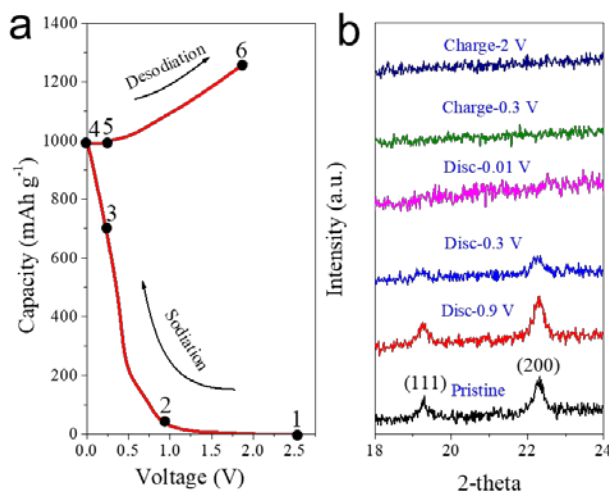


**Figure 3. 25** (a) Discharge/charge curves of SnP<sub>2</sub>O<sub>7</sub>@C. (b) *Ex-situ* XRD patterns of SnP<sub>2</sub>O<sub>7</sub>@C at selected discharge–charge states.

The cycling properties of the SnP<sub>2</sub>O<sub>7</sub>@C anode were tested at 200 mA g<sup>-1</sup> as shown in **Figure 3.26 a**. The SnP<sub>2</sub>O<sub>7</sub>@C anode delivers a capacity of 305 mA h g<sup>-1</sup> after 100 cycles, demonstrating excellent cycling stability. In contrast, the SnP<sub>2</sub>O<sub>7</sub> anode exhibits inferior cycling stability that the capacity decreases dramatically to below 100 mA h g<sup>-1</sup>

after just several cycles and down to only  $28 \text{ mA h g}^{-1}$  after 100 cycles. Apparently, the cycling stability of the  $\text{SnP}_2\text{O}_7$  material has a great improvement with the protection of the carbon layer. On the other hand, the CE of the  $\text{SnP}_2\text{O}_7@\text{C}$  electrode is stable and almost 100% throughout the whole process, while the CE of the  $\text{SnP}_2\text{O}_7$  anode is quite lower than that of  $\text{SnP}_2\text{O}_7@\text{C}$  with apparent fluctuation.

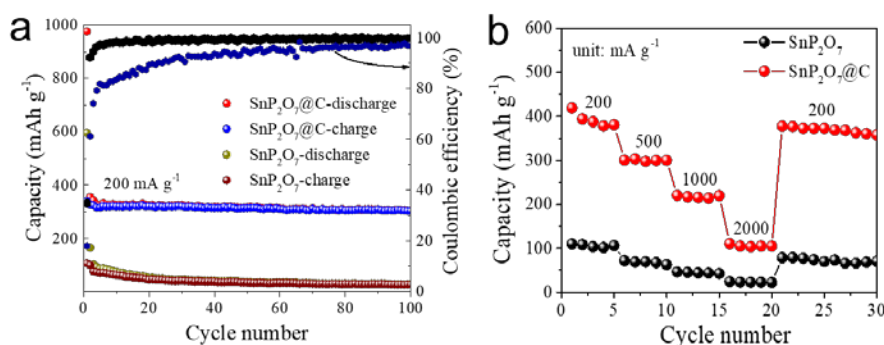


**Figure 3.26** (a) Cycling performance, and (b) Rate performance of the  $\text{SnP}_2\text{O}_7@\text{C}$  and  $\text{SnP}_2\text{O}_7$  electrodes.

**Figure 3.13b** displays the rate performances of  $\text{SnP}_2\text{O}_7@\text{C}$  at various current densities. The  $\text{SnP}_2\text{O}_7@\text{C}$  electrode displays high reversible capacities of 380, 300, 220 and 110  $\text{mA h g}^{-1}$  at a current density of 200, 500, 1000 and 2000  $\text{mA g}^{-1}$ , respectively. When the current density reverts back to 200  $\text{mA g}^{-1}$ , the capacity of the  $\text{SnP}_2\text{O}_7@\text{C}$  electrode can be fully recovered. In contrast, the  $\text{SnP}_2\text{O}_7$  electrode shows a clear contrast that the capacity drops to 100  $\text{mA h g}^{-1}$  at a low current density of 200  $\text{mA g}^{-1}$  and the cell fails to charge/discharge when the current density reaches 2000  $\text{mA g}^{-1}$ . The superior rate performance of the  $\text{SnP}_2\text{O}_7@\text{C}$  electrode can be attributed to the high conductivity of N-doped carbon with abundant defects and the short diffusion pathway of sodium ions driving from particle pulverization.



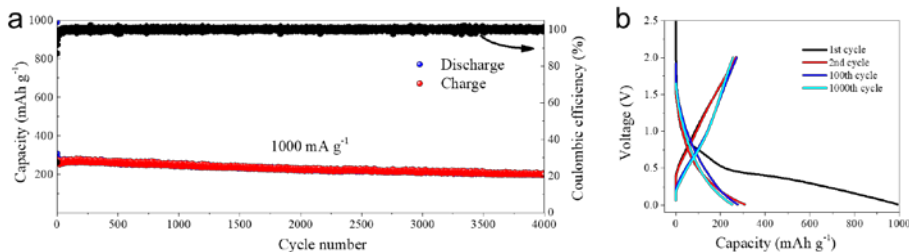


**Figure 3. 27** (a) Long-term cycling performance of SnP<sub>2</sub>O<sub>7</sub>@C at 1000 mA g<sup>-1</sup>, and (b) corresponding discharge/charge profiles.

**Figure 3.27 a** shows the long cycling performance of SnP<sub>2</sub>O<sub>7</sub>@C at 1000 mA g<sup>-1</sup>. It remains at a capacity of 185 mA h g<sup>-1</sup> after 4000 cycles without apparent capacity fluctuation throughout the whole cycling process. The capacity retention is 72 % and the capacity decay per cycle is only 0.007 %. Moreover, the 10th, 50th and 100th charge/discharge curves in **Figure 3.14b** almost overlap, indicating a stable and reversible electrochemical behavior of the SnP<sub>2</sub>O<sub>7</sub>@C electrode. The electrochemical performances of SnP<sub>2</sub>O<sub>7</sub>@C and previously reported mixed-reaction-type anode materials or their hybrid compound are compared and summarized in **Table 3.1**. According to this table, the SnP<sub>2</sub>O<sub>7</sub>@C anode displays one of the best performances among the mixed-reaction-type anodes for SIBs reported yet. The reasons come from the following aspects. First, the self-nanocrystallization ultrafine SnP<sub>2</sub>O<sub>7</sub> particles can significantly shorten the diffusion path of electrons and sodium ions, which allows for fast charge transport and good reaction kinetics.

**Table 3. 1** Performance of the common mix-reaction type anode materials for SIBs.

Materials	Voltage windows (V)	Current density [mA g <sup>-1</sup> ]	Cycle number	Reversible capacity [mAh g <sup>-1</sup> ]	Ref.
Sb <sub>2</sub> S <sub>3</sub> nanosheet	0.01-3	200	100	500	[155]
SbPO <sub>4</sub> /rGO	0.01-1.5	500	100	280	[156]
		1000	1000	100	
SnP <sub>3</sub> @C	0.01-2	150	150	805	[157]
SnO nanosheet	0.005-2.5	100	100	665	[158]
		1000	1000	492	
Sn <sub>4</sub> P <sub>3</sub> @C	0.01-3	200	300	413	[159]
		2000	4000	205	
Sn <sub>4</sub> P <sub>3</sub> @CNT/C	0.01-3	200	150	742	[160]
		2000	500	449	
SnS <sub>2</sub> @C	0.01-3	200	200	627	[161]
Sn/SnO <sub>x</sub> @MXene	0.01-3	50	200	594.2	[162]
SnS <sub>2</sub> Nanosheet	0.02-2.5	50	60	471	[126]
		200	80	417	
SnS@SNCF	0.01-2	100	100	600	[108]
		800	500	332	
SnS <sub>2</sub> /Sb <sub>2</sub> S <sub>3</sub> @rGO	0.01-2.8	200	100	642	[163]
		1000	400	480	
SnS@NC	0.01-3	500	100	443	[39]
SnP <sub>2</sub> O <sub>7</sub> @C	0.01-2	200	100	305	This
		1000	4000	185	work

Second, the N-doped carbon with abundant defects decreases the charge-transfer resistance, which is supported by the related Nyquist plots shown in **Figure 3.28**. Third, the carbon matrix can buffer the volume changes and form strong interaction with the  $\text{SnP}_2\text{O}_7$  nanoparticles, restraining the particle aggregation upon cycling.

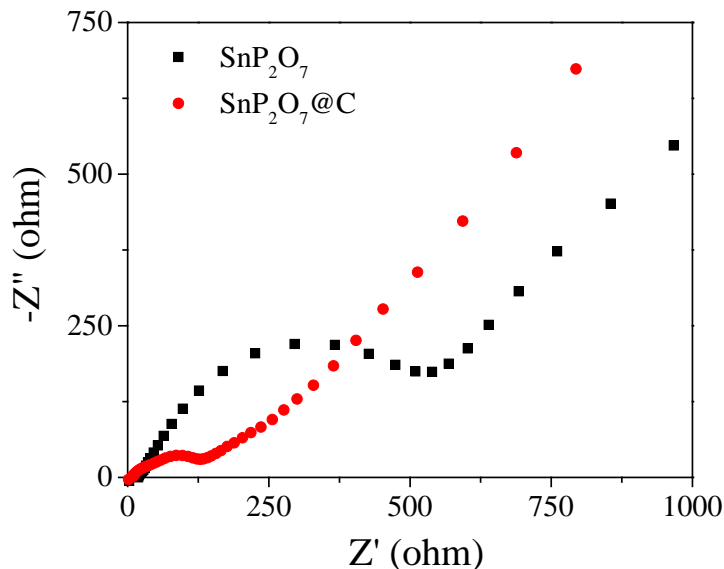


**Figure 3. 28** EIS spectra of the  $\text{SnP}_2\text{O}_7$ @C electrodes.

To further understand the self-nanocrystallization of the  $\text{SnP}_2\text{O}_7$  particles upon cycling, we performed the study on *ex-situ* TEM. The mechanism of structural revolution of the  $\text{SnP}_2\text{O}_7$  and  $\text{SnP}_2\text{O}_7$ @C electrodes is schematically illustrated in **Figure 3.29**. Without the protective layer, the  $\text{SnP}_2\text{O}_7$  particles experience immense volume changes and crush after several cycles inevitably, resulting in losing contact with the current collector and turning into permanently inactive components. Hence the pure  $\text{SnP}_2\text{O}_7$  electrode suffers poor cycling stability and an inferior rate capability as discussed above. However, with the protection of robust carbon matrix, the  $\text{SnP}_2\text{O}_7$  nanoparticles can form strong

adhesion with the carbon matrix even after particle pulverization, keeping the whole structure stable after ultralong cycle life.

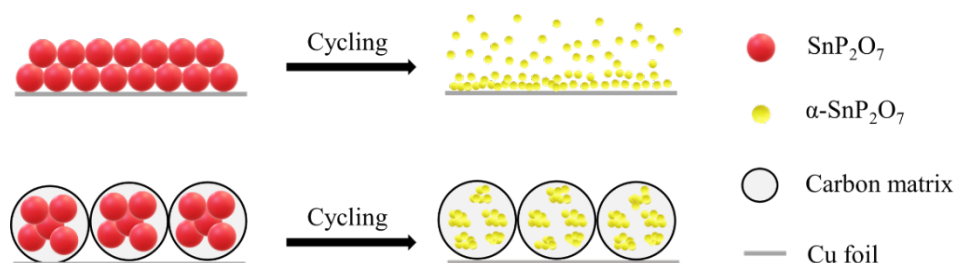


**Figure 3. 29** Schematic illustration for the cycling process of the  $\text{SnP}_2\text{O}_7@\text{C}$  and  $\text{SnP}_2\text{O}_7$  electrodes.

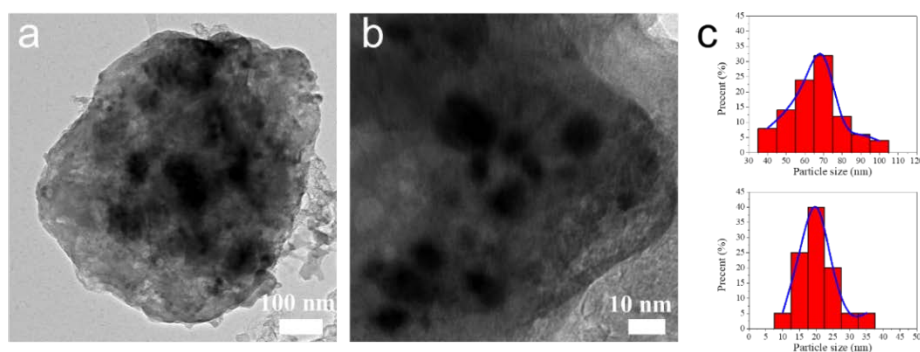


**Figure 3. 30** (a-b) TEM images of  $\text{SnP}_2\text{O}_7@\text{C}$  after 100 cycles at  $200 \text{ mA g}^{-1}$ . (c) The  $\text{SnP}_2\text{O}_7$  particle size distribution diagram of before cycle (upper) and after 100 cycles (lower).

The mechanism is further confirmed by the TEM images of the structure revolution of the  $\text{SnP}_2\text{O}_7@\text{C}$  electrode after 100 cycles. The TEM images in **Figures 3.30 a-b** reveal that the structure of  $\text{SnP}_2\text{O}_7@\text{C}$  is well preserved after long cycles and the  $\text{SnP}_2\text{O}_7$  particles inside are pulverized into smaller particles. The particle size distribution curves of the  $\text{SnP}_2\text{O}_7$  in the  $\text{SnP}_2\text{O}_7@\text{C}$  electrode are shown in **Figure 3.30 c**. The average size of the

SnP<sub>2</sub>O<sub>7</sub> particles after 100 cycles is 20.5 nm, which is much smaller than that of before cycling of 66 nm. The ultrasmall SnP<sub>2</sub>O<sub>7</sub> particles derived from particle pulverization can form strong adhesion with the carbon matrix, which further shortens the diffusion pathway of sodium ions and effectively alleviates strain originating from the volume changes, leading to longer cycling performance and better rate capability.

**Figure 3.31** shows the charge transfer resistance of SnP<sub>2</sub>O<sub>7</sub>@C before and after cycling by the EIS measurement. The resistance shows a slight decrease after 100 cycles, demonstrating the high structure stability and good conductivity of the SnP<sub>2</sub>O<sub>7</sub>@C anode.

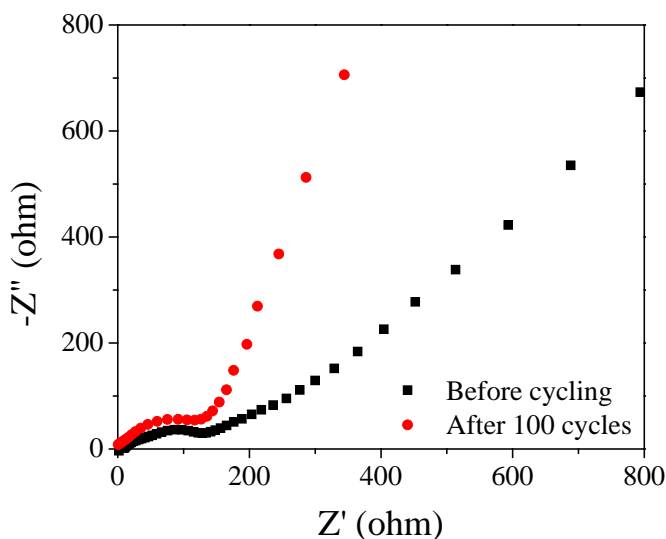


**Figure 3. 31** EIS spectra of the SnP<sub>2</sub>O<sub>7</sub>@C electrode before and after 100 cycles.

To understand the electrochemical kinetic properties, the CV curves of the SnP<sub>2</sub>O<sub>7</sub>@C electrode at various sweep rates are recorded in **Figure 3.32 a**. The b value of cathodic peak is calculated as 0.72 (**Figure 3.32 b**), suggesting that both diffusion- and capacitive-controlled behavior play important roles in contributing capacity. On the other hand, the b value of the anodic peak is 0.87, indicating the larger capacity contribution from the

capacitive-controlled behavior. As a comparison, the  $b$  values of the anodic and cathodic peaks of the pure  $\text{SnP}_2\text{O}_7$  electrode are 0.52 and 0.64 (**Figure 3.33**), thus the diffusion-controlled process dominates the sodium ions storage.

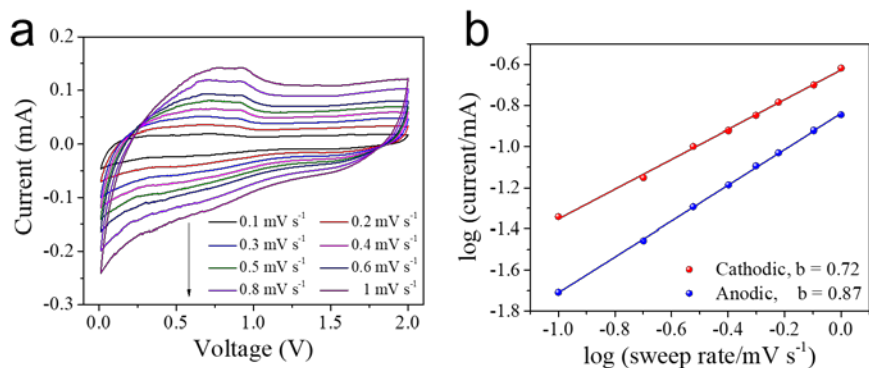


**Figure 3. 32** (a) CV curves of the  $\text{SnP}_2\text{O}_7@\text{C}$  electrode at various scan rate. (b)

Calculation of the  $b$  values based on the curves of  $\log i$  vs.  $\log v$ .

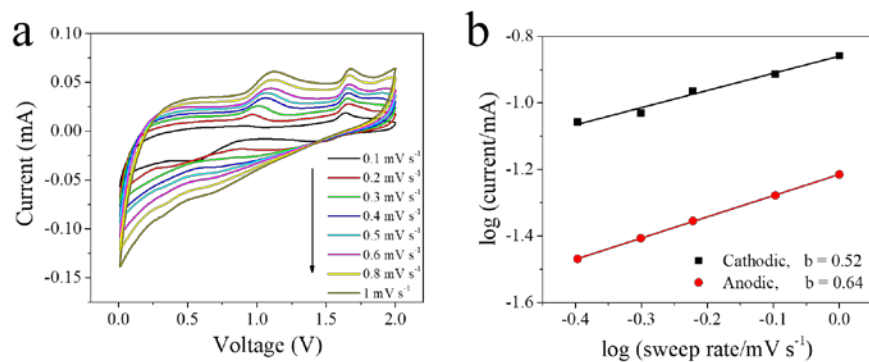


**Figure 3. 33** (a) CV curves of the  $\text{SnP}_2\text{O}_7$  electrode at various scan rate. (b) The corresponding curves of  $\log i$  versus  $\log v$  for cathodic and anodic peaks of the  $\text{SnP}_2\text{O}_7$  electrode.

**Figure 3.34 a** shows the capacitive-controlled behavior at  $0.4 \text{ mV s}^{-1}$ . The capacitive contribution is calculated at 75.7%, indicating that the capacitive energy storage is

predominant at this scan rate. It is also found that the SnP<sub>2</sub>O<sub>7</sub>@C electrode shows significant capacitive energy storage at different CV scan rates, rising from 51.8% at 0.1 mV s<sup>-1</sup> to 82.4% at 0.6 mV s<sup>-1</sup> as shown in **Figure 3.34 b**. The high capacitive energy storage can be contributed to the unique hierarchical structure with the nanoparticles wrapped in N-doped carbon matrix, which has been demonstrated by the morphology of SEM and TEM images and the results of Raman spectra. Since the enhanced capacitive contribution avoids slow sodium ion diffusion and prevents structure damage, the SnP<sub>2</sub>O<sub>7</sub>@C electrode has a good rate performance and an excellent cycling stability.

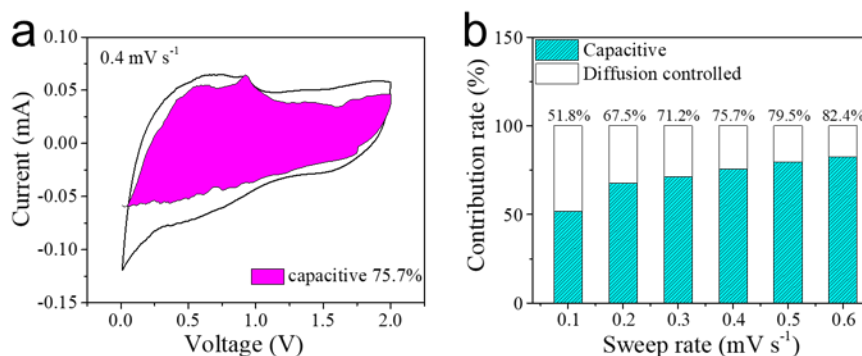


**Figure 3. 34** (a) Capacitive-controlled behavior at 0.4 mV s<sup>-1</sup>. (b) The capacitive contribution at different scan rates.

### 3.2.4 Conclusions of the SnP<sub>2</sub>O<sub>7</sub>@C project

A pomegranate-like SnP<sub>2</sub>O<sub>7</sub>@C material was successfully synthesized by a facile and scalable method. The self-nanocrystallized process was effectively utilized to generate ultrafine SnP<sub>2</sub>O<sub>7</sub> particles with homogeneous dispersion in the robust carbon matrix and without particle aggregation. Hence, the self-nanocrystallization SnP<sub>2</sub>O<sub>7</sub> particles fully make use of the advantage of nanomaterials that can shorten the diffusion path of

electrons and ions and alleviate strain originating from the sodiation/desodiation process. This nano engineering can boost pseudocapacitance to achieve high capacity and ultrafast charge storage. Moreover, the N-doped carbon matrix can enhance the conductivity of the material and keep the pulverization particles active during a long cycling life. The  $\text{SnP}_2\text{O}_7@\text{C}$  anode shows a high reversible capacity and exceptional cycle stability.

### **3.3 Heterostructure $\text{SnS}/\text{Sb}_2\text{S}_3@\text{SNC}$ anode with engineered porous structure<sup>4</sup>**

#### **3.3.1 Introduction**

The metallic sulfides can deliver high theoretical capacities since  $\text{Na}^+$  can be stored via the conversion reaction and/or the alloying reaction [164]. They also show a good reversibility upon cycling because of the weak M-S bonds [165]. For example, tin (II) sulfide ( $\text{SnS}$ ) with cubic phase and antimony sulfide ( $\text{Sb}_2\text{S}_3$ ) with an orthorhombic crystal structure are the two promising anodes for SIBs, which have large theoretical specific capacities of  $1022 \text{ mA h g}^{-1}$  and  $947 \text{ mA h g}^{-1}$ , respectively [166, 167]. In addition, when two metallic sulfides with different bandgaps combine together, heterostructures will be formed with internal electric fields, which have an enhanced charge-transfer capability [54, 55]. Despite the heterojunctions formed between metallic sulfides are able to improve the conversion-alloying reaction reversibility, they are still not good enough to remain the structure stable in a long cycling life or under a high current density [117, 168]. Thus, it is necessary to build a novel structure together with the heterostructure to

---

<sup>4</sup> This section in full has been submitted to Small Structures entitled “Realizing Rapid Kinetics of Na Ions in Tin-Antimony Bimetallic Sulfide Anode with Engineered Porous Structure”, Wei He was the primary investigator and first author of this paper.



mitigate the volume expansion of the metallic sulfides upon an extensive sodiation/desodiation process.

In this project, we come up with a ‘killing three birds with one stone’ method to build bimetallic sulfide of the SnS/Sb<sub>2</sub>S<sub>3</sub> heterostructure with engineered porous structure. The precursor of composite SnSb<sub>x</sub>/PAN/S was first obtained by ball milling SnSb<sub>x</sub>, PAN polymer, and sulfur together. During the following calcination process, the sulfur evaporated and reacted with SnSb<sub>x</sub> alloy to form the bimetallic SnS/Sb<sub>2</sub>S<sub>3</sub> heterostructure, and the original position of sulfur became void, generating the porous structure. Meanwhile, the PAN polymer was carbonized to form a highly disordered carbon matrix with sulfur and nitrogen co-doping. The advantages of this novel and facile process are in three folds. First, the SnS and Sb<sub>2</sub>S<sub>3</sub> with band gap difference form the heterostructures, which enhances the surface reaction kinetics and facilitates charge transport due to the internal electric field at heterointerface. Second, the porous structure provides space to mitigate the volume changes upon cycling. In addition, the S, N co-doped carbon matrix can boost the conductivity of the material, where abundant defects can provide fruitful sites to store sodium ions, leading to a high pseudocapacitance.

### **3.3.2 Material characterizations of SnS/Sb<sub>2</sub>S<sub>3</sub>@SNC**

The SEM images of the as-prepared SnS/Sb<sub>2</sub>S<sub>3</sub>@SNC particles are shown in **Figure 3.35**. As represented in **Figure 3.35 a, b**, the SnS/Sb<sub>2</sub>S<sub>3</sub>@SNC particles show an average particle size from hundreds of nanometers to a few microns. The high-resolution SEM images of the particles shown in **Figure 3.35 c, d** exhibit fruitful pores in the particles, which act as the void space to alleviate volume expansion of the SnS/Sb<sub>2</sub>S<sub>3</sub>

heterostructure. The SEM images of SnS/Sb<sub>2</sub>S<sub>3</sub> are also compared and shown in **Figure 3.36**.

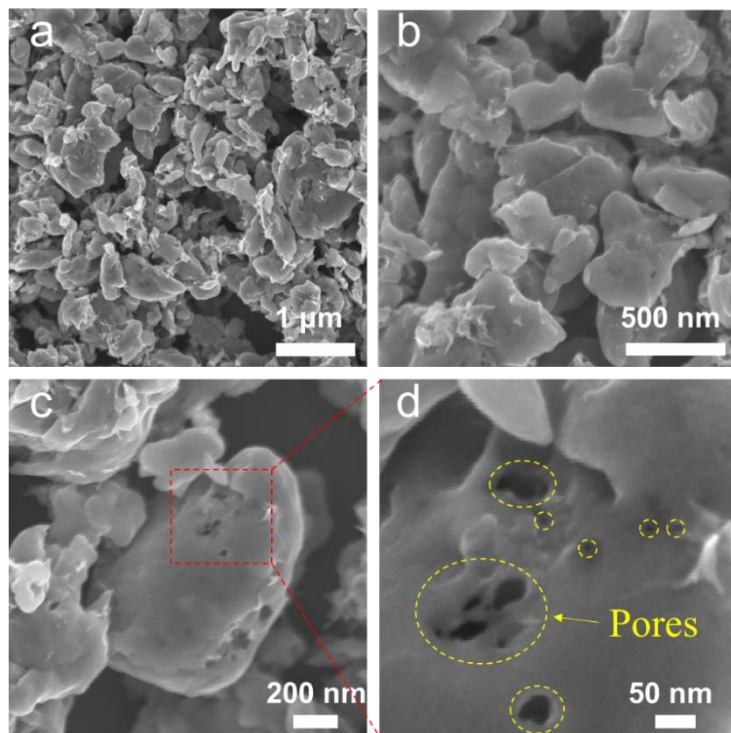


**Figure 3. 35** The SEM images of SnS/Sb<sub>2</sub>S<sub>3</sub>@C.

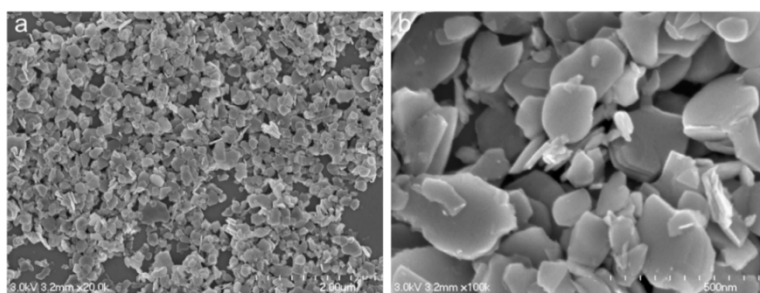


**Figure 3. 36** SEM images of the SnS/Sb<sub>2</sub>S<sub>3</sub> heterostructure.

To verify the distribution of the elements, the SnS/Sb<sub>2</sub>S<sub>3</sub>@SNC material was investigated by the EDS mapping (**Figure 3.37**). The results show that the elements of C, S, Sn, and

Sb are homogeneously distributed in the particles. The C element presents a similar distribution pattern compared to the other elements, indicating the SnS/Sb<sub>2</sub>S<sub>3</sub> composite is well coated with the carbon on its surface.

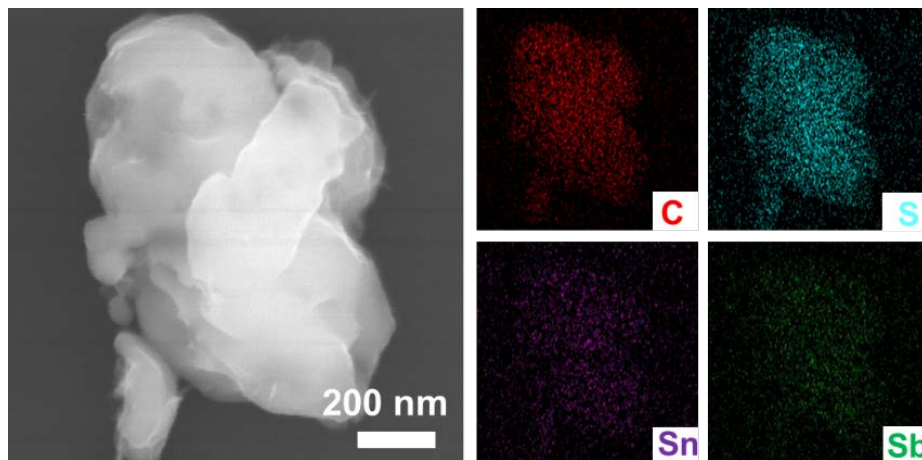


**Figure 3. 37** Selected SnS/Sb<sub>2</sub>S<sub>3</sub>@C particle for the EDS mapping, and the corresponding EDS elemental mappings.

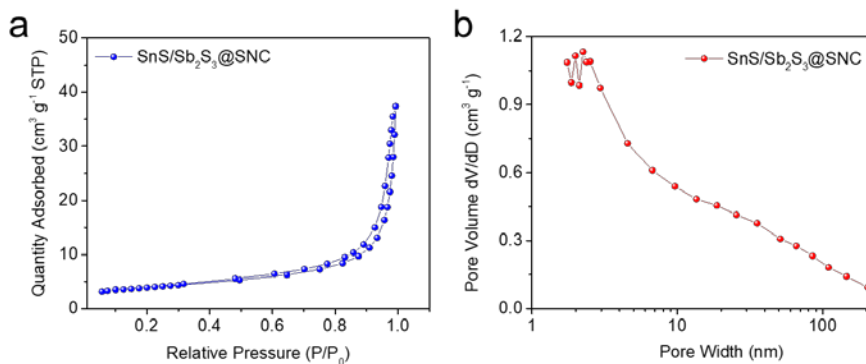


**Figure 3. 38** BET analysis of SnS/Sb<sub>2</sub>S<sub>3</sub>@SNC. (a) The nitrogen adsorption-desorption isotherm, and (b) the pore-size distribution curves.

The porous structure of the SnS/Sb<sub>2</sub>S<sub>3</sub>@SNC sample was further characterized by the BET test. The nitrogen adsorption-desorption isotherm is shown in **Figure 3.38 a**, and the

result fits the type III adsorption isotherm well [169]. Meanwhile, the pore-size distribution (**Figure 3.38 b**) reveals a hierarchical pore structure of the as-prepared material, which is consisting of the micro-, meso- and macropores. The formation of the hierarchical pore structure facilitates the infiltration of the electrolyte and provide void space to mitigate the large volume change of the electrode material upon cycling [170].

The XRD pattern in **Figure 3.39 a** shows that the intense and instinctive peaks of SnS/Sb<sub>2</sub>S<sub>3</sub>@SNC can be attributed to a cubic phase of SnS (JCPDS no. 43-0304), and some small peaks can be indexed to the orthorhombic phase of Sb<sub>2</sub>S<sub>3</sub> (JCPDS no. 42-1393). The amorphous feature of the as-prepared carbon matrix is further investigated by the Raman spectrum. In **Figure 4.8b**, two characteristic peaks located at 1334.7 and 1553.1 cm<sup>-1</sup> are D and G bands, respectively. The intensity ratio of the D band and G band ( $I_D/I_G$ ) is 1.49, demonstrating the dominant defective and disordered nature of the S, N co-doped carbon layer.

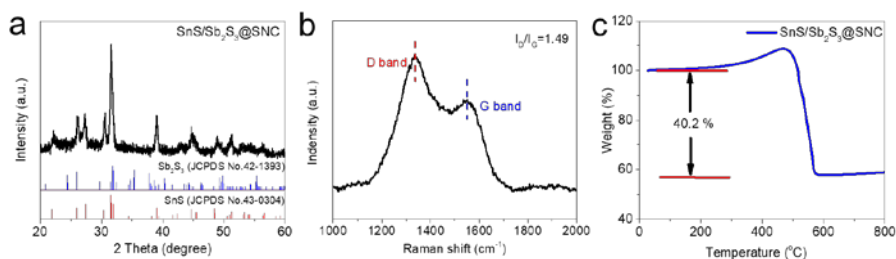


**Figure 3. 39** (a) XRD pattern, (b) Raman spectra, and (c) TGA curve of SnS/Sb<sub>2</sub>S<sub>3</sub>@C.

To confirm the carbon content in the SnS/Sb<sub>2</sub>S<sub>3</sub>@SNC material, TGA is conducted in the air with a temperature range from 25 to 800 °C (**Figure 3.39 c**). The slight weight increase at around 500 °C in the TGA curve can be ascribed to the oxidation of the

functional groups in the carbon matrix, which was also reported by other works [171]. According to the **equation (3-8) - (3-10)**, the weight ratios of carbon, SnS, and Sb<sub>2</sub>S<sub>3</sub> in composite are 37.6%, 44.2% and 18.2%, respectively.

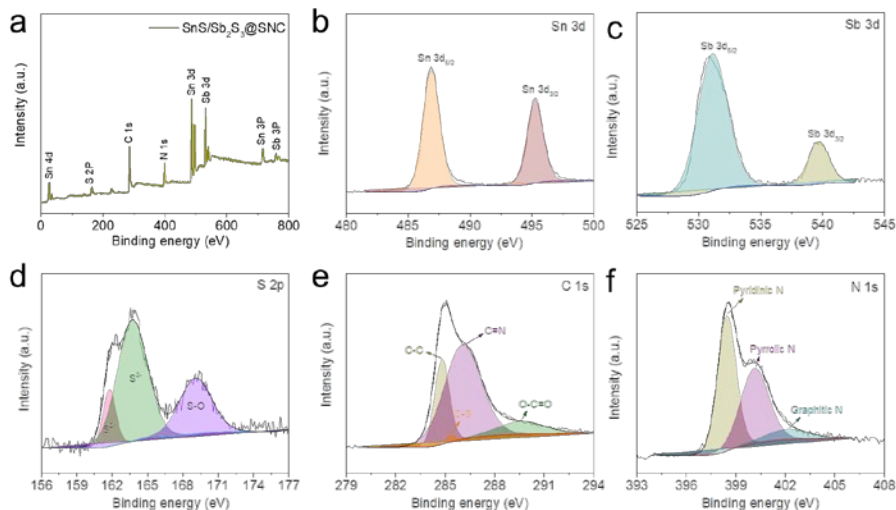
$$C \text{ wt. \%} = 1 - \frac{M(\text{SnS}) \times \text{Sn at. \%} + 0.5 \times M(\text{Sb}_2\text{S}_3) \times \text{Sb at. \%}}{M(\text{SnO}_2) \times \text{Sn at. \%} + 0.5 \times M(\text{Sb}_2\text{O}_3) \times \text{Sb at. \%}} \times (1 - \text{mass loss \%}) \quad (3-8)$$

$$\text{SnS wt. \%} = \frac{M(\text{SnS}) \times \text{Sn at. \%}}{M(\text{SnS}) \times \text{Sn at. \%} + 0.5 \times M(\text{Sb}_2\text{S}_3) \times \text{Sb at. \%}} \times (1 - C \text{ wt. \%}) \quad (3-9)$$

$$\text{Sb}_2\text{S}_3 \text{ wt. \%} = \frac{0.5 \times M(\text{Sb}_2\text{S}_3) \times \text{Sb at. \%}}{M(\text{SnS}) \times \text{Sn at. \%} + 0.5 \times M(\text{Sb}_2\text{S}_3) \times \text{Sb at. \%}} \times (1 - C \text{ wt. \%}) \quad (3-10)$$

The chemical bonding information of SnS/Sb<sub>2</sub>S<sub>3</sub>@SNC was analyzed by XPS. **Figure 3.40 a** shows the existence of the Sn, Sb, S, C, and N elements in the survey of the XPS spectrum. The high-resolution Sn 3d spectrum (**Figure 3.40 b**) displays a pair of characteristic peaks at 495.2 and 483.7 eV from Sn 3d<sub>3/2</sub> and Sn 3d<sub>5/2</sub> of Sn<sup>2+</sup>, respectively [172]. In **Figure 3.40 b**, the peaks for Sb 3d<sub>3/2</sub> (539.8 eV) and Sb 3d<sub>5/2</sub> (530.8 eV) confirm the existence of Sb<sup>3+</sup> [173]. The high-resolution S 2p spectrum can be fitted into three peaks as shown in **Figure 3.40 d**. The two peaks at 163.8 and 161.8 eV are assigned to the S 2p<sub>1/2</sub> and S 2p<sub>3/2</sub> orbitals of the divalent sulfide ions (S<sup>2-</sup>) [167]. Another peak with the binding energy of 169.1 eV corresponds to the S-O bond, indicating some of the surface S<sup>2-</sup> are oxidized during the XPS measurements [174]. In **Figure 3.40 e**, the high-resolution C 1s spectrum can be fitted to the peaks at 284.7, 285.3, 286.1, and 289.7 eV, which are related to the C-C, C-S, C-N, and C=O, respectively. The C=N and C-S peaks show that the carbon matrix is successfully doped by N and S atoms. Furthermore, three peaks can be observed in the high-resolution N 1s spectrum (**Figure 3.40 f**), and

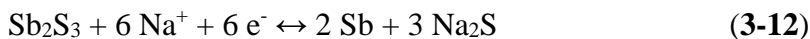
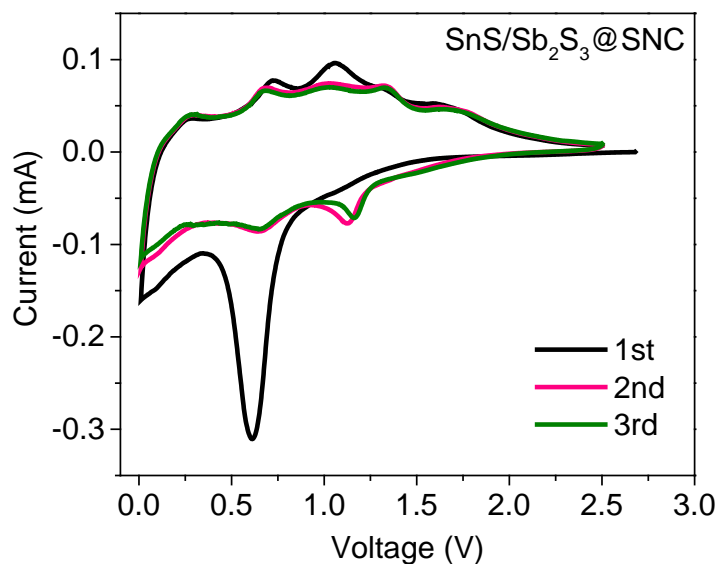
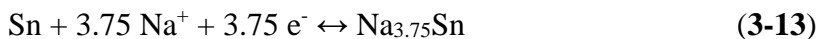
they correspond to pyridinic N (398.5 eV), pyrrolic N (400.2 eV), and graphitic N (401.8 eV). This phenomenon also confirms the successful N-doping in the carbon matrix.



**Figure 3.40** XPS spectra of SnS/Sb<sub>2</sub>S<sub>3</sub>@C, (a) survey, (b) Sn 3d, (c) Sb 3d, (d) S 2p, (e) C 1s, (f) N 1s.

### 3.3.3 Electrochemical performance of SnS/Sb<sub>2</sub>S<sub>3</sub>@SNC

**Figure 3.41** shows the CV curves of SnS/Sb<sub>2</sub>S<sub>3</sub>@SNC for the first three cycles, which were tested between 0.01 and 2.5 V at a scan rate of 0.1 mV s<sup>-1</sup>. In the first cathodic sweep, the sharp and broad peak at around 0.6 V corresponds to the conversion of SnS and Sb<sub>2</sub>S<sub>3</sub> to metallic Sn and Sb, the alloying process of Sn and Sb with Na<sup>+</sup>, and the formation of the SEI layer. After that, three small broad anodic peaks around 0.3 V, 0.7, and 1 V are observed, corresponding to the desodiation of the Na<sub>x</sub>Sn and Na<sub>x</sub>Sb phase. The CV curves of the second and third cycles are overlapped very well, demonstrating good reversibility and the stability of the electrode. The basic reversible reactions of SnS/Sb<sub>2</sub>S<sub>3</sub>@SNC can be described as follows:

**Conversion reactions:****Alloying/dealloying reactions:**

**Figure 3. 41** CV curves of SnS/Sb<sub>2</sub>S<sub>3</sub>@SNC at a scan rate of 0.1 mV s<sup>-1</sup>.

**Figure 3.42 a** displays the charge/discharge curves of the SnS/Sb<sub>2</sub>S<sub>3</sub>@SNC electrode at 200 mA g<sup>-1</sup>. The first discharge and charge capacities of SnS/Sb<sub>2</sub>S<sub>3</sub>@SNC are calculated as 995 and 456 mA h g<sup>-1</sup>, respectively. The charge/discharge curves of the SnSb<sub>x</sub> and SnS/Sb<sub>2</sub>S<sub>3</sub> electrodes are provided in **Figure 3.43**.

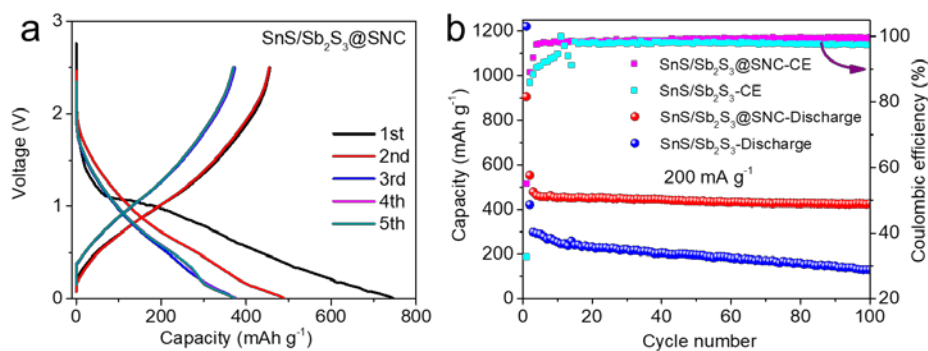


**Figure 3.42** (a) Galvanostatic discharge/charge profiles, and (b) Cycling performance of the SnS/Sb<sub>2</sub>S<sub>3</sub>@SNC electrode at 200 mA g<sup>-1</sup>.

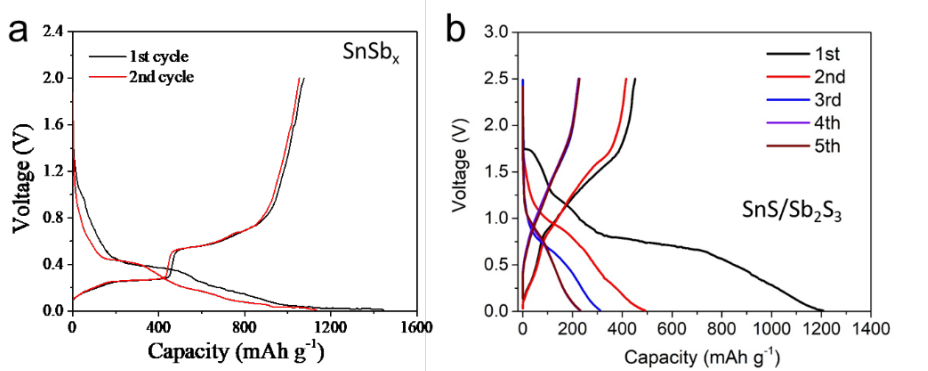


**Figure 3.43** The charge/discharge curves of the SnSb<sub>x</sub> and SnS/Sb<sub>2</sub>S<sub>3</sub> electrodes.

The cycling performance of the SnS/Sb<sub>2</sub>S<sub>3</sub>@SNC electrode was tested at 200 mA g<sup>-1</sup> and compared with that of the SnS/Sb<sub>2</sub>S<sub>3</sub> electrode as shown in **Figure 3.44**. The SnS/Sb<sub>2</sub>S<sub>3</sub> electrode shows poor cycling stability with a rapid performance degradation that the capacity decay to just 130 mA h g<sup>-1</sup> after 100 cycles. This is because the solid structure of the SnS/Sb<sub>2</sub>S<sub>3</sub> material cannot fully resist the stress derived from the large volume change upon cycling, resulting in the particle pulverization and turning into inactive components. In contrast, the SnS/Sb<sub>2</sub>S<sub>3</sub>@SNC electrode reveals much better cycling



stability than that of SnS/Sb<sub>2</sub>S<sub>3</sub>, delivering a capacity of 426 mA h g<sup>-1</sup> at 200 mA g<sup>-1</sup> after 100 cycles. The CE of the SnS/Sb<sub>2</sub>S<sub>3</sub>@SNC electrode rises quickly to over 98% after only 5 cycles and then remains a stable CE larger than 99% throughout the whole cycling process. On the other hand, the CE of the SnS/Sb<sub>2</sub>S<sub>3</sub> anode is quite lower than that of SnS/Sb<sub>2</sub>S<sub>3</sub>@SNC with apparent fluctuation.

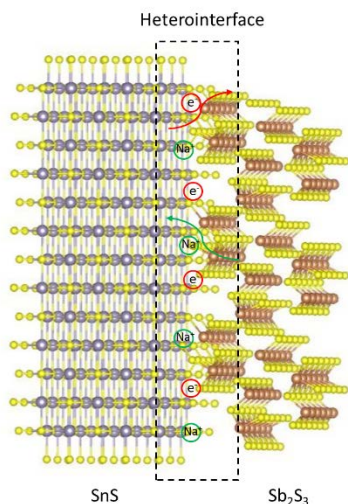


**Figure 3. 44** Schematic illustration of the micro-electric field at the SnS/Sb<sub>2</sub>S<sub>3</sub> heterointerfaces.

The good cycling performance of the SnS/Sb<sub>2</sub>S<sub>3</sub>@SNC electrode can be ascribed to the unique structure design. First, the porous structure can provide buffer space to alleviate large volume changes upon cycling. The structure also facilitates the electrolyte infiltration to boost the charge transfer. Second, the SnS/Sb<sub>2</sub>S<sub>3</sub> heterostructure can create a micro-electric field at heterointerfaces as illustrated in **Figure 3.44**, which can improve the ion-diffusion efficiency and promote interfacial electron transport. Third, the S, N co-doped carbon matrix with abundant defects can improve the conductivity of the composite material.

The synergistic effect of porous structure, SnS/Sb<sub>2</sub>S<sub>3</sub> heterostructure, and S, N co-doped carbon matrix is expected to significantly enhance ionic and electronic transport, which is further investigated by the EIS tests. As shown in **Figure 3.45 a**, the semicircle in the EIS spectra of the SnS/Sb<sub>2</sub>S<sub>3</sub>@SNC electrode, which represents the charge transfer resistance, is much smaller than that of SnS/Sb<sub>2</sub>S<sub>3</sub> before cycle. The SnS/Sb<sub>2</sub>S<sub>3</sub>@SNC electrode shows a smaller charge transfer resistance after 10 cycles compared with fresh cell (**Figure 3.45 b**).

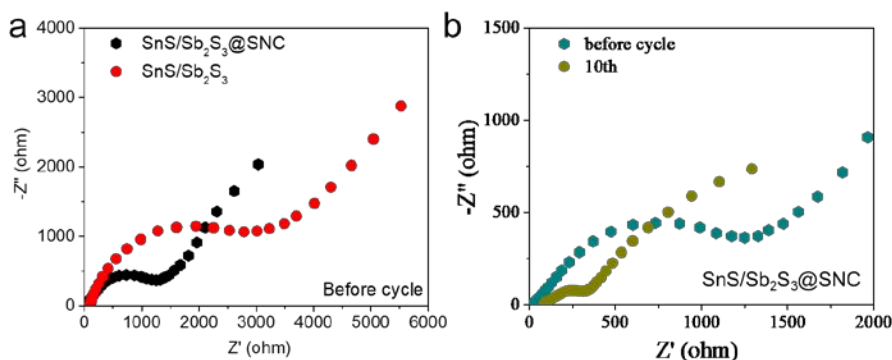


**Figure 3. 45** The Nyquist plots of the (a) SnS/Sb<sub>2</sub>S<sub>3</sub> and SnS/Sb<sub>2</sub>S<sub>3</sub>@SNC electrodes before cycle, and (b) the SnS/Sb<sub>2</sub>S<sub>3</sub>@SNC electrode before and after 10 cycles.

The improvement of the ionic and electronic conductivity benefits the rate performance of the SnS/Sb<sub>2</sub>S<sub>3</sub>@SNC electrode. As shown in **Figure 3.46 a**, the cells were tested at various current densities from 50 to 5000 mA g<sup>-1</sup>. The SnS/Sb<sub>2</sub>S<sub>3</sub>@SNC electrode delivers specific capacities of 457, 404, 357, 301, and 252 mA h g<sup>-1</sup> at the current densities of 50, 200, 500, 1000, and 2000 mA g<sup>-1</sup>, respectively. Even at a very high current density of 5000 mA g<sup>-1</sup>, the cell with the SnS/Sb<sub>2</sub>S<sub>3</sub>@SNC electrode can provide a capacity of 200 mA h g<sup>-1</sup>. When the current density dropped back to 50 mA g<sup>-1</sup> after various current densities, the capacity rebounded to 440 mA h g<sup>-1</sup>, indicating an excellent

rate performance and cycling stability of the SnS/Sb<sub>2</sub>S<sub>3</sub>@SNC electrode. The long-term cycling stability of the SnS/Sb<sub>2</sub>S<sub>3</sub>@SNC electrode was further examined at a high current density of 500 mA g<sup>-1</sup> (**Figure 3.46 b**). The SnS/Sb<sub>2</sub>S<sub>3</sub>@SNC electrode delivers a reversible capacity of 322 mA h g<sup>-1</sup> after 400 cycles, and the CE reaches more than 99% after the 5th cycle and remains stable throughout the whole cycling process.

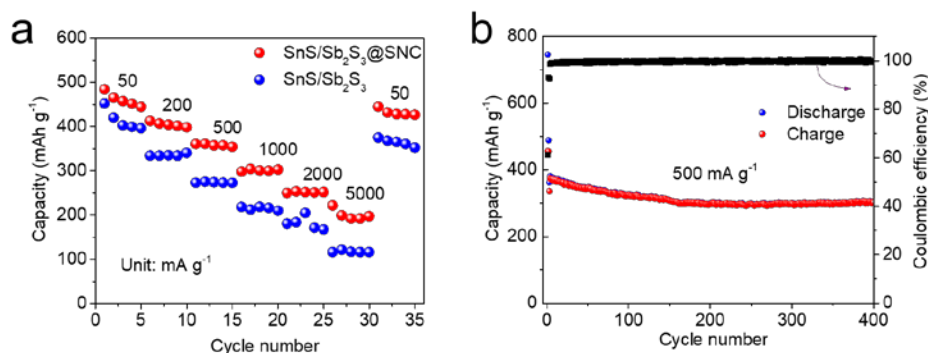


**Figure 3.46** (a) Rate performance of SnS/Sb<sub>2</sub>S<sub>3</sub>@SNC and SnS/Sb<sub>2</sub>S<sub>3</sub> at various rates (50–5000 mA g<sup>-1</sup>), and (b) Long-term cycling performance of the SnS/Sb<sub>2</sub>S<sub>3</sub>@SNC anode at 500 mA g<sup>-1</sup>.

The CV tests of the SnS/Sb<sub>2</sub>S<sub>3</sub>@SNC electrode at various scan rates from 0.1 to 1 mV s<sup>-1</sup> were performed to examine the electrochemical kinetic properties. The same peaks can be found in the CV curves at different scan rates as shown in **Figure 3.47 a**. The intensities of those peaks grow gradually with the increase of the scan rates. According to **Figure 3.47 b**, the b values of three cathodic peaks of the SnS/Sb<sub>2</sub>S<sub>3</sub>@SNC electrode are 0.839, 0.854, and 0.769. In addition, the b values of the anodic peaks are 0.841, 0.897, and 0.864, respectively. The capacity contribution from capacitive-controlled process is derived from the S, N co-doped carbon matrix, which can improve the surface redox kinetics of the SnS/Sb<sub>2</sub>S<sub>3</sub>@SNC electrode. At a high scan rate of CV at 0.8 mV s<sup>-1</sup>, the

capacitive contribution is 79.5% as shown in shade area (**Figure 3.47 c**). The high capacitive contribution reveals the predomination of pseudocapacitance at this scan rate, which benefits the fast-charging capability and high-power density of the assembled cell. The dominant pseudocapacitive contribution of the SnS/Sb<sub>2</sub>S<sub>3</sub>@SNC anode can be ascribed to the unique porous SnS/Sb<sub>2</sub>S<sub>3</sub> heterostructure and the S, N co-doped carbon matrix.

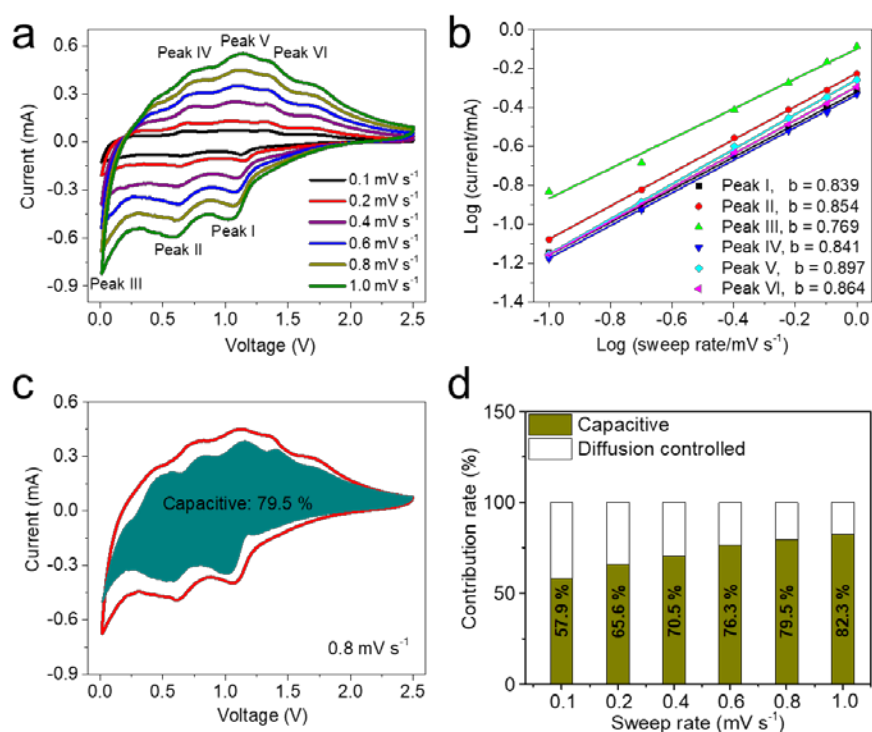


**Figure 3. 47** The electrochemical kinetic properties of SnS/Sb<sub>2</sub>S<sub>3</sub>@SNC. (a) CV curves at various scan rates from 0.1 to 1 mV s<sup>-1</sup>. (b) The corresponding curves log i versus log v for the cathodic and anodic peaks. (c) CV curve and the capacitive contribution (shaded area) at 0.8 mV s<sup>-1</sup>. (d) The capacitive contribution in percentage at different scan rates.

### 3.3.4 Conclusions of the SnS/Sb<sub>2</sub>S<sub>3</sub>@SNC project

In summary, a porous bimetallic sulfide SnS/Sb<sub>2</sub>S<sub>3</sub> heterostructure has been prepared and encapsulated in a S, N co-doped carbon matrix. The internal electric field at SnS/Sb<sub>2</sub>S<sub>3</sub> heterointerfaces can enhance charge transport and promote reaction kinetics. The S, N co-doping can greatly improve the conductivity of carbon matrix, which addresses the issue of sluggish kinetics of Na<sup>+</sup>. Meanwhile, the porous structure can provide void space to mitigate the volume expansion upon cycling, guaranteeing long-term cycling stability. The SnS/Sb<sub>2</sub>S<sub>3</sub>@SNC anode delivers high capacities of 425 mA h g<sup>-1</sup> at 200 mA g<sup>-1</sup> after 100 cycles, and 302 mA h g<sup>-1</sup> at 500 mA g<sup>-1</sup> after 400 cycles. The SnS/Sb<sub>2</sub>S<sub>3</sub>@SNC anode also demonstrates good rate capability, and it shows a capacity of over 200 mA h g<sup>-1</sup> at a high current density of 5000 mA g<sup>-1</sup>.

### 3.4 Conclusions

Three Sn-based anodes of Sn@CFC, SnP<sub>2</sub>O<sub>7</sub>@C and SnS/Sb<sub>2</sub>S<sub>3</sub>@SNC have been developed in SIBs. They all show improved electrochemical performance because of the unique structure design. The Sn@CFC material prepared by the electrospinning technology can be used as the electrode directly without binder and current collector, yielding high mass loading. The SnP<sub>2</sub>O<sub>7</sub>@C sample make use of the self-nanocrystallization to generate nanoparticles, which from strong adhesion to the robust carbon matrix and remain active in a long cycling life. The SnS/Sb<sub>2</sub>S<sub>3</sub>@SNC anode takes the advantages of the SnS/Sb<sub>2</sub>S<sub>3</sub> heterostructure and the engineered porous structure to mitigate the large volume expansion upon cycling, enabling fast charging capability. Those work shed now light on developing advanced anodes for SIBs.

## Chapter 4 Tetrahydrofuran electrolyte additive for highly reversible aqueous zinc-ion batteries<sup>5</sup>

### 4.1 Introduction

Cyclic ethers such as 1,3-dioxane and THF are widely used in various chemical fields as a solvent [175]. These cyclic ethers are miscible with H<sub>2</sub>O at any composition and their solvent properties such as dielectric constant and viscosity can be adjusted by changing the mixing ratio [176]. The cyclic ether molecule can play as a proton acceptor to form hydrogen bond between the oxygen atom of the cyclic ether molecule and proton of water molecule [177]. Here, for the first time, the THF additive was introduced into the 2 M ZnSO<sub>4</sub> electrolyte for AZIBs. THF as a proton acceptor can moderately disrupt the water network by forming hydrogen bonds to decrease the water activity, thus optimizing the solvation structure of the Zn hydration layer to suppress the decomposition of the water and the generation of the byproducts. The Zn metal electrode shows an improved electrochemical behavior in the 2 M ZnSO<sub>4</sub> electrolyte with a small amount of the THF (5% by volume) additive.

---

<sup>5</sup> Chapter 4 in full is a reprint of the paper “Decreasing Water Activity Using the Tetrahydrofuran Electrolyte Additive for Highly Reversible Aqueous Zinc Metal Batteries.” as it appears in ACS Appl. Mater. Interfaces 2023, 15, 5, 6647–6656, Wei He was the primary investigator and first author of this paper.

## 4.2 Results and analysis

### 4.2.1 DFT simulation and electrolyte characterization

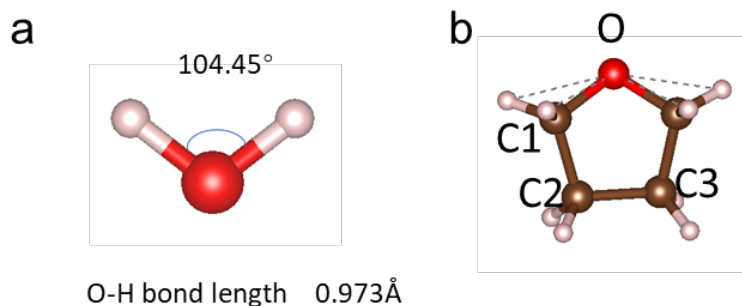


**Figure 4. 1** The molecular formula of (a) H<sub>2</sub>O and (b) THF molecules.

**Figure 4.1** shows the molecular formula of the H<sub>2</sub>O and THF molecules, where THF has one oxygen atom as a proton acceptor within the molecule. Thus, the oxygen atoms within THF can form hydrogen bonds with protons of the water molecules to decrease water activity.

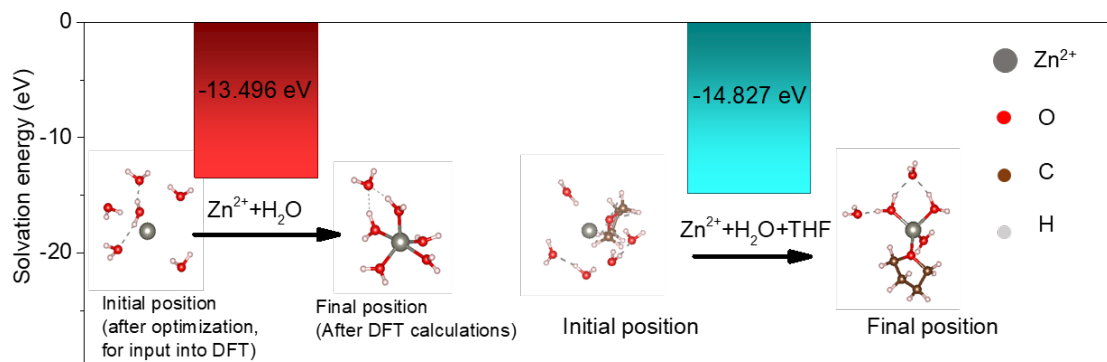


**Figure 4. 2** Optimized solvation structure and the corresponding solvation energy with the THF additive in the DFT calculations.

DFT simulations are performed to study the Zn<sup>2+</sup> solvation energy in the aqueous electrolytes. Zn<sup>2+</sup> is considered to mainly coordinate with 6 H<sub>2</sub>O molecules (Zn[H<sub>2</sub>O]<sub>6</sub><sup>2+</sup>)

in the low concentration  $\text{ZnSO}_4$  electrolyte based on the previous references [178, 179]. With the introduction of the THF additive, some THF molecules will replace water molecules in the main  $\text{Zn}[\text{H}_2\text{O}]_6^{2+}$  solvation structure due to the strong interaction between THF and  $\text{H}_2\text{O}$  by the hydrogen bonds. Many possible solvation configurations of  $\text{Zn}[\text{H}_2\text{O}]_x[\text{THF}]_y^{2+}$  emerge in the optimized 2 M  $\text{ZnSO}_4/\text{THF}$  5% electrolyte. Because the ratio of the water molecules and the THF molecules is larger than 5:1, the possible solvation structure is that one THF molecule replaces one water molecule in the  $\text{Zn}[\text{H}_2\text{O}]_6^{2+}$  solvation structure to form  $\text{Zn}[\text{H}_2\text{O}]_5[\text{THF}]^{2+}$ . Thus, the representative solvation structures of  $\text{Zn}^{2+}$  in two different electrolytes mentioned above are shown in **Figure 4.2**. First, the total energy ( $E_{total}$ ) values of  $\text{Zn}[\text{H}_2\text{O}]_6^{2+}$  and  $\text{Zn}[\text{H}_2\text{O}]_5[\text{THF}]^{2+}$  solvation structures are calculated.  $E_{\text{H}_2\text{O}}$  and  $E_{\text{THF}+\text{H}_2\text{O}}$  are calculated by removing the  $\text{Zn}^{2+}$  ion from the two solvation structures. Meanwhile, the energy of a single  $\text{Zn}^{2+}$  ion ( $E_{\text{Zn}^{2+}}$ ) is also calculated separately. Finally, the solvation energy ( $E_{sol}$ ) is calculated as the difference between  $E_{total}$ ,  $E_{\text{H}_2\text{O}/\text{THF}+\text{H}_2\text{O}}$  and  $E_{\text{Zn}^{2+}}$  (**Equation 2-1**). These results are summarized in **Figure 4.2** and **Table 4.1**. It is found that the solvation energy of  $\text{Zn}[\text{H}_2\text{O}]_6^{2+}$  is calculated to be -13.496 eV, which agrees with the values in the previous literature.[180] On the other hand, the solvation energy of  $\text{Zn}[\text{H}_2\text{O}]_5[\text{THF}]^{2+}$  is -14.827 eV, which is 1.331 eV lower than that of  $\text{Zn}[\text{H}_2\text{O}]_6^{2+}$ , indicating that  $\text{Zn}[\text{H}_2\text{O}]_5[\text{THF}]^{2+}$  is a more stable solvation structure. Although more bonds are formed between the  $\text{Zn}^{2+}$  ion and oxygen (O) atoms in  $\text{Zn}[\text{H}_2\text{O}]_6^{2+}$  than in  $\text{Zn}[\text{H}_2\text{O}]_5[\text{THF}]^{2+}$ , the calculated average bond length in  $\text{Zn}[\text{H}_2\text{O}]_6^{2+}$  (2.06Å based on our DFT calculations) is longer than that in  $\text{Zn}[\text{H}_2\text{O}]_5[\text{THF}]^{2+}$  (1.98Å). Furthermore, based on the structures of 6  $\text{H}_2\text{O}$  / 5  $\text{H}_2\text{O}$  + 1



THF molecules as shown in **Figure 4.3**, more hydrogen bonds are broken in the process of forming  $\text{Zn}[\text{H}_2\text{O}]_6^{2+}$ , compared to the number of broken bonds in the formation of  $\text{Zn}[\text{H}_2\text{O}]_5[\text{THF}]^{2+}$ . These two factors could explain why  $\text{Zn}[\text{H}_2\text{O}]_5[\text{THF}]^{2+}$  has lower solvation energy than  $\text{Zn}[\text{H}_2\text{O}]_6^{2+}$ , which can decrease water activity.

**Table 4. 1** The total energy of the two solvation structures ( $E_{total}$ ), the energy of the  $\text{H}_2\text{O}/\text{H}_2\text{O}+\text{THF}$  molecule clusters ( $E_{\text{H}_2\text{O}/\text{THF}+\text{H}_2\text{O}}$ ), and the energy of the isolated  $\text{Zn}^{2+}$  ion ( $E_{\text{Zn}^{2+}}$ ). The corresponding solvation energies ( $E_{sol}$ ) for the two-solvation structure are calculated based on Eq. 2-1.

Species	Energy	$E_{sol}$
$E_{\text{Zn}^{2+}}$	+24.292eV	
$E_{\text{H}_2\text{O}}$	-87.738eV	
$E_{total(\text{Zn}[\text{H}_2\text{O}]_6^{2+})}$	-76.942eV	-13.496eV
$E_{\text{THF}+\text{H}_2\text{O}}$	-145.246eV	
$E_{total(\text{Zn}[\text{H}_2\text{O}]_5[\text{THF}]^{2+})}$	-135.781eV	-14.827eV

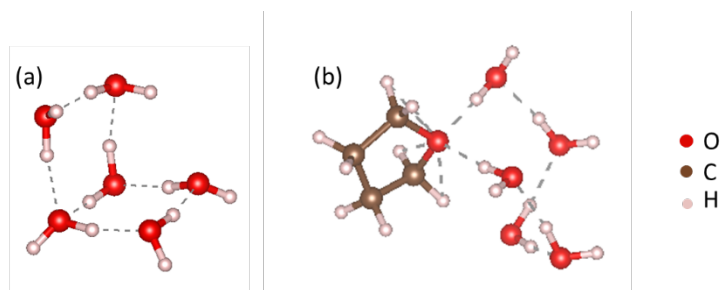


**Figure 4.3** The optimized structures of (a) 6 H<sub>2</sub>O molecule clusters with 7 hydrogen bonds (as represented by the grey dashed lines); and (b) 5 H<sub>2</sub>O and 1 THF molecule cluster with 10 hydrogen bonds.

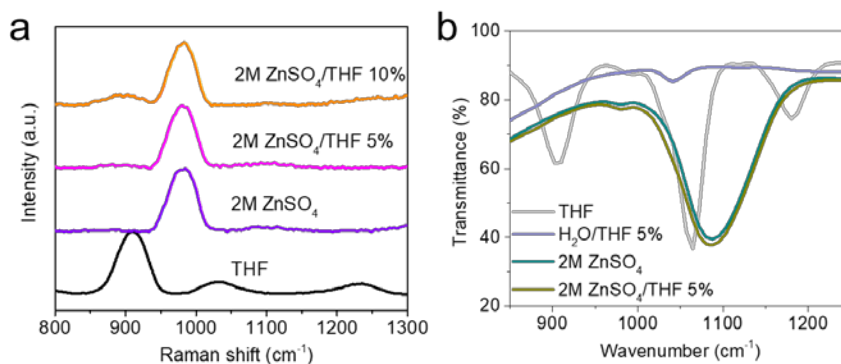


**Figure 4.4** (a) Raman spectra, and (b) FTIR spectra of the baseline 2 M ZnSO<sub>4</sub> and 2 M ZnSO<sub>4</sub>/THF 5% electrolytes.

**Figure 4.4 a** shows the Raman spectra of the prepared electrolytes and the pure THF solvent. The optimal 2 M ZnSO<sub>4</sub>/THF 5% shows an inconspicuous difference from the baseline 2 M ZnSO<sub>4</sub> electrolyte. The distinct peaks of THF disappear when a 5% THF additive is added to the 2 M ZnSO<sub>4</sub> electrolyte, but the peaks can be observed in 2 M ZnSO<sub>4</sub>/THF 10%. This finding indicates that a small quantity of THF (less than 10%) can be fully absorbed in the primary solvation shell of Zn<sup>2+</sup> by the hydrogen bond with H<sub>2</sub>O, decreasing the interaction between active H<sub>2</sub>O molecules and Zn<sup>2+</sup> to restrain the

generation of the byproducts. This phenomenon was evidenced by the FTIR spectroscopy, as shown in **Figure 4.4 b**. In the FTIR spectra profile, pure THF shows characteristic IR peaks at around 1180, 1065, and 903  $\text{cm}^{-1}$ , but these peaks cannot be found when 5% THF was mixed with 2 M  $\text{ZnSO}_4$  because of the formation between a small amount of THF and  $\text{H}_2\text{O}$ . Therefore, the IR peaks of bare 2 M  $\text{ZnSO}_4$  and 2 M  $\text{ZnSO}_4/\text{THF}$  5% electrolytes are almost overlapped. Digital images of electrolytes in vials are shown in **Figure 4.5**. Both 2 M  $\text{ZnSO}_4$  and 2 M  $\text{ZnSO}_4/\text{THF}$  5% electrolytes are transparent at the initial state, and they remain stable after 30 days.

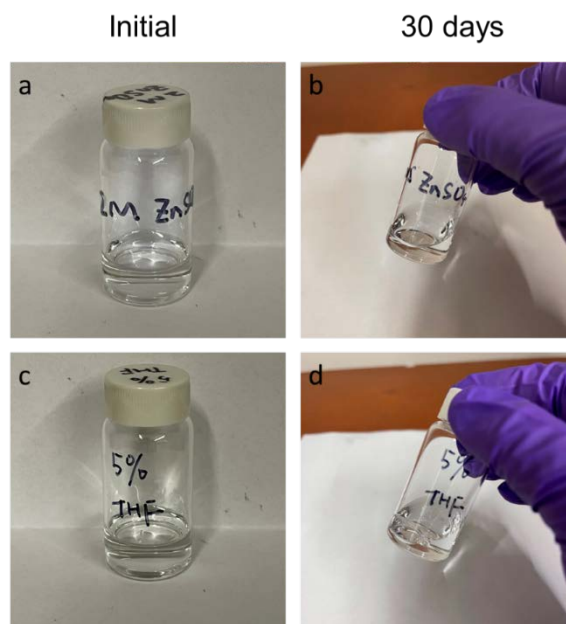


**Figure 4. 5** Digital images of the electrolytes in vials at the initial state and after 30 days.

(a, b) Baseline 2 M  $\text{ZnSO}_4$ , and (c, d) 2 M  $\text{ZnSO}_4/\text{THF}$  5%.

The wettability of 2 M  $\text{ZnSO}_4$  and  $\text{ZnSO}_4/\text{THF}$  5% electrolyte on zinc foil was characterized by the contact angle measurement. As shown in **Figure 4.6**, the contact angle of  $\text{ZnSO}_4/\text{THF}$  5% on the zinc foil is  $45^\circ$ , which is much smaller than that of the

baseline 2 M  $\text{ZnSO}_4$  ( $79^\circ$ ). The significantly decreased contact angle indicates the remarkably improved surface wettability of the  $\text{ZnSO}_4/\text{THF}$  5% electrolyte on the zinc foil. The good wettability of  $\text{ZnSO}_4/\text{THF}$  5% on the zinc foil leads to a more uniform deposition of  $\text{Zn}^{2+}$  on the surface of the Zn metal electrode, achieving and thus favoring the reversible and stable electrochemical behavior [181, 182].

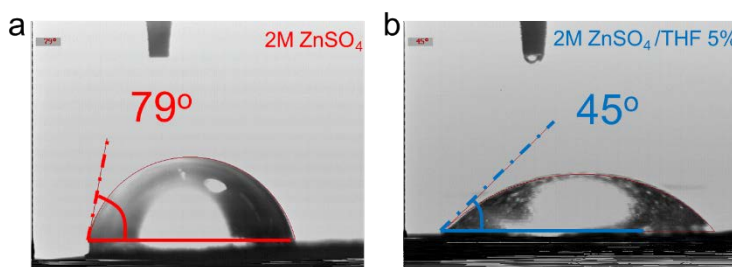


**Figure 4. 6** Contact angle measurement of (a) 2 M  $\text{ZnSO}_4$  and (b) 2 M  $\text{ZnSO}_4/\text{THF}$  5% on the Zn electrode.

#### 4.2.2 Electrochemical performance of the Zn||Cu asymmetrical Cell and Zn symmetrical cell

The electrochemical stability windows of various aqueous electrolytes were evaluated on the non-active titanium electrodes. As shown in **Figure 4.7**, the electrochemical stability window of the baseline 2 M  $\text{ZnSO}_4$  electrolyte is 2.28 V with a cathode limit of -0.01 V versus  $\text{Zn}^{2+}$  and an anodic limit of 2.27 V versus  $\text{Zn}^{2+}$ . In contrast, the 2 M  $\text{ZnSO}_4/\text{THF}$  5% electrolyte shows a wider stability window of ~2.38 V. 2 M  $\text{ZnSO}_4/\text{THF}$  5% was also found to have a slight extent in both the cathodic (-0.06 V vs  $\text{Zn}^{2+}$ , **Figure 4.7 b**) and anodic (2.32 V vs  $\text{Zn}^{2+}$ , **Figure 4.7 c**) limits [60].

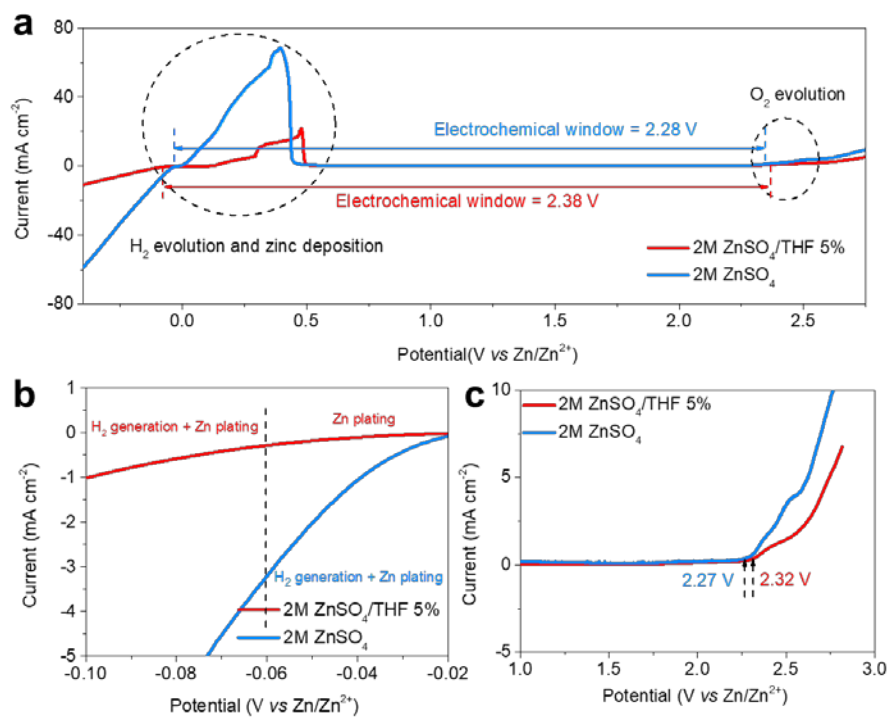


**Figure 4. 7** (a-c) The electrochemical stability window of the aqueous electrolytes measured using the polarization scanning at  $1 \text{ mV s}^{-1}$  on the non-active Ti electrodes between  $-0.5 \text{ V}$  and  $3.0 \text{ V}$  versus  $\text{Zn}^{2+}$ .

The transference number of  $\text{Zn}^{2+}$  ( $t_{\text{Zn}^{2+}}$ ) was based on measurements in symmetrical Zn cells with the help of EIS before and following CA tests and was determined using the following equation [183, 184]:

$$t_{\text{Zn}^{2+}} = \frac{I_s(\Delta V - I_0 R_0)}{I_0(\Delta V - I_s R_s)}$$

$\Delta V$  is the applied voltage (25 mV).  $I_0$  and  $I_s$  are the initial and steady-state currents, where  $R_0$  and  $R_s$  are initial and steady-state electrode resistances, respectively [185]. The  $\text{Zn}^{2+}$  transference number of the baseline 2 M  $\text{ZnSO}_4$  electrolyte is 0.36 based on the data from **Figure 4.8 a**, which is consistent with the references [186, 187]. On the other hand, the

optimal  $\text{Zn}^{2+}$  solvation configuration affects the transference number ( $t_{\text{Zn}^{2+}}$ ) in the 2 M  $\text{ZnSO}_4/\text{THF}$  5% electrolyte. As shown in **Figure 4.8 b**,  $t_{\text{Zn}^{2+}}$  is computed to be 0.51, higher than that of the baseline electrolyte, which suggests a faster migration speed of  $\text{Zn}^{2+}$  in  $\text{ZnSO}_4/\text{THF}$  5% [94, 186, 187].

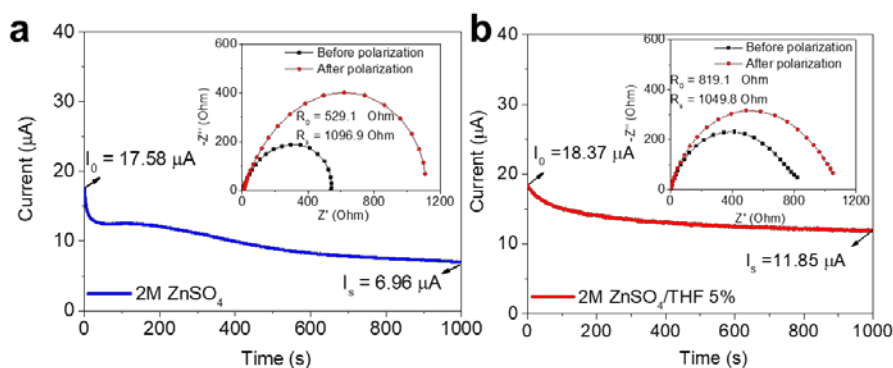


**Figure 4.8** (a) Current-time plots of the Zn symmetric cell with the 2 M  $\text{ZnSO}_4$  electrolyte after the application of a constant potential (25 mV) and the corresponding impedance spectra before and after polarization; (b) Current-time plots of the Zn symmetric cell with the  $\text{ZnSO}_4/\text{THF}$  5% electrolyte after the application of a constant potential (25 mV) and the corresponding impedance spectra before and after polarization.

The Tafel plots were obtained by the linear polarization measurements to confirm the effect of the THF additive on Zn corrosion. From the fitting data in **Figure 4.9**, the corrosion current density of the 2 M  $\text{ZnSO}_4/\text{THF}$  5% electrolyte is  $0.47 \text{ mA cm}^{-2}$ , which is greater than that of the baseline 2 M  $\text{ZnSO}_4$  with a corrosion current density of  $0.18 \text{ mA cm}^{-2}$ . However, the corrosion potential in the 2 M  $\text{ZnSO}_4/\text{THF}$  5% electrolyte increased to  $-0.92 \text{ V}$  from  $-1.01 \text{ V}$  in the baseline 2 M  $\text{ZnSO}_4$  electrolyte. The much more positive corrosion potential of the 2 M  $\text{ZnSO}_4/\text{THF}$  5% demonstrates less tendency toward corrosion reactions [188, 189].

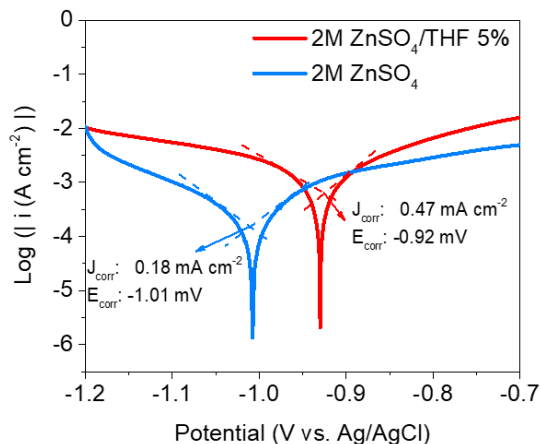


**Figure 4. 9** Comparison of the Tafel plots representing corrosion behavior of the Zn electrodes under different electrolyte systems.

The impact of the THF additive on CE of Zn plating/stripping was investigated on the Zn||Cu asymmetrical cells. As shown in **Figure 4.10 a**, the initial CE of the Zn||Cu cell at  $1 \text{ mA cm}^{-2}$  and  $1 \text{ mA h cm}^{-2}$  in the baseline 2 M ZnSO<sub>4</sub> electrolyte is 79.65 %, which is lower than that of in the ZnSO<sub>4</sub>/THF 5% electrolyte with a CE value of 89.39 %. The CE values of the Zn||Cu cells in these two electrolytes further increase to 99.9 % after 10 cycles and then remain stable and unchanged. For the Zn||Cu cell in the 2 M ZnSO<sub>4</sub> electrolyte, the CE value starts to fluctuate after 90 cycles and turns to failure just after 100 cycles, which is caused mainly by side reactions and dendritic deposition. An average CE of 95.73 % was obtained in the first 100 cycles. In contrast, the Zn||Cu cells with the THF additive displayed a significantly improved Zn plating/stripping reversibility, showing a stable CE after 430 cycles with a high average value of 99.59 %. **Figure 4.10 b** compares the plating/stripping curves of the Zn||Cu cells with different electrolytes. In the first cycle, the cell with the ZnSO<sub>4</sub>/THF 5% electrolyte displayed a higher voltage polarization of 107 mV than that with the 2 M ZnSO<sub>4</sub> electrolyte (39 mV).

The THF additive increased the overpotential of the Zn plating/stripping on the Cu surface due to the decreased ionic conductivity of the electrolyte. In the following second cycle, the overpotential of the Zn||Cu cell in the ZnSO<sub>4</sub>/THF 5% electrolyte reduced to 48 mV compared to 35 mV for the 2 M ZnSO<sub>4</sub> electrolyte. **Figure 4.10 c, d** shows the voltage profiles of the Zn plating/stripping on the Cu surface at selected cycles in the ZnSO<sub>4</sub>/THF 5% electrolyte. The curves almost overlapped in the 50th, 100th, and 200th cycles with a steady overpotential of 30 mV, suggesting excellent reversibility of the Zn metal anode in the ZnSO<sub>4</sub>/THF 5% electrolyte.

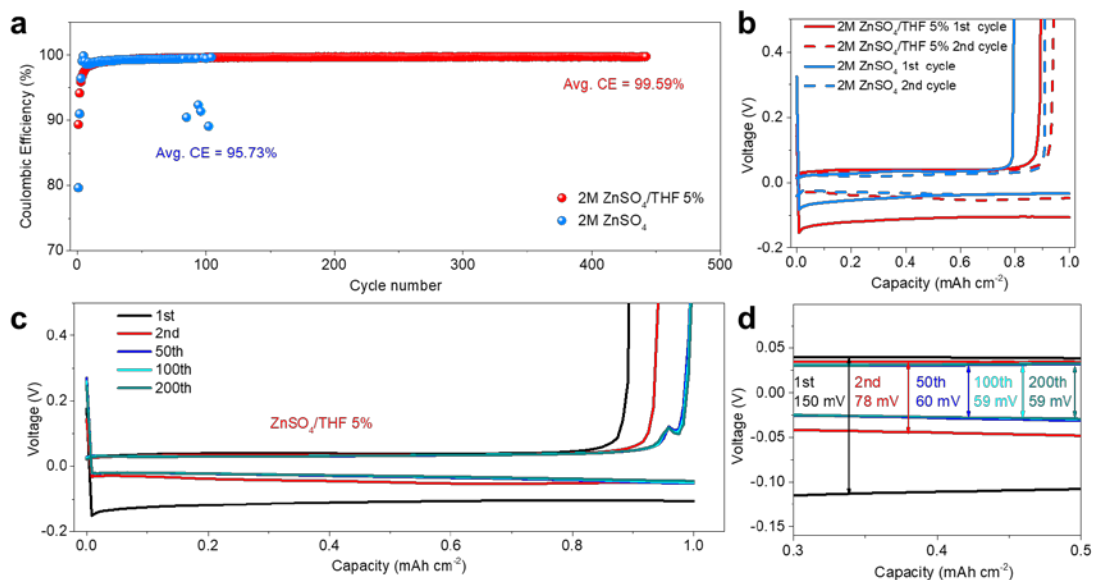


**Figure 4. 10** (a) Zn plating/stripping CE of the Zn||Cu cells with the different electrolytes. (b) Voltage profiles in the 2 M ZnSO<sub>4</sub> and 2 M ZnSO<sub>4</sub>/THF 5% electrolytes at the initial two cycles. (c, d) Voltage profiles of the Zn plating/stripping processes at selected cycles in the ZnSO<sub>4</sub>/THF 5% electrolyte.



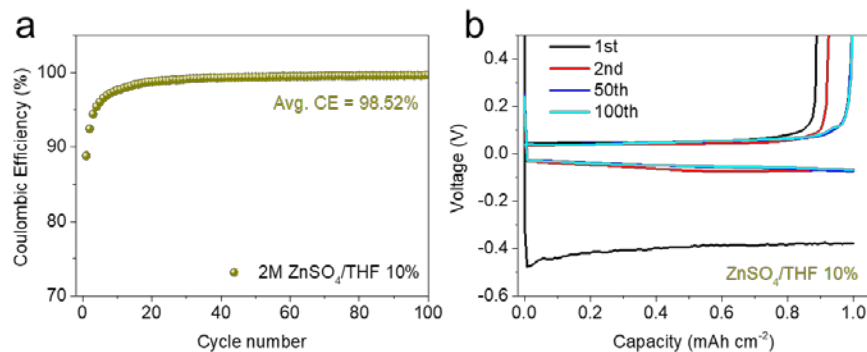


**Figure 4. 11** (a) CE of the Zn||Cu cells with the ZnSO<sub>4</sub>/THF 10% electrolyte. (b) profiles of the Zn plating/stripping processes at selected cycles.

The CE of the Zn||Cu asymmetrical cell with the ZnSO<sub>4</sub>/THF 10% electrolyte is shown in **Figure 4.11**. An average CE of 98.52% is obtained over 100 cycles in the ZnSO<sub>4</sub>/THF 10% electrolyte, which is higher than that of the baseline 2 M ZnSO<sub>4</sub> electrolyte (95.73%) but lower than that of the optimized ZnSO<sub>4</sub>/THF 5% electrolyte (99.59%). Besides, the cell with the ZnSO<sub>4</sub>/THF 10% electrolyte shows a very high voltage polarization of over 400 mV in the first cycle because of the redundant THF molecules, resulting in damage to the overall electrochemical performance.

To optimize the content of THF in the 2 M ZnSO<sub>4</sub> electrolyte, voltage-time profiles of the Zn symmetric cells with the different electrolytes are shown in **Figure 4.12 a**. It can be found that the longest plating/stripping cycles were achieved in the presence of 5% THF (by volume) in 2 M ZnSO<sub>4</sub>, i.e., ZnSO<sub>4</sub>/THF 5%. With the addition of THF, the overpotential is larger than that of the baseline 2 M ZnSO<sub>4</sub> electrolyte (**Figure 4.12 b, c**). The overpotential increase slightly with an increase in the THF concentration from 2.5 to 7.5% by volume. When the concentration of the THF additive reaches 10%, the overpotential of the Zn symmetric cell surges to more than 300 mV. Thus, 5% is

considered the optimal concentration of THF in the 2 M ZnSO<sub>4</sub> electrolyte. Further measurements, characterizations, and comparisons were based on the baseline 2 M ZnSO<sub>4</sub> and ZnSO<sub>4</sub>/THF 5% unless stated.

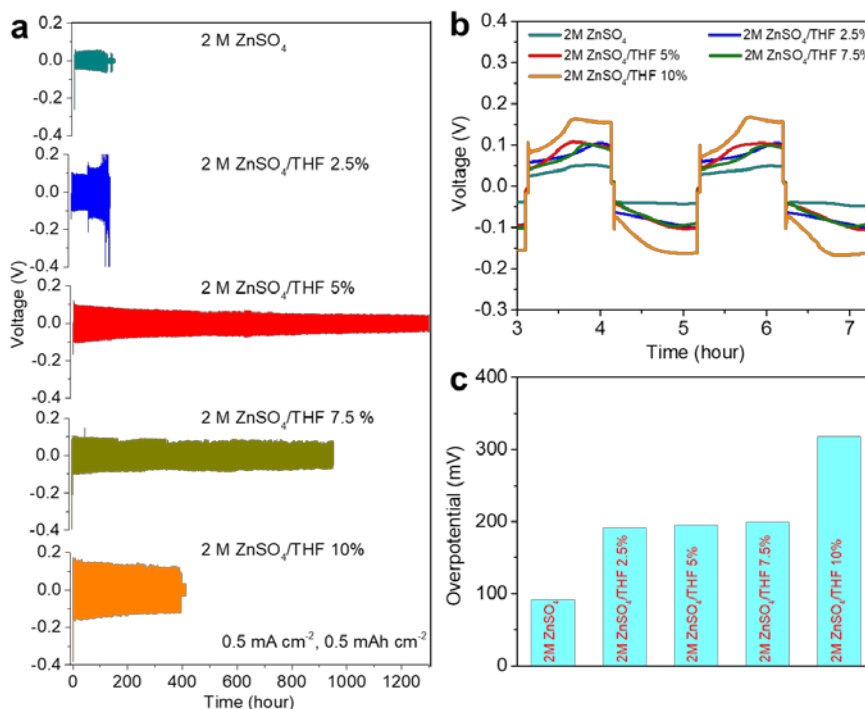


**Figure 4.12** (a) Galvanostatic Zn plating/stripping in the Zn symmetrical cell at 0.5 mA cm<sup>-2</sup> and 0.5 mA h cm<sup>-2</sup>. (b) Voltage profiles of the Zn symmetric cells at 0.5 mA cm<sup>-2</sup> and 0.5 mA h cm<sup>-2</sup>. (c) The corresponding overpotential of Zn symmetric cells at 0.5 mA cm<sup>-2</sup>.

According to **Figure 4.13**, when the cells were tested at a current density of 0.5 mA cm<sup>-2</sup> with a capacity of 0.5 mA h cm<sup>-2</sup>, the cell with the 2 M ZnSO<sub>4</sub> electrolyte failed after only 120 h, while it can reach an ultralong cycling life of over 1300 h with the ZnSO<sub>4</sub>/THF 5% electrolyte. Meanwhile, the cell in 2 M ZnSO<sub>4</sub> exhibits a stable polarization overpotential of ~ 47 mV at the beginning, which is smaller than that of

ZnSO<sub>4</sub>/THF 5% (~ 75 mV), and after that, a sudden and irreversible decrease of the polarization voltage appeared, and then the cell failed due to Zn dendrite growth. As a comparison, the overpotential of Zn symmetrical cell in ZnSO<sub>4</sub>/THF 5% remains stable over 1300 h in **Figure 4.13 d**. The overpotential of the cell with the ZnSO<sub>4</sub>/THF 5% electrolyte is larger than that of 2 M ZnSO<sub>4</sub>, which is attributed to the introduction of the THF additive slightly reducing the ionic conductivity and increasing the resistance.

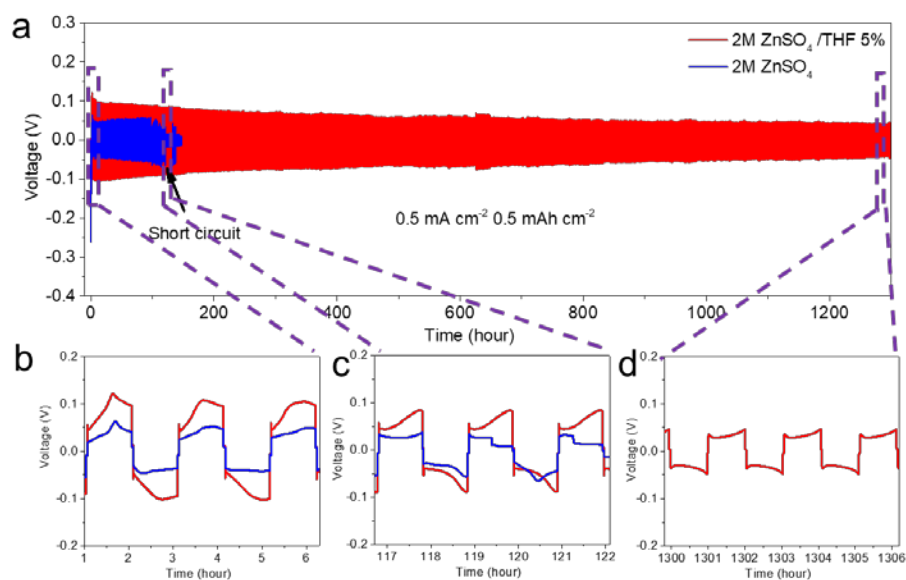


**Figure 4. 13** (a-d) Galvanostatic Zn plating/stripping in the Zn symmetrical cell at 0.5 mA cm<sup>-2</sup> and 0.5 mA h cm<sup>-2</sup>.

The equivalent circuit of the EIS tests based on the Zn symmetrical cell is shown in **Figure 4.14 a**.  $R_s$  and  $R_{ct}$  are the electrolyte resistance and the charge-transfer resistance, respectively. CPE is the constant phase elements to fit capacitances. According to **Figure 4.14 b**, the EIS spectra of the baseline 2 M ZnSO<sub>4</sub> electrolyte and 2 M ZnSO<sub>4</sub>/THF 5% electrolytes display only one semi-circle, indicating a simple charge transfer at the Zn-electrolyte interface. The electrolyte with the THF additive shows a larger charge-transfer

resistance before and after cycling compared with the baseline 2 M ZnSO<sub>4</sub> electrolyte. It suggests that the Zn<sup>2+</sup> deposition ability is reduced by introducing THF additive, which is consistent with the overpotential behavior in the Zn symmetrical cell. The ionic conductivity ( $\sigma$ ) can be evaluated from the EIS spectra by the following equation:

$$\sigma = \frac{L}{R_s S} \quad (5.2)$$

Where  $R_s$  represents the electrode resistance according to the EIS measurement,  $L$  represents the length of the testing cell, and  $S$  is the contact area between the electrode and the electrolyte in the testing cell. **Figure 4.14c** reveals that the electrolyte with THF additive has a larger electrolyte resistance, suggesting the decrease in the ionic conductivity of the 2 M ZnSO<sub>4</sub>/THF 5% electrolyte. The EIS result in **Figure 4.14** confirms that both electrolyte resistance and the charge transfer resistance of 2 M ZnSO<sub>4</sub>/THF 5% are greater than that of the baseline 2 M ZnSO<sub>4</sub>, suggesting the decrease in the ionic conductivity due to the introduction of the organic THF additive.

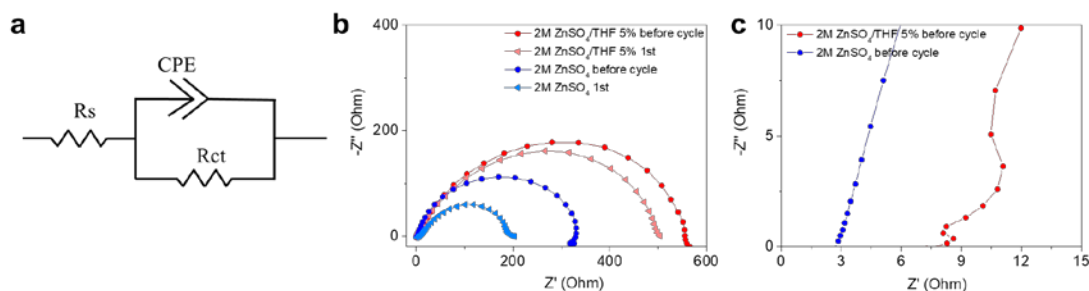


**Figure 4. 14** (a) The equivalent circuit of the EIS tests based on the Zn symmetrical cell, and (b, c) Nyquist plots of the baseline 2 M ZnSO<sub>4</sub> electrolyte and the 2 M ZnSO<sub>4</sub>/THF 5% electrolytes.

At a higher current density of  $1 \text{ mA cm}^{-2}$  and a capacity of  $1 \text{ mA h cm}^{-2}$ , the cells with  $2 \text{ M ZnSO}_4$  display inferior cycle stability of only 40 h (**Figure 4.15 a**). After introducing a 5% THF additive into the electrolyte, the Zn symmetrical cell can achieve a prolonged cycle life of over 500 h. The cycling stability of the Zn symmetrical cell in  $2 \text{ M ZnSO}_4/\text{THF } 5\%$  was further tested under a very high current density of  $5 \text{ mA cm}^{-2}$  with a capacity of  $1 \text{ mA h cm}^{-2}$  (**Figure 4.15 b**). The result also reveals a great improvement in cycling stability, in which the cell with the baseline  $2 \text{ M ZnSO}_4$  electrolyte lasted for only 60 h while the cell with the  $2 \text{ M ZnSO}_4/\text{THF } 5\%$  electrolyte showed excellent cycling performance over 600 h. These results show a 10-fold improvement in cycle life at different current densities, demonstrating that the THF additive can suppress the side reactions and dendrite growth to boost cycling stability.

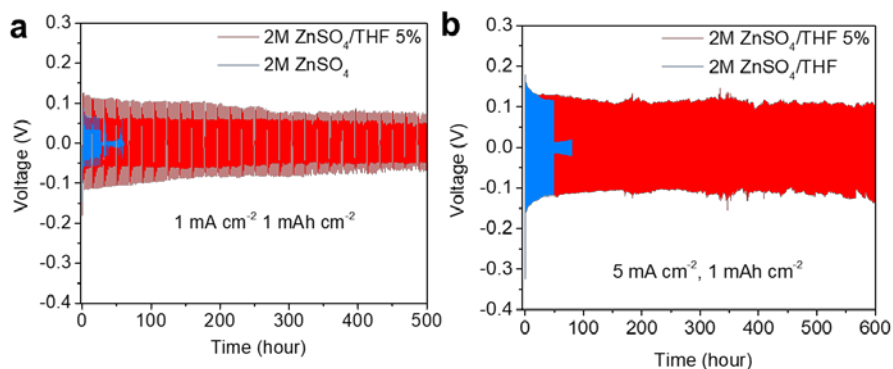


**Figure 4.15** Galvanostatic Zn plating/stripping in the Zn symmetrical cell at (d)  $1 \text{ mA cm}^{-2}$  and  $1 \text{ mA h cm}^{-2}$  and (e) at  $5 \text{ mA cm}^{-2}$  and  $1 \text{ mA h cm}^{-2}$ .

In **Figure 4.16**, the overcharge tests of the Zn symmetric cells in the  $2 \text{ M ZnSO}_4$  and  $\text{ZnSO}_4/\text{THF } 5\%$  electrolytes were conducted at a current density of  $1 \text{ mA cm}^{-2}$ . The discharge capacity of the Zn metal electrode can reach over  $48 \text{ mA h cm}^{-2}$  in  $\text{ZnSO}_4/\text{THF } 5\%$ , while that of the pure  $2 \text{ M ZnSO}_4$  electrolyte is less than  $20 \text{ mA h cm}^{-2}$  before the

cells short-circuited. The excellent overcharge performance reveals that the THF additive has the potential to achieve better reversibility and higher rate capability. The plating/stripping hours of 2 M ZnSO<sub>4</sub>/THF 5% are compared to the previously reported literature as summarized in **Table 4.2**. It is found that the THF additive can achieve long plating/stripping performance at various current densities. The excellent cycling stability of the cells with the 2 M ZnSO<sub>4</sub>/THF 5% electrolyte is attributed to the THF additive, which can decrease the water activity to suppress the HER and byproduct precipitation.

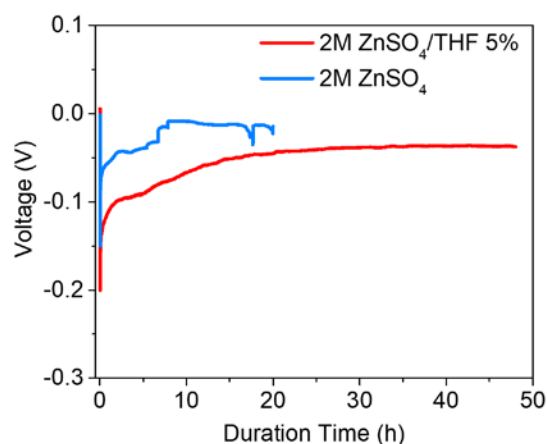


**Figure 4.16** Overcharging test of the Zn symmetric cells at 1 mA cm<sup>-2</sup>.

**Table 4.2** The comparison of the plating/stripping hours in AZIBs with other previous works.

Ref.	Works	Plating/stripping in Zn symmetrical cells	
		Time (h)	Current density / Capacity mA cm <sup>-2</sup> / mA h cm <sup>-2</sup>
[95]	Dimethyl sulfoxide (DMSO) additive in the	~ 1000	0.5 / 0.5

	ZnCl <sub>2</sub> electrolyte		
[190]	Tetrabutylammonium sulfate (TBA <sub>2</sub> SO <sub>4</sub> ) as a cationic surfactant-type additive in the ZnSO <sub>4</sub> electrolyte	~ 300	2 / 2
		~ 160	5 / 5
[100]	Diethyl ether (Et <sub>2</sub> O) as self-healing additive in the Zn(CF <sub>3</sub> SO <sub>3</sub> ) <sub>2</sub> electrolyte	~ 250	0.2 / 0.2
[191]	Lithium chloride (LiCl) additive in the ZnSO <sub>4</sub> electrolyte	~ 170	0.2 / 0.034
[192]	Vanillin Additive in the ZnSO <sub>4</sub> electrolyte	~ 1000	1 / 1
		~ 1000	1 / 5
[193]	Polyacrylamide (PAM) additive in the ZnSO <sub>4</sub> electrolyte	~ 180	1 / 1
		~ 280	2 / 4
Our work	Tetrahydrofuran (THF) additive in the ZnSO <sub>4</sub> electrolyte	~ <b>1300</b>	<b>0.5 / 0.5</b>
		~ <b>500</b>	<b>1 / 1</b>
		~ <b>600</b>	<b>5 / 1</b>

**Figure 4.17** depicts that the Zn electrode can be easily corroded under the traditional baseline  $\text{ZnSO}_4$  electrolyte upon cycling, while smooth plating of Zn can be achieved with the existence of the THF additive in the  $\text{ZnSO}_4$  electrolyte. This is because the solvation structure of the Zn hydration layer can be optimized by the THF additive, suppressing the side reactions and dendrite growth during the Zn plating/stripping processes.

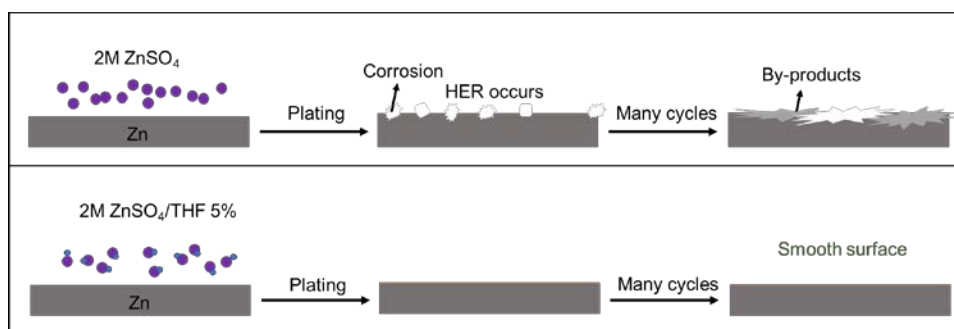


**Figure 4. 17** Illustration of surface evolution mechanism with and without the THF additive.

#### 4.2.3 Cycled Zn electrode characterizations

XRD was further employed to investigate the crystal structure of the Zn electrode after Zn deposition. The XRD profiles of bare Zn and Zn foil after plating in 2 M  $\text{ZnSO}_4$  and  $\text{ZnSO}_4/\text{THF}$  5% are illustrated in **Figure 4.18**. Some new peaks located at  $17^\circ$  and  $26^\circ$  emerged after the Zn plating in the baseline 2 M  $\text{ZnSO}_4$  electrolyte, which is consistent with  $\text{Zn}_4\text{SO}_4(\text{OH})_6 \cdot x\text{H}_2\text{O}$  [194, 195]. In contrast, with a 5% THF additive in the 2 M  $\text{ZnSO}_4$  electrolyte, the peaks of the byproduct  $\text{Zn}_4\text{SO}_4(\text{OH})_6 \cdot x\text{H}_2\text{O}$  disappeared in the XRD pattern. Therefore, the THF additive in the  $\text{ZnSO}_4$  electrolyte can significantly suppress the generation of byproducts of  $\text{Zn}_4\text{SO}_4(\text{OH})_6 \cdot x\text{H}_2\text{O}$  by modulating the solvated structure of the Zn hydration layer.



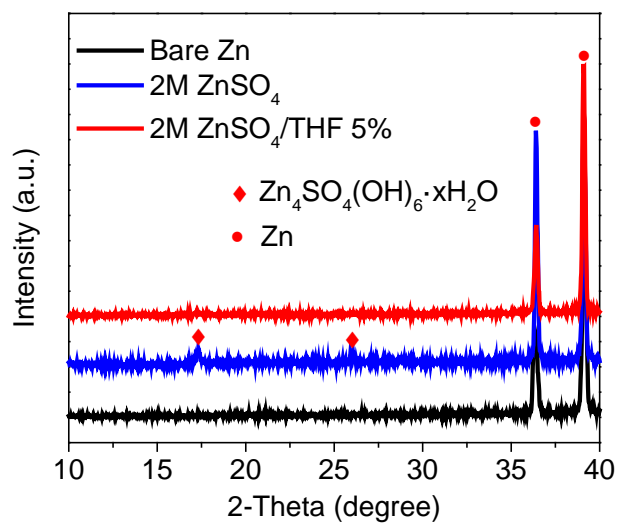


**Figure 4. 18** XRD patterns of the Zn foil after 100 cycles at  $0.5 \text{ mA cm}^{-2}$  and  $0.5 \text{ mA h cm}^{-2}$ .

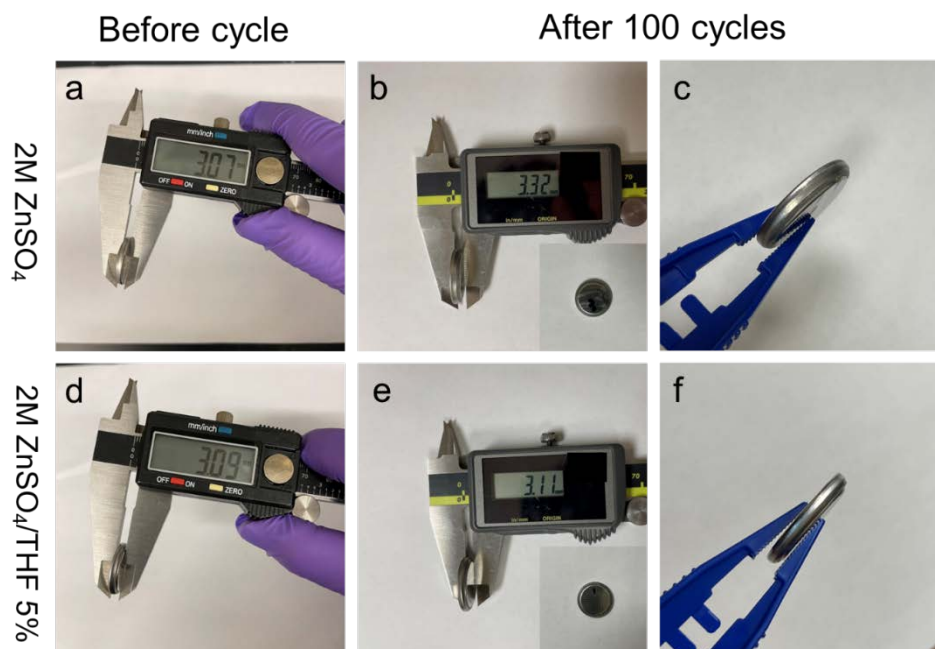


**Figure 4. 19** Volume expansion comparison of (a-c) 2 M  $\text{ZnSO}_4$ , (d-f) 2 M  $\text{ZnSO}_4$ / THF 5% symmetric cells after 100 cycles.

The volume expansion comparison after cycles of the Zn symmetrical cells with different electrolytes is displayed in **Figure 4.19**. The thickness of the coin cell with the baseline 2 M ZnSO<sub>4</sub> electrolyte increases from 3.07 to 3.32 cm after 100 cycles because of the release of H<sub>2</sub>, while there is only a slight increase (3.09 to 3.11 cm) for 2 M ZnSO<sub>4</sub>/THF 5% after 100 cycles.

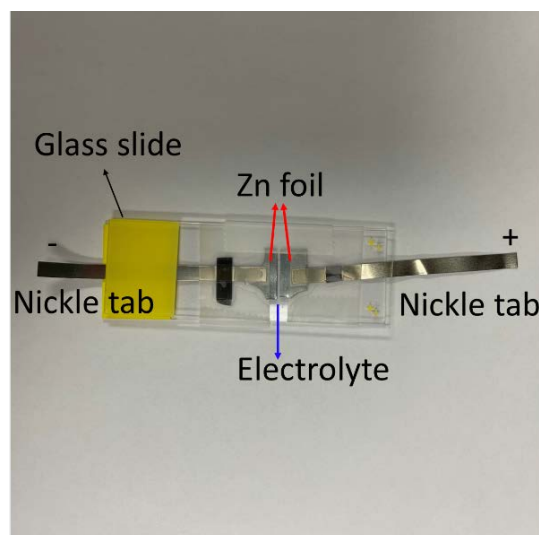


**Figure 4. 20** Photograph of the home-built devices for in situ monitoring of the H<sub>2</sub> evolution.

Moreover, a home-built device was developed for in situ monitoring of HER (**Figure 4.20**). To build the cell for the in-situ monitoring of hydrogen gas evolution, two glass slides were stacked on top of each other to act as the cell shell. Two small pieces of the Zn electrode connecting with the nickel tabs were placed close to each other but insulated. The electrolytes were injected to the void space between the two Zn electrodes by the pipette. After that, the home-made cells were sealed by the scotch tape. The as-designed cells were tested at a current density of 10 mA cm<sup>-2</sup>, where an optical microscope was used to detect the generation of the bubbles. As shown in **Figure 4.21 a**, some bubbles

are generated on the surface of the Zn electrode in the baseline 2 M ZnSO<sub>4</sub> electrolyte after 5 min, and more bubbles are found after 10 min. In contrast, the bubbles are barely detected in the electrolyte with the THF additive, indicating that the HER has been suppressed by the THF additive (**Figure 4.21 b**).

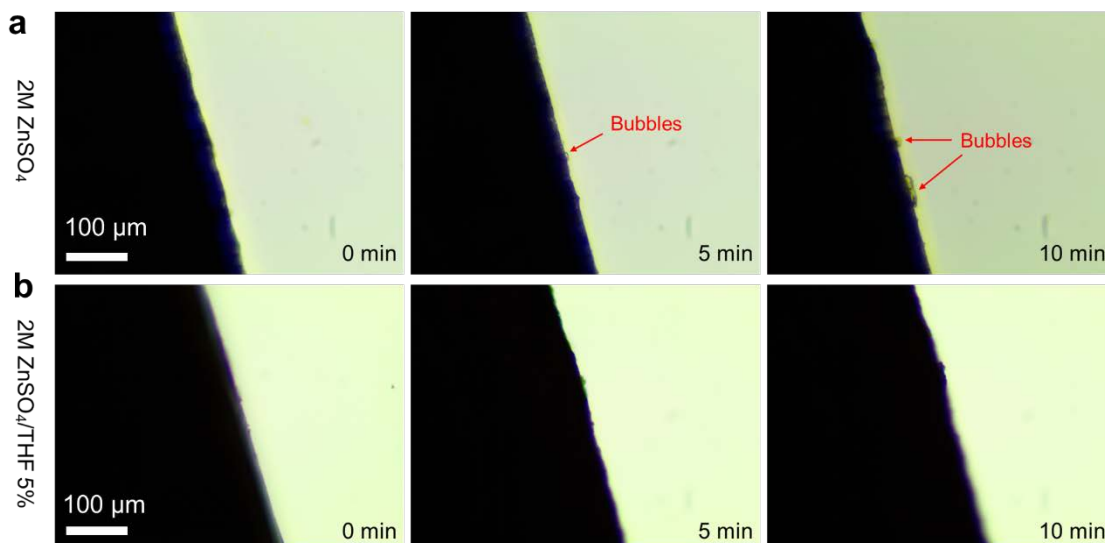


**Figure 4. 21** (a, b) *In-situ* optical microscopy of the H<sub>2</sub> generation in 2 M ZnSO<sub>4</sub> and 2 M ZnSO<sub>4</sub>/THF 5% in the symmetrical cells at a current density of 10 mA cm<sup>-2</sup>.

The surface morphologies of the Zn electrode before and after 100 plating/stripping cycles in the 2 M ZnSO<sub>4</sub> and ZnSO<sub>4</sub>/THF 5% electrolytes are investigated by the photographs and SEM. The optical images of the Zn electrode after 100 cycles reveal that the surface of the Zn electrode in 2 M ZnSO<sub>4</sub> is coarse, while it shows a smooth surface in the 2 M ZnSO<sub>4</sub>/THF 5% electrolyte (**Figure 4.22**). According to SEM images in **Figure 4.23**, the surface of the Zn electrode before cycling is smooth with some grooves.

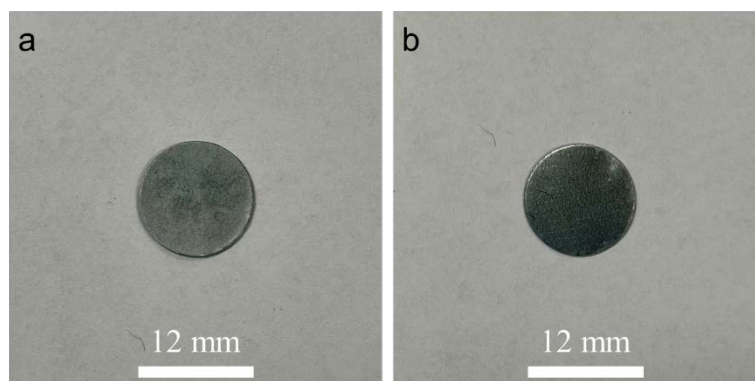


**Figure 4. 22** The optical images of the Zn electrodes in (a) 2 M ZnSO<sub>4</sub> and (b) 2 M ZnSO<sub>4</sub>/THF 5% after 100 cycles.

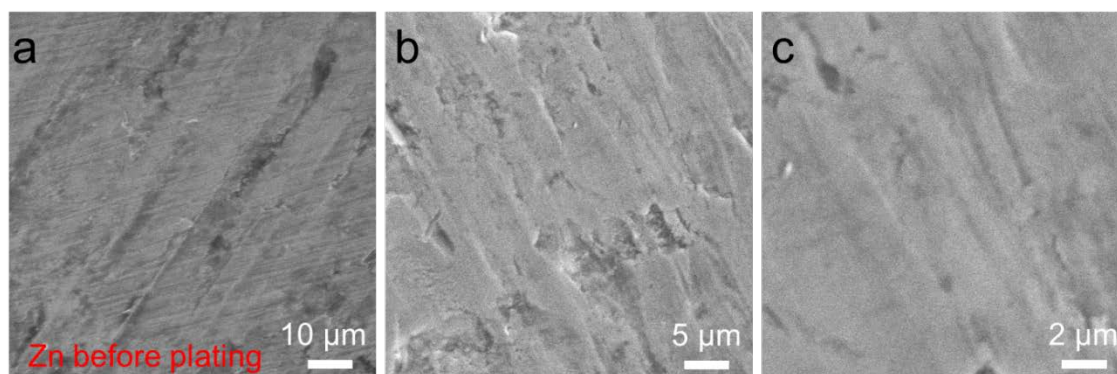


**Figure 4. 23** (a-c) The SEM images of the Zn electrode before plating.

After 100 plating/stripping cycles in the baseline 2 M ZnSO<sub>4</sub> at a current density of 0.5 mA cm<sup>-2</sup> and a capacity of 0.5 mA h cm<sup>-2</sup>, the surface of the Zn electrode is severely eroded to be quite rough and uneven, as shown in **Figure 4.24 a**. Besides, many tiny particles of the byproducts adhere to the surface of the zinc metal electrode (**Figure 4.24 b**). This structure with erosion surface and “dead Zn” can increase the surface area between the electrode and electrolyte to reduce the CE and capacity of AZIBs, as well as provide more reaction sites for side reactions. The EDS elemental mapping of the Zn electrodes after 100 plating/stripping cycles was performed to further investigate the

distribution of the elements on the surface (**Figure 4.24 c**). The EDS mapping finds widespread O and S on the surface of the Zn electrode with the 2 M ZnSO<sub>4</sub> electrolyte, corresponding to the formation of the byproduct of Zn<sub>4</sub>SO<sub>4</sub>(OH)<sub>6</sub>·xH<sub>2</sub>O. The surface of the Zn electrode in the ZnSO<sub>4</sub>/THF 5% electrolyte, which is comparable to the original Zn foil morphology, is much smoother than that of the baseline 2 M ZnSO<sub>4</sub> electrolyte (**Figure 4.24 d, e**). According to the EDS mapping in **Figure 4.24 f**, it can be observed that the Zn element covers the whole surface with the 2 M ZnSO<sub>4</sub>/THF 5% electrolyte, while little O and S can be detected. These results have successfully proven that the THF additive can inhibit side reactions including the HER and byproduct precipitation because of the decrease in water activity.

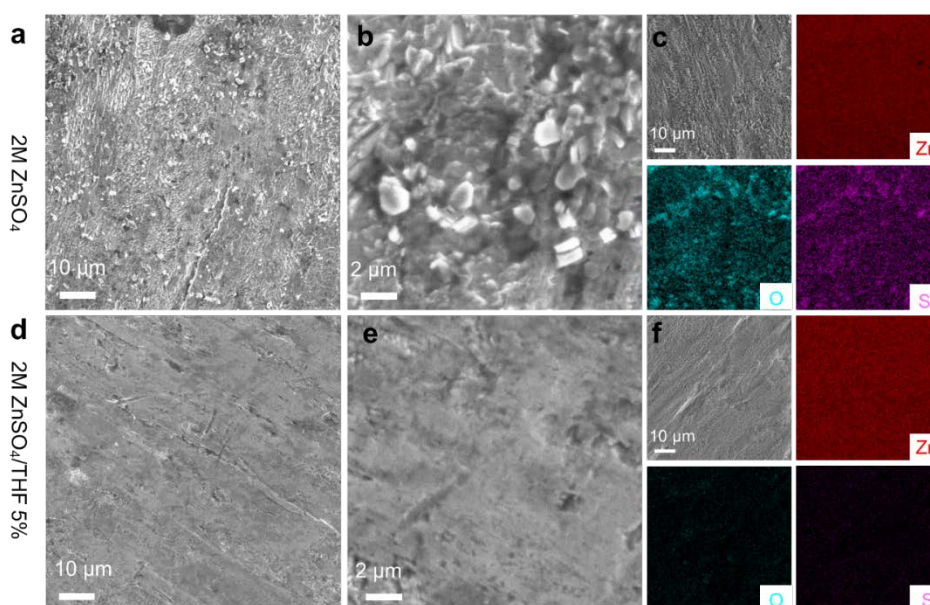


**Figure 4. 24** SEM images of (c, d) Zn electrode after 100th plating in 2 M ZnSO<sub>4</sub>, and (e) corresponding EDS mapping. SEM images of (f, g) Zn electrode after 100th plating in 2 M ZnSO<sub>4</sub>/THF 5%, and (h) corresponding EDS mapping.

#### 4.2.4 Full cell evaluation

To evaluate the practical application of the ZnSO<sub>4</sub>/THF 5% electrolyte, the full cell with Zn as the anode and β-MnO<sub>2</sub> as the cathode (a tunnel structure) was assembled and tested. MnO<sub>2</sub> is one of the most promising cathodes for AZIBs due to its high theoretical capacity of 308 mA h g<sup>-1</sup> [196, 197]. To address the issue of the dissolution loss of the MnO<sub>2</sub> active material upon cycling, the MnSO<sub>4</sub> salt was added to the electrolytes with a concentration of 0.1 M. **Figure 4.25 a** shows the CV curves of the Zn||MnO<sub>2</sub> cells in 2 M ZnSO<sub>4</sub> and ZnSO<sub>4</sub>/THF 5% electrolytes at a scan rate of 0.1 mV s<sup>-1</sup>. The MnO<sub>2</sub> electrode in different electrolytes shows similar behavior with distinct Mn-ion redox peaks. A smaller overpotential gap is observed in the CV curve for the ZnSO<sub>4</sub>/THF 5% electrolyte compared with that using the 2 M ZnSO<sub>4</sub> electrolyte, which is consistent with the voltage profiles of the galvanostatic charge/discharge as shown in **Figure 4.25 b**. The cell with the ZnSO<sub>4</sub>/THF 5% electrolyte also shows a smaller charge-transfer resistance (R<sub>ct</sub>) than that with the baseline 2 M ZnSO<sub>4</sub> electrolyte (**Figure 4.25 c**). This may be because the THF organic additive promotes the infiltration of the electrolyte into the MnO<sub>2</sub> electrode, as well as wetting the MnO<sub>2</sub> active material with PVDF binder. **Figure 4.25 d** shows the rate performance of the different electrolytes at various current densities from 100 to 5000 mA g<sup>-1</sup>. The result shows that cells with different electrolytes deliver similar capacities at a low current density of 100 mA g<sup>-1</sup>, but the cell with the THF additive shows higher capacities than that with the baseline 2 M ZnSO<sub>4</sub> electrolyte with the increase in the current densities. The cycling properties of the Zn||MnO<sub>2</sub> cell were tested at a current density of 500 mA g<sup>-1</sup> after the activation at a small current density of 100 mA g<sup>-1</sup> for the initial two cycles. As shown in **Figure 4.25e**, the MnO<sub>2</sub> cathode in the

ZnSO<sub>4</sub>/THF 5% electrolyte delivers a capacity of 225.2 mA h g<sup>-1</sup> after 250 cycles, decreasing from 231.3 mA h g<sup>-1</sup> in the third cycle with a capacity retention of 97.56%. The capacity of the Zn||MnO<sub>2</sub> batteries with the 2 M ZnSO<sub>4</sub>/THF 5% electrolyte is on the rise from the 50th cycle to the 240th cycle because of the addition of MnSO<sub>4</sub> and THF. MnSO<sub>4</sub> can provide the additional Mn<sup>2+</sup> in the electrolytes, which would be electrochemically oxidized to MnO<sub>x</sub> on the MnO<sub>2</sub> electrode to provide additional capacity. Meanwhile, the THF additive shows the capability of decreasing the water activity, which may be able to prevent the dissolution loss of MnO<sub>2</sub>. By comparison, the MnO<sub>2</sub> cathode in the baseline 2 M ZnSO<sub>4</sub> electrolyte exhibits inferior cycling stability where the capacity decreases dramatically to 130.8 mA h g<sup>-1</sup> after 100 cycles with a capacity retention of 62.05%.

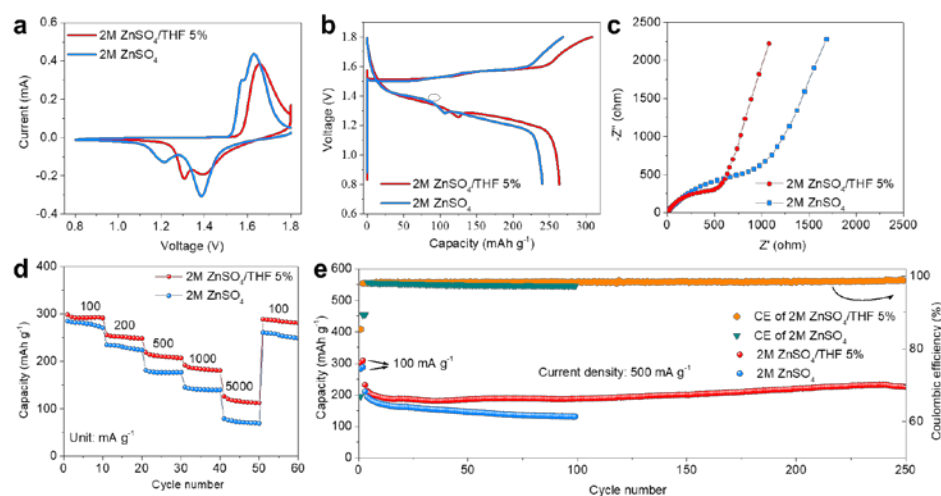


**Figure 4.25** Electrochemical performance of the Zn||MnO<sub>2</sub> cells in the different electrolytes. (a) CV at a scan rate of 0.1 mV s<sup>-1</sup>. (b) Charge-discharge profiles. (c) EIS spectra. (d) Rate performance. (e) Cyclic stability at 500 mA g<sup>-1</sup>.

**Figure 5.26** shows the 1st, 2nd, 10th, 50th, and 100th capacity-voltage profiles of the full cell with the Zn metal electrode in the ZnSO<sub>4</sub>/THF 5% electrolyte. The curves of the 10th, 50th, and 100th nearly overlapped, revealing that the Zn metal anode has a stable and reversible electrochemical behavior in the ZnSO<sub>4</sub>/THF 5% electrolyte. This full cell result shows the proof of concept and the promise for practical application.

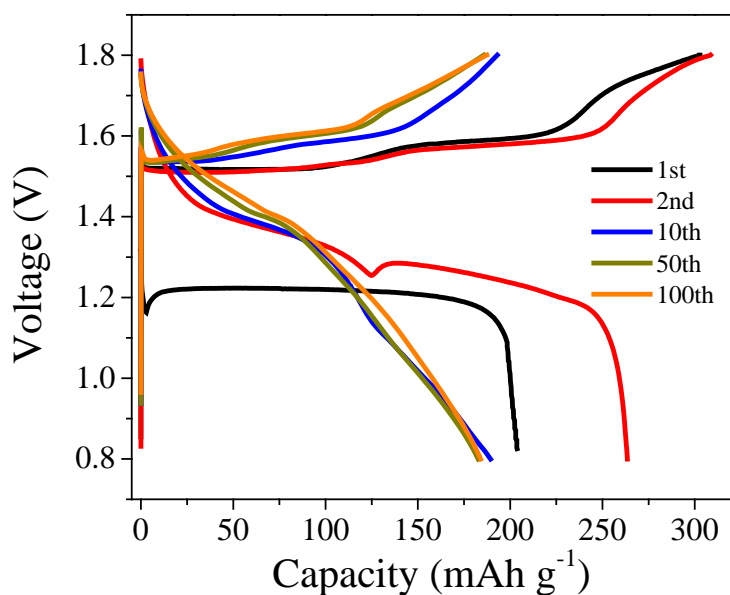


**Figure 4. 26** Charge-discharge profiles at selected cycles of the Zn||MnO<sub>2</sub> cells in the 2 M ZnSO<sub>4</sub>/THF 5% electrolyte.

### 4.3 Conclusions

A common and low-cost cyclic ether of THF was introduced into the 2 M ZnSO<sub>4</sub> electrolyte. THF as a proton acceptor can form a hydrogen bond with H<sub>2</sub>O. Thus, it can optimize the solvation structure of the Zn hydration layer to decrease the water activity. The water-induced undesired reactions are therefore suppressed, which can improve the electrochemical behavior of the zinc metal anode with good cycling stability and high CE.



The  $\text{Zn}^{2+}$  plating/stripping tests confirm that 5% THF (by volume) is considered the optimal concentration in the 2 M  $\text{ZnSO}_4$  electrolyte. The Zn symmetrical cell in the  $\text{ZnSO}_4/\text{THF}$  5% electrolyte exhibits an ultralong cycle life of more than 1300 h at  $0.5 \text{ mA cm}^{-2}$  with a capacity of  $0.5 \text{ mA h cm}^{-2}$ . According to the ex-situ SEM images, the surface of the Zn electrode became much smoother after plating/stripping cycling in the  $\text{ZnSO}_4/\text{THF}$  5% electrolyte than that in the baseline 2 M  $\text{ZnSO}_4$  electrolyte. The THF additive also enables a high CE in the Zn||Cu cells with an average value of 99.59% over 430 cycles. The  $\text{MnO}_2$  cathode in the Zn|| $\text{MnO}_2$  full cell with the  $\text{ZnSO}_4/\text{THF}$  5% electrolyte delivers a high reversible capacity of  $225 \text{ mA h g}^{-1}$  after 250 cycles with a capacity retention of 97.56%.

## Chapter 5 Conclusion and Future Work

### 5.1 Conclusions

Three types of the anode materials have been developed with high capacities and long cycling life for SIBs. The Sn@CFC anode with high mass loading was fabricated by electrospinning technology, which is free-standing and can be used as electrode directly without binder and carbon black. The novel SnP<sub>2</sub>O<sub>7</sub>@C anode prepared by sintering and ball-milling process delivers ultralong cycling life, which is achieved by the unique structure design that the SnP<sub>2</sub>O<sub>7</sub> nanoparticles remain active throughout the whole cycling life. The SnS/Sb<sub>2</sub>S<sub>3</sub>@SNC anode is made of the SnS/Sb<sub>2</sub>S<sub>3</sub> heterostructure encapsulated in S, N co-doped carbon with the engineered porous structure. Benefiting from the synergistic effect of the unique structure design, the SnS/Sb<sub>2</sub>S<sub>3</sub>@SNC anode shows enhanced cycling stability and improved rate performance.

An organic additive of THF was introduced into the baseline ZnSO<sub>4</sub> electrolyte to enhance the performance of AZIBs. The THF additive can play as a proton acceptor to form hydrogen bonds with the H<sub>2</sub>O molecules to reduce H<sub>2</sub>O activity and suppress H<sub>2</sub>O reduction, thus it can suppress the water-induced side reactions such as HER and byproduct precipitation. The THF can significantly improve the cycling life of AZIBs.

The as-prepared anodes and electrolytes were characterized by SEM, XRD, FTIR TGA, XPS, FTIR and Raman spectroscopy. Electrochemical tests were performed to study cycling stabilities and rate performance of SIBs, and zinc plating and stripping stability. The main conclusions are as following:

(1) The facile manufacturing technique yields the Sn@CFC electrode with an extremely high mass loading of  $5.5 \text{ mg cm}^{-2}$  with very little sacrifice of the electrochemical performances. The cross-link CF with N-doping and Sn nanoparticles together provide fast ions and electrons pathway, enabling a dominant pseudocapacitance contribution of 87.1% at a scan rate of  $0.5 \text{ mV s}^{-1}$ .

(2) The Sn@CFC electrode shows a high area capacity of  $1.68 \text{ mA h cm}^{-2}$  and a superior cyclic stability with more than 80% capacity retention after 1000 cycles. *Ex*-XRD and *Ex*-SEM reveal an outstanding chemical and physical stability of the Sn@CFC electrode over a ultralong cycling life.

(3) The self-nanocrystallization approach leads to the decrease of the size of the  $\text{SnP}_2\text{O}_7$  particles from 66 nm to 20 nm. This novel approach opens a new door to fabricate ultrasmall particles in an *in-situ* way with much low cost and high scalability. Moreover, owing to the unique structure, the homogenous dispersion of the nanoparticles remain active without particle aggregation after self-nanocrystallization.

(4) The self-nanocrystallization  $\text{SnP}_2\text{O}_7$  particles shorten the diffusion pathway of sodium ions and electrons, mitigating the stress originating from the sodiation/desodiation process. The N-doped carbon matrix not only enhances the electronic conductivity, but also keeps the self-nanocrystallization particles active during long-life cycles because of the strong bonding between  $\text{SnP}_2\text{O}_7$  particles and the carbon matrix. Thus, the  $\text{SnP}_2\text{O}_7$ @C anode delivers a high reversible capacity ( $403 \text{ mA h g}^{-1}$  at  $200 \text{ mA g}^{-1}$ ) and an excellent cycle stability over 4000 cycles at a high current density of  $1000 \text{ mA g}^{-1}$ .

(5) The SnS/Sb<sub>2</sub>S<sub>3</sub> heterostructure and the S, N co-doped carbon matrix can improve diffusion efficiency of the ions and electrons of SnS/Sb<sub>2</sub>S<sub>3</sub>@SNC, ensuring a good rate performance. The SnS/Sb<sub>2</sub>S<sub>3</sub>@SNC anode demonstrates excellent rate capability with a capacity of over 200 mA h g<sup>-1</sup> at a high current density of 5000 mA g<sup>-1</sup>.

(6) The porous can provide void space to mitigate the volume expansion upon cycling, guaranteeing long-term cycling stability. The SnS/Sb<sub>2</sub>S<sub>3</sub>@SNC electrode delivers a reversible capacity of 302 mA h g<sup>-1</sup> after 400 cycles.

(7) The DFT calculation and experimental studies have been integrated to fundamentally elucidate how the THF additive influences the solvation structure and its effect on the ion kinetics at the interface between the Zn electrode and the electrolyte. DFT calculation has confirmed the decrease in the solvation energy of the Zn hydration structure with the addition of THF. The formation of hydrogen bonds between H<sub>2</sub>O and THF plays a key role in reducing water activity to suppress the generation of H<sub>2</sub> and by-products.

(8) The Zn||Cu asymmetrical cell with ZnSO<sub>4</sub>/THF 5% electrolyte displayed a high average CE of 99.59% over 430 cycles, and the Zn symmetrical cell with the 2 M ZnSO<sub>4</sub>/THF 5% electrolyte achieved an ultralong cycling life of 1300 h at 0.5 mA cm<sup>-2</sup> and 0.5 mA h cm<sup>-2</sup> with the 10-fold improvement compared to baseline 2 M ZnSO<sub>4</sub> electrolyte. The MnO<sub>2</sub> cathode in Zn||MnO<sub>2</sub> full cell with ZnSO<sub>4</sub>/THF 5% electrolyte delivered a high reversible capacity of 225 mA h g<sup>-1</sup> after 250 cycles with a capacity retention of 97.56%.

## 5.2 Significance

In chapter 2, many synthesis methods have been developed. The projects in chapter 3 provide new strategies and insight to fabricate high performance nanomaterials in a facile and low-cost way for the energy storage field and holds the great potential to be applied in broader areas such as advanced manufacturing, catalyst, drug delivery, etc.

The work in chapter 4 demonstrates the high effectiveness of a simple organic molecule of THF in the improvement of AZIBs. We believe this original work provides a new strategy and insight to design novel aqueous electrolytes to consider the impact of the hydrogen bonds, which widely exist in water and organic molecules.

This dissertation will inspire the academic researcher further to find and work on such low-cost and facile materials/techniques that can help in the practical realization and applications of next-generation batteries. As a result, such a technique can pave the pathways for the commercialization to pacify the need for LSES, at a low cost.

## 5.3 Future work

To make this dissertation more comprehensive, some further work can be done, which can help for a better understanding of SIBs and AZIBs. Some proposed works are listed below:

- (1) To examine the practical application of the electrodes and electrolytes proposed in this dissertation, the pouch cells will be fabricated with capacity at Ah scale, because the pouch cells deliver high energy density in a smaller form factor. The flexibility of the pouch cells enables them to fit into a variety of shapes and sizes, making them highly versatile and adaptable for use in different applications. The

electrochemical performance of the pouch cells will be studied. The post-mortem analysis of the electrodes in the pouch cells will be examined to compare the differences between pouch and coin cells.

- (2) DFT calculations will be used to modify the composition of the materials. Some advanced materials will be studied by the DFT first, and then using the calculated figure guides the development of the electrode materials for SIBs and other battery technologies.
- (3) More additive will be screened in the aqueous electrolytes for AZIBs. The additive will include some salts that small amount of them can significantly improve the performance of the cells.

## Reference

- [1] J. Hansen, M. Sato, R. Ruedy, A. Lacis, and V. Oinas, "Global warming in the twenty-first century: An alternative scenario," *Proceedings of the National Academy of Sciences*, vol. 97, no. 18, pp. 9875-9880, 2000.
- [2] T. J. Crowley and R. A. Berner, "CO<sub>2</sub> and climate change," *Science*, vol. 292, no. 5518, pp. 870-872, 2001.
- [3] S. A. Montzka, E. J. Dlugokencky, and J. H. Butler, "Non-CO<sub>2</sub> greenhouse gases and climate change," *Nature*, vol. 476, no. 7358, pp. 43-50, 2011/08/01 2011.
- [4] P. Stott, "How climate change affects extreme weather events," *Science*, vol. 352, no. 6293, pp. 1517-1518, 2016.
- [5] F. Bosello, R. Roson, and R. S. Tol, "Economy-wide estimates of the implications of climate change: Sea level rise," *Environmental and Resource Economics*, vol. 37, pp. 549-571, 2007.
- [6] M. Romanello *et al.*, "The 2022 report of the countdown on health and climate change: health at the mercy of fossil fuels," *The Lancet*, vol. 400, no. 10363, pp. 1619-1654, 2022.
- [7] P. J. Gregory, J. S. Ingram, and M. Brklacich, "Climate change and food security," *Philosophical Transactions of the Royal Society B: Biological Sciences*, vol. 360, no. 1463, pp. 2139-2148, 2005.
- [8] R. S. J. Tol, "The economic effects of climate change," *Journal of economic perspectives*, vol. 23, no. 2, pp. 29-51, 2009.
- [9] R. Avtar *et al.*, "Exploring renewable energy resources using remote sensing and GIS—A review," *Resources*, vol. 8, no. 3, p. 149, 2019.

- [10] H. S. Hirsh, Y. Li, D. H. S. Tan, M. Zhang, E. Zhao, and Y. S. Meng, "Sodium-ion batteries paving the way for grid energy storage," *Advanced Energy Materials*, vol. 10, no. 32, p. 2001274, 2020.
- [11] K. M. Abraham, "How comparable are sodium-ion batteries to lithium-ion counterparts?," *ACS Energy Letters*, vol. 5, no. 11, pp. 3544-3547, 2020/11/13 2020.
- [12] C. Li, S. Jin, L. A. Archer, and L. F. Nazar, "Toward practical aqueous zinc-ion batteries for electrochemical energy storage," *Joule*, vol. 6, no. 8, pp. 1733-1738, 2022/08/17/ 2022.
- [13] Y. Geng *et al.*, "Electrolyte additive engineering for aqueous Zn ion batteries," *Energy Storage Materials*, vol. 51, pp. 733-755, 2022/10/01/ 2022.
- [14] S. Kuze *et al.*, "Development of a sodium ion secondary battery," *Sumitomo Kagaku*, vol. 2013, pp. 1-13, 2013.
- [15] R. J. Bones, D. A. Teagle, S. D. Brooker, and F. L. Cullen, "Development of a Ni, NiCl<sub>2</sub> positive electrode for a liquid sodium (ZEBRA) battery cell," *Journal of The Electrochemical Society*, vol. 136, no. 5, p. 1274, 1989/05/01 1989.
- [16] T. Oshima, M. Kajita, and A. Okuno, "Development of sodium-sulfur batteries," *International Journal of Applied Ceramic Technology*, vol. 1, no. 3, pp. 269-276, 2004.
- [17] G. H. Newman and L. P. Klemann, "Ambient temperature cycling of an Na - TiS<sub>2</sub> cell," *Journal of The Electrochemical Society*, vol. 127, no. 10, p. 2097, 1980/10/01 1980.



- [18] C. Delmas, C. Fouassier, and P. Hagemuller, "Structural classification and properties of the layered oxides," *Physica B+C*, vol. 99, no. 1, pp. 81-85, 1980/01/01/ 1980.
- [19] X. Liang, T.-Y. Yu, H.-H. Ryu, and Y.-K. Sun, "Hierarchical O3/P2 heterostructured cathode materials for advanced sodium-ion batteries," *Energy Storage Materials*, vol. 47, pp. 515-525, 2022/05/01/ 2022.
- [20] C. Delmas, J.-J. Braconnier, C. Fouassier, and P. Hagemuller, "Electrochemical intercalation of sodium in  $\text{Na}_x\text{CoO}_2$  bronzes," *Solid State Ionics*, vol. 3-4, pp. 165-169, 1981/08/01/ 1981.
- [21] N. Yabuuchi, K. Kubota, M. Dahbi, and S. Komaba, "Research development on sodium-ion batteries," *Chemical Reviews*, vol. 114, no. 23, pp. 11636-11682, 2014/12/10 2014.
- [22] Y. Liu, B. V. Merinov, and W. A. Goddard, "Origin of low sodium capacity in graphite and generally weak substrate binding of Na and Mg among alkali and alkaline earth metals," *Proceedings of the National Academy of Sciences*, vol. 113, no. 14, pp. 3735-3739, 2016.
- [23] Y. Okamoto, "Density functional theory calculations of alkali metal (Li, Na, and K) graphite intercalation compounds," *The Journal of Physical Chemistry C*, vol. 118, no. 1, pp. 16-19, 2014/01/09 2014.
- [24] D. A. Stevens and J. R. Dahn, "High capacity anode materials for rechargeable sodium-ion batteries," *Journal of The Electrochemical Society*, vol. 147, no. 4, p. 1271, 2000/04/01 2000.

- [25] X. Dou *et al.*, "Hard carbons for sodium-ion batteries: Structure, analysis, sustainability, and electrochemistry," *Materials Today*, vol. 23, pp. 87-104, 2019/03/01/ 2019.
- [26] J. Peng *et al.*, "Prussian blue analogues for sodium-ion batteries: Past, present, and future," *Advanced Materials*, vol. 34, no. 15, p. 2108384, 2022.
- [27] Q. Liu *et al.*, "The cathode choice for commercialization of sodium-ion batteries: Layered transition metal oxides versus prussian blue analogs," *Advanced Functional Materials*, vol. 30, no. 14, p. 1909530, 2020.
- [28] W. Wang *et al.*, "Reversible structural evolution of sodium-rich rhombohedral Prussian blue for sodium-ion batteries," *Nature Communications*, vol. 11, no. 1, p. 980, 2020/02/20 2020.
- [29] A. Paoletta *et al.*, "A review on hexacyanoferrate-based materials for energy storage and smart windows: challenges and perspectives," *Journal of Materials Chemistry A*, 10.1039/C7TA05121B vol. 5, no. 36, pp. 18919-18932, 2017.
- [30] B. Sayahpour, H. Hirsh, S. Parab, L. H. B. Nguyen, M. Zhang, and Y. S. Meng, "Perspective: Design of cathode materials for sustainable sodium-ion batteries," *MRS Energy & Sustainability*, vol. 9, no. 2, pp. 183-197, 2022/09/01 2022.
- [31] C. Vaalma, D. Buchholz, M. Weil, and S. Passerini, "A cost and resource analysis of sodium-ion batteries," *Nature Reviews Materials*, vol. 3, no. 4, p. 18013, 2018/03/13 2018.
- [32] J.-Y. Hwang, S.-T. Myung, and Y.-K. Sun, "Sodium-ion batteries: Present and future," *Chemical Society Reviews*, vol. 46, no. 12, pp. 3529-3614, 2017.

- [33] X. Xiang, K. Zhang, and J. Chen, "Recent advances and prospects of cathode materials for sodium-ion batteries," *Advanced Materials*, vol. 27, no. 36, pp. 5343-5364, 2015.
- [34] K. Chayambuka, G. Mulder, D. L. Danilov, and P. H. Notten, "Sodium - ion battery materials and electrochemical properties reviewed," *Advanced Energy Materials*, vol. 8, no. 16, p. 1800079, 2018.
- [35] M. Zhang, Y. Li, F. Wu, Y. Bai, and C. Wu, "Boost sodium-ion batteries to commercialization: Strategies to enhance initial Coulombic efficiency of hard carbon anode," *Nano Energy*, vol. 82, p. 105738, 2021.
- [36] L.-b. Tang *et al.*, "MoS<sub>2</sub>/SnS@C hollow hierarchical nanotubes as superior performance anode for sodium-ion batteries," *Nano Energy*, vol. 90, p. 106568, 2021.
- [37] K. Li *et al.*, "Evolution of the electrochemical interface in sodium ion batteries with ether electrolytes," *Nature communications*, vol. 10, no. 1, p. 725, Feb 13 2019.
- [38] D. Zhao *et al.*, "Alkali-induced 3D crinkled porous Ti<sub>3</sub>C<sub>2</sub> MXene architectures coupled with NiCoP bimetallic phosphide nanoparticles as anodes for high-performance sodium-ion batteries," *Energy & Environmental Science*, 10.1039/C9EE00308H vol. 12, no. 8, pp. 2422-2432, 2019.
- [39] S. Wang, Y. Fang, X. Wang, and X. W. Lou, "Hierarchical microboxes constructed by SnS nanoplates coated with nitrogen-doped carbon for efficient sodium storage," *Angewandte Chemie International Edition*, vol. 58, no. 3, pp. 760-763, 2019.

- [40] Y. Liu, B. Zhou, S. Liu, Q. Ma, and W.-H. Zhang, "Galvanic replacement synthesis of highly uniform Sb nanotubes: Reaction mechanism and enhanced sodium storage performance," *ACS Nano*, vol. 13, no. 5, pp. 5885-5892, 2019/05/28 2019.
- [41] J. Yan *et al.*, "Ultrahigh phosphorus doping of carbon for high-rate sodium ion batteries anode," *Advanced Energy Materials*, vol. 11, no. 21, p. 2003911, 2021.
- [42] Y. Wen *et al.*, "Expanded graphite as superior anode for sodium-ion batteries," *Nature Communications*, vol. 5, no. 1, p. 4033, 2014/06/04 2014.
- [43] F. Xie, Z. Xu, Z. Guo, and M.-M. Titirici, "Hard carbons for sodium-ion batteries and beyond," *Progress in Energy*, vol. 2, no. 4, p. 042002, 2020/09/18 2020.
- [44] B. Xiao, T. Rojo, and X. Li, "Hard carbon as sodium-ion battery anodes: Progress and challenges," *ChemSusChem*, vol. 12, no. 1, pp. 133-144, 2019.
- [45] H. Ying and W.-Q. Han, "Metallic Sn-based anode materials: Application in high-performance lithium-ion and sodium-ion batteries," *Advanced Science*, vol. 4, no. 11, p. 1700298, 2017.
- [46] B. Qu *et al.*, "Layered SnS<sub>2</sub>-reduced graphene oxide composite – A high-capacity, high-rate, and long-cycle life sodium-ion battery anode material," *Advanced Materials*, vol. 26, no. 23, pp. 3854-3859, 2014.
- [47] J. W. Wang, X. H. Liu, S. X. Mao, and J. Y. Huang, "Microstructural evolution of tin nanoparticles during in situ sodium insertion and extraction," *Nano Letters*, vol. 12, no. 11, pp. 5897-5902, 2012/11/14 2012.

- [48] N. Zhang, Y. Liu, Y. Lu, X. Han, F. Cheng, and J. Chen, "Spherical nano-Sb@C composite as a high-rate and ultra-stable anode material for sodium-ion batteries," *Nano Research*, vol. 8, pp. 3384-3393, 2015.
- [49] K. Chen, W. Chou, L. Liu, Y. Cui, P. Xue, and M. Jia, "Electrochemical sensors fabricated by electrospinning technology: An overview," *Sensors*, vol. 19, no. 17, p. 3676, 2019.
- [50] Y. Li *et al.*, "Developments of advanced electrospinning techniques: A critical review," *Advanced Materials Technologies*, vol. 6, no. 11, p. 2100410, 2021.
- [51] J. Xia *et al.*, "Free-standing SnS/C nanofiber anodes for ultralong cycle-life lithium-ion batteries and sodium-ion batteries," *Energy Storage Materials*, vol. 17, pp. 1-11, 2019/02/01/ 2019.
- [52] W. Luo, A. Calas, C. Tang, F. Li, L. Zhou, and L. Mai, "Ultralong Sb<sub>2</sub>Se<sub>3</sub> nanowire-based free-standing membrane anode for lithium/sodium ion batteries," *ACS Applied Materials & Interfaces*, vol. 8, no. 51, pp. 35219-35226, 2016/12/28 2016.
- [53] M. Yousaf *et al.*, "Core-shell FeSe<sub>2</sub>/C nanostructures embedded in a carbon framework as a free standing anode for a sodium ion battery," *Small*, vol. 16, no. 47, p. 2002200, 2020.
- [54] X. Ou *et al.*, "Fabrication of SnS<sub>2</sub>/Mn<sub>2</sub>SnS<sub>4</sub>/carbon heterostructures for sodium-ion batteries with high initial coulombic efficiency and cycling stability," *ACS Nano*, vol. 13, no. 3, pp. 3666-3676, 2019/03/26 2019.

- [55] J. Lin *et al.*, "Construction of  $\text{Sb}_2\text{S}_3@ \text{SnS}@ \text{C}$  tubular heterostructures as high-performance anode materials for sodium-ion batteries," *ACS Sustainable Chemistry & Engineering*, vol. 9, no. 33, pp. 11280-11289, 2021.
- [56] D. Yuan, Y. Dou, Y. Tian, D. Adekoya, L. Xu, and S. Zhang, "Robust pseudocapacitive sodium cation intercalation induced by cobalt vacancies at atomically thin  $\text{Co}_{1-x}\text{Se}_2/\text{graphene}$  heterostructure for sodium-ion batteries," *Angewandte Chemie International Edition*, vol. 60, no. 34, pp. 18830-18837, 2021.
- [57] H. Yang *et al.*, "Reducing water activity by zeolite molecular sieve membrane for long-life rechargeable zinc battery," *Advanced Materials*, vol. 33, no. 38, p. 2102415, 2021.
- [58] L. Ma *et al.*, "Hydrogen-free and dendrite-free all-solid-state Zn-ion batteries," *Advanced Materials*, vol. 32, no. 14, p. 1908121, 2020.
- [59] F. Wang *et al.*, "Highly reversible zinc metal anode for aqueous batteries," *Nature Materials*, vol. 17, no. 6, pp. 543-549, 2018/06/01 2018.
- [60] L. Cao *et al.*, "Fluorinated interphase enables reversible aqueous zinc battery chemistries," *Nature Nanotechnology*, vol. 16, no. 8, pp. 902-910, 2021/08/01 2021.
- [61] W. Sun *et al.*, "A rechargeable zinc-air battery based on zinc peroxide chemistry," *Science*, vol. 371, no. 6524, pp. 46-51, 2021.
- [62] Z. Chen *et al.*, "Zinc/selenium conversion battery: a system highly compatible with both organic and aqueous electrolytes," *Energy & Environmental Science*, 10.1039/D0EE02999H vol. 14, no. 4, pp. 2441-2450, 2021.

- [63] W. He *et al.*, "Achieving high pseudocapacitance anode by an in situ nanocrystallization strategy for ultrastable sodium-ion batteries," *ACS Applied Materials & Interfaces*, vol. 13, no. 19, pp. 22577-22585, 2021/05/19 2021.
- [64] W. He *et al.*, "High-mass-loading Sn-based anode boosted by pseudocapacitance for long-life sodium-ion batteries," *Chemical Engineering Journal*, vol. 414, p. 128638, 2021/06/15/ 2021.
- [65] C. Xu, B. Li, H. Du, and F. Kang, "Energetic zinc ion chemistry: The rechargeable zinc ion battery," *Angewandte Chemie International Edition*, vol. 51, no. 4, pp. 933-935, 2012.
- [66] W. Sun *et al.*, "Zn/MnO<sub>2</sub> battery chemistry with H<sup>+</sup> and Zn<sup>2+</sup> coinsertion," *Journal of the American Chemical Society*, vol. 139, no. 29, pp. 9775-9778, 2017/07/26 2017.
- [67] F. Wan, L. Zhang, X. Dai, X. Wang, Z. Niu, and J. Chen, "Aqueous rechargeable zinc/sodium vanadate batteries with enhanced performance from simultaneous insertion of dual carriers," *Nature Communications*, vol. 9, no. 1, p. 1656, 2018/04/25 2018.
- [68] Z. Wang *et al.*, "A MOF-based single-ion Zn<sup>2+</sup> solid electrolyte leading to dendrite-free rechargeable Zn batteries," *Nano Energy*, vol. 56, pp. 92-99, 2019/02/01/ 2019.
- [69] H. Yang *et al.*, "Constructing a super-saturated electrolyte front surface for stable rechargeable aqueous zinc batteries," *Angewandte Chemie International Edition*, vol. 59, no. 24, pp. 9377-9381, 2020.

- [70] W. He *et al.*, "Decreasing water activity using the tetrahydrofuran electrolyte additive for highly reversible aqueous zinc metal batteries," *ACS Applied Materials & Interfaces*, vol. 15, no. 5, pp. 6647-6656, 2023/02/08 2023.
- [71] N. Zhang, X. Chen, M. Yu, Z. Niu, F. Cheng, and J. Chen, "Materials chemistry for rechargeable zinc-ion batteries," *Chemical Society Reviews*, 10.1039/C9CS00349E vol. 49, no. 13, pp. 4203-4219, 2020.
- [72] X. Gao *et al.*, "H<sup>+</sup>-insertion boosted  $\alpha$ -MnO<sub>2</sub> for an aqueous Zn-ion battery," *Small*, vol. 16, no. 5, p. 1905842, 2020.
- [73] W. Zhang *et al.*, "The current developments and perspectives of V<sub>2</sub>O<sub>5</sub> as cathode for rechargeable aqueous zinc-ion batteries," *Energy Technology*, vol. 9, no. 2, p. 2000789, 2021.
- [74] J. Huang *et al.*, "Polyaniline-intercalated manganese dioxide nanolayers as a high-performance cathode material for an aqueous zinc-ion battery," *Nature communications*, vol. 9, no. 1, p. 2906, 2018.
- [75] B. Yong, D. Ma, Y. Wang, H. Mi, C. He, and P. Zhang, "Understanding the design principles of advanced aqueous zinc-ion battery cathodes: From transport kinetics to structural engineering, and future perspectives," *Advanced Energy Materials*, vol. 10, no. 45, p. 2002354, 2020.
- [76] C. Liu *et al.*, "Liquid alloy interlayer for aqueous zinc-ion battery," *ACS Energy Letters*, vol. 6, no. 2, pp. 675-683, 2021/02/12 2021.
- [77] Z. Cao *et al.*, "Eliminating Zn dendrites by commercial cyanoacrylate adhesive for zinc ion battery," *Energy Storage Materials*, vol. 36, pp. 132-138, 2021/04/01/ 2021.



- [78] J. Zhou *et al.*, "Ultrathin surface coating of nitrogen-doped graphene enables stable zinc anodes for aqueous zinc-ion batteries," *Advanced Materials*, vol. 33, no. 33, p. 2101649, 2021.
- [79] M. Wang, F. Zhang, C.-S. Lee, and Y. Tang, "Low-cost metallic anode materials for high performance rechargeable batteries," *Advanced Energy Materials*, vol. 7, no. 23, p. 1700536, 2017.
- [80] H. He *et al.*, "Engineering interfacial layers to enable Zn metal anodes for aqueous zinc-ion batteries," *Energy Storage Materials*, vol. 43, pp. 317-336, 2021.
- [81] Z. Cao, P. Zhuang, X. Zhang, M. Ye, J. Shen, and P. M. Ajayan, "Strategies for dendrite-free anode in aqueous rechargeable zinc ion batteries," *Advanced Energy Materials*, vol. 10, no. 30, p. 2001599, 2020.
- [82] W. Du, E. H. Ang, Y. Yang, Y. Zhang, M. Ye, and C. C. Li, "Challenges in the material and structural design of zinc anode towards high-performance aqueous zinc-ion batteries," *Energy & Environmental Science*, 10.1039/D0EE02079F vol. 13, no. 10, pp. 3330-3360, 2020.
- [83] M. Liu, J. Cai, H. Ao, Z. Hou, Y. Zhu, and Y. Qian, "NaTi<sub>2</sub>(PO<sub>4</sub>)<sub>3</sub> solid-state electrolyte protection layer on Zn metal anode for superior long-life aqueous zinc-ion batteries," *Advanced Functional Materials*, vol. 30, no. 50, p. 2004885, 2020.
- [84] Z. Zhao *et al.*, "Long-life and deeply rechargeable aqueous Zn anodes enabled by a multifunctional brightener-inspired interphase," *Energy & Environmental Science*, vol. 12, no. 6, pp. 1938-1949, 2019.

- [85] Y. Jin *et al.*, "Stabilizing zinc anode reactions by polyethylene oxide polymer in mild aqueous electrolytes," *Advanced Functional Materials*, vol. 30, no. 43, p. 2003932, 2020.
- [86] S. Zhou *et al.*, "Anti-corrosive and Zn-ion-regulating composite interlayer enabling long-life Zn metal anodes," *Advanced Functional Materials*, vol. 31, no. 46, p. 2104361, 2021.
- [87] N. Zhang, S. Huang, Z. Yuan, J. Zhu, Z. Zhao, and Z. Niu, "Direct self-assembly of MXene on Zn anodes for dendrite-free aqueous zinc-ion batteries," *Angewandte Chemie International Edition*, vol. 60, no. 6, pp. 2861-2865, 2021.
- [88] X. Zhou *et al.*, "Driving the interfacial ion-transfer kinetics by mesoporous TiO<sub>2</sub> spheres for high-performance aqueous Zn-ion batteries," *ACS Applied Materials & Interfaces*, vol. 13, no. 7, pp. 8181-8190, 2021.
- [89] P. Liang *et al.*, "Highly reversible Zn anode enabled by controllable formation of nucleation sites for Zn-based batteries," *Advanced Functional Materials*, vol. 30, no. 13, p. 1908528, 2020.
- [90] S. Bhoyate, S. Mhin, J.-e. Jeon, K. Park, J. Kim, and W. Choi, "Stable and high-energy-density Zn-ion rechargeable batteries based on a MoS<sub>2</sub>-coated Zn anode," *ACS applied materials & interfaces*, vol. 12, no. 24, pp. 27249-27257, 2020.
- [91] C. Zhang *et al.*, "The electrolyte comprising more robust water and superhalides transforms Zn-metal anode reversibly and dendrite-free," *Carbon Energy*, vol. 3, no. 2, pp. 339-348, 2021.

- [92] Q. Zhang *et al.*, "Modulating electrolyte structure for ultralow temperature aqueous zinc batteries," *Nature Communications*, vol. 11, no. 1, p. 4463, 2020/09/08 2020.
- [93] S. Cai *et al.*, "Water–salt oligomers enable supersoluble electrolytes for high-performance aqueous batteries," *Advanced Materials*, vol. 33, no. 13, p. 2007470, 2021.
- [94] J. Hao *et al.*, "Boosting zinc electrode reversibility in aqueous electrolytes by using low-cost antisolvents," *Angewandte Chemie International Edition*, vol. 60, no. 13, pp. 7366-7375, 2021.
- [95] L. Cao *et al.*, "Solvation structure design for aqueous Zn metal batteries," *Journal of the American Chemical Society*, vol. 142, no. 51, pp. 21404-21409, 2020.
- [96] S. Liu *et al.*, "Tuning the electrolyte solvation structure to suppress cathode dissolution, water reactivity, and Zn dendrite growth in zinc-ion batteries," *Advanced Functional Materials*, vol. 31, no. 38, p. 2104281, 2021.
- [97] Q. Zhang *et al.*, "Designing anion-type water-free Zn<sup>2+</sup> solvation structure for robust Zn metal anode," *Angewandte Chemie*, vol. 133, no. 43, pp. 23545-23552, 2021.
- [98] P. Sun *et al.*, "Simultaneous regulation on solvation shell and electrode interface for dendrite-free Zn ion batteries achieved by a low-cost glucose additive," *Angewandte Chemie International Edition*, vol. 60, no. 33, pp. 18247-18255, 2021.

- [99] J. Shi *et al.*, "Ultra-high coulombic efficiency and long-life aqueous Zn anodes enabled by electrolyte additive of acetonitrile," *Electrochimica Acta*, vol. 358, p. 136937, 2020.
- [100] W. Xu *et al.*, "Diethyl ether as self-healing electrolyte additive enabled long-life rechargeable aqueous zinc ion batteries," *Nano Energy*, vol. 62, pp. 275-281, 2019/08/01/ 2019.
- [101] G. Kresse and J. Hafner, "Ab initio molecular dynamics for liquid metals," *Physical Review B*, vol. 47, no. 1, pp. 558-561, 01/01/ 1993.
- [102] G. Kresse and J. Furthmüller, "Efficiency of ab-initio total energy calculations for metals and semiconductors using a plane-wave basis set," *Computational Materials Science*, vol. 6, no. 1, pp. 15-50, 1996/07/01/ 1996.
- [103] J. P. Perdew *et al.*, "Atoms, molecules, solids, and surfaces: Applications of the generalized gradient approximation for exchange and correlation," *Physical Review B*, vol. 46, no. 11, pp. 6671-6687, 09/15/ 1992.
- [104] H. J. Monkhorst and J. D. Pack, "Special points for Brillouin-zone integrations," *Physical Review B*, vol. 13, no. 12, pp. 5188-5192, 06/15/ 1976.
- [105] Z. Liu *et al.*, "Dendrite-free lithium based on lessons learned from lithium and magnesium electrodeposition morphology simulations," *Cell Reports Physical Science*, vol. 2, no. 1, p. 100294, 2021/01/20/ 2021.
- [106] Y. Liu, N. Zhang, L. Jiao, and J. Chen, "Tin nanodots encapsulated in porous nitrogen-doped carbon nanofibers as a free-standing anode for advanced sodium-ion batteries," *Advanced materials*, vol. 27, no. 42, pp. 6702-7, Nov 2015.

- [107] T. Palaniselvam *et al.*, "Sodium storage and electrode dynamics of tin-carbon composite electrodes from bulk precursors for sodium-ion batteries," *Advanced Functional Materials*, vol. 29, no. 18, p. 1900790, 2019.
- [108] Y. Wang *et al.*, "Tin sulfide nanoparticles embedded in sulfur and nitrogen dual-doped mesoporous carbon fibers as high-performance anodes with battery-capacitive sodium storage," *Energy Storage Materials*, vol. 18, pp. 366-374, 2019.
- [109] S. Chen, Z. Ao, B. Sun, X. Xie, and G. Wang, "Porous carbon nanocages encapsulated with tin nanoparticles for high performance sodium-ion batteries," *Energy Storage Materials*, vol. 5, pp. 180-190, 2016/10/01/ 2016.
- [110] X. Ren *et al.*, "Sn-C bonding riveted SnSe nanoplates vertically grown on nitrogen-doped carbon nanobelts for high-performance sodium-ion battery anodes," *Nano Energy*, vol. 54, pp. 322-330, 2018/12/01/ 2018.
- [111] W. Ma, K. Yin, H. Gao, J. Niu, Z. Peng, and Z. Zhang, "Alloying boosting superior sodium storage performance in nanoporous tin-antimony alloy anode for sodium ion batteries," *Nano Energy*, vol. 54, pp. 349-359, 2018/12/01/ 2018.
- [112] W. Song *et al.*, "Sn@C evolution from yolk-shell to core-shell in carbon nanofibers with suppressed degradation of lithium storage," *Energy Storage Materials*, vol. 18, pp. 229-237, 2019/03/01/ 2019.
- [113] D. Lin *et al.*, "A high tap density secondary silicon particle anode fabricated by scalable mechanical pressing for lithium-ion batteries," *Energy & Environmental Science*, 10.1039/C5EE01363A vol. 8, no. 8, pp. 2371-2376, 2015.
- [114] L. Hu *et al.*, "Lithium-ion textile batteries with large areal mass loading," *Advanced Energy Materials*, vol. 1, no. 6, pp. 1012-1017, 2011.

- [115] R. Yi, J. Zai, F. Dai, M. L. Gordin, and D. Wang, "Dual conductive network-enabled graphene/Si-C composite anode with high areal capacity for lithium-ion batteries," *Nano Energy*, vol. 6, pp. 211-218, 2014/05/01/ 2014.
- [116] T. Wang, D. Legut, Y. Fan, J. Qin, X. Li, and Q. Zhang, "Building fast diffusion channel by constructing metal sulfide/metal selenide heterostructures for high-performance sodium ion batteries anode," *Nano Letters*, vol. 20, no. 8, pp. 6199-6205, 2020/08/12 2020.
- [117] G. Fang *et al.*, "Observation of pseudocapacitive effect and fast ion diffusion in bimetallic sulfides as an advanced sodium-ion battery anode," *Advanced Energy Materials*, vol. 8, no. 19, p. 1703155, 2018.
- [118] Y. Jiang *et al.*, "Sandwich-like SnS<sub>2</sub>/graphene/SnS<sub>2</sub> with expanded interlayer distance as high-rate lithium/sodium-ion battery anode materials," *ACS Nano*, vol. 13, no. 8, pp. 9100-9111, 2019/08/27 2019.
- [119] Z. Yuan, L. Wang, D. Li, J. Cao, and W. Han, "Carbon-reinforced Nb<sub>2</sub>CT<sub>x</sub> MXene/MoS<sub>2</sub> nanosheets as a superior rate and high-capacity anode for sodium-ion batteries," *ACS nano*, vol. 15, no. 4, pp. 7439-7450, 2021.
- [120] Y. Xu *et al.*, "Uniform nano-Sn/C composite anodes for lithium ion batteries," *Nano Letters*, vol. 13, no. 2, pp. 470-474, 2013/02/13 2013.
- [121] L. Cao, X. Gao, B. Zhang, X. Ou, J. Zhang, and W.-B. Luo, "Bimetallic sulfide Sb<sub>2</sub>S<sub>3</sub>@FeS<sub>2</sub> hollow nanorods as high-performance anode materials for sodium-ion batteries," *ACS Nano*, vol. 14, no. 3, pp. 3610-3620, 2020/03/24 2020.
- [122] Y. Yang *et al.*, "Ionic-liquid-bifunctional wrapping of ultrafine SnO<sub>2</sub> nanocrystals into N-doped graphene networks: high pseudocapacitive sodium storage and high-

- performance sodium-ion full cells," *Nanoscale*, 10.1039/C9NR02542A vol. 11, no. 31, pp. 14616-14624, 2019.
- [123] Y. Zheng, T. Zhou, C. Zhang, J. Mao, H. Liu, and Z. Guo, "Boosted charge transfer in SnS/SnO<sub>2</sub> heterostructures: toward high rate capability for sodium-ion batteries," *Angewandte Chemie International Edition*, vol. 55, no. 10, pp. 3408-3413, 2016.
- [124] M. Wang *et al.*, "SnO<sub>2</sub> nanoflake arrays coated with polypyrrole on a carbon cloth as flexible anodes for sodium-ion batteries," *ACS Applied Materials & Interfaces*, vol. 11, no. 27, pp. 24198-24204, 2019/07/10 2019.
- [125] J. Chen *et al.*, "Intercalation of Bi nanoparticles into graphite results in an ultra-fast and ultra-stable anode material for sodium-ion batteries," *Energy & Environmental Science*, 10.1039/C7EE03016A vol. 11, no. 5, pp. 1218-1225, 2018.
- [126] Z. Liu *et al.*, "Highly reversible sodiation/desodiation from a carbon-sandwiched SnS<sub>2</sub> nanosheet anode for sodium ion batteries," *Nano Letters*, vol. 20, no. 5, pp. 3844-3851, 2020/05/13 2020.
- [127] L. Ji *et al.*, "Controlling SEI formation on SnSb-Porous carbon nanofibers for improved Na ion storage," *Advanced Materials*, vol. 26, no. 18, pp. 2901-2908, 2014.
- [128] K. Dai, H. Zhao, Z. Wang, X. Song, V. Battaglia, and G. Liu, "Toward high specific capacity and high cycling stability of pure tin nanoparticles with conductive polymer binder for sodium ion batteries," *Journal of Power Sources*, vol. 263, pp. 276-279, 2014/10/01/ 2014.

- [129] J. Ming, H. Ming, W.-J. Kwak, C. Shin, J. Zheng, and Y.-K. Sun, "The binder effect on an oxide-based anode in lithium and sodium-ion battery applications: the fastest way to ultrahigh performance," *Chemical Communications*, 10.1039/C4CC02657H vol. 50, no. 87, pp. 13307-13310, 2014.
- [130] M. Sheng, F. Zhang, B. Ji, X. Tong, and Y. Tang, "A novel tin-graphite dual-ion battery based on sodium-ion electrolyte with high energy density," *Advanced Energy Materials*, vol. 7, no. 7, p. 1601963, 2017.
- [131] S. Rubio *et al.*, "Superior electrochemical performance of TiO<sub>2</sub> sodium-ion battery anodes in diglyme-based electrolyte solution," *Journal of Power Sources*, vol. 432, pp. 82-91, 2019/08/31/ 2019.
- [132] C. Wang, H. Wu, Z. Chen, M. T. McDowell, Y. Cui, and Z. Bao, "Self-healing chemistry enables the stable operation of silicon microparticle anodes for high-energy lithium-ion batteries," *Nature Chemistry*, vol. 5, no. 12, pp. 1042-1048, 2013/12/01 2013.
- [133] Y. Fang, X.-Y. Yu, and X. W. Lou, "Formation of polypyrrole-coated Sb<sub>2</sub>Se<sub>3</sub> microclips with enhanced sodium-storage properties," *Angewandte Chemie International Edition*, vol. 57, no. 31, pp. 9859-9863, 2018.
- [134] P. Simon, Y. Gogotsi, and B. Dunn, "Where do batteries end and supercapacitors begin?," *Science*, vol. 343, no. 6176, pp. 1210-1211, 2014.
- [135] S. Lou *et al.*, "Superior performance of ordered macroporous TiNb<sub>2</sub>O<sub>7</sub> anodes for lithium ion batteries: Understanding from the structural and pseudocapacitive insights on achieving high rate capability," *Nano Energy*, vol. 34, pp. 15-25, 2017/04/01/ 2017.



- [136] H. Xie *et al.*, " $\beta$ -SnSb for sodium ion battery anodes: Phase transformations responsible for enhanced cycling stability revealed by in situ TEM," *ACS Energy Letters*, vol. 3, no. 7, pp. 1670-1676, 2018/07/13 2018.
- [137] M. Xu *et al.*, "Rambutan-like hybrid hollow spheres of carbon confined  $\text{Co}_3\text{O}_4$  nanoparticles as advanced anode materials for sodium-ion batteries," *Advanced Functional Materials*, vol. 29, no. 6, p. 1807377, 2019.
- [138] Y. Li and J. Li, "Carbon-coated macroporous  $\text{Sn}_2\text{P}_2\text{O}_7$  as anode materials for Li-ion battery," *The Journal of Physical Chemistry C*, vol. 112, no. 36, pp. 14216-14219, 2008/09/11 2008.
- [139] P. S. Attidekou, P. A. Connor, P. Wormald, D. P. Tunstall, S. M. Francis, and J. T. S. Irvine, "Solid state NMR studies of phosphate/tin matrix formed on electrochemical insertion into  $\text{SnP}_2\text{O}_7$ ," *Solid State Ionics*, vol. 175, no. 1, pp. 185-190, 2004/11/30/ 2004.
- [140] W. He, H. Tian, S. Zhang, H. Ying, Z. Meng, and W. Han, "Scalable synthesis of Si/C anode enhanced by  $\text{FeSi}_x$  nanoparticles from low-cost ferrosilicon for lithium-ion batteries," *Journal of Power Sources*, vol. 353, pp. 270-276, 2017.
- [141] W. Shuang *et al.*, "Nitrogen-doped carbon shell-confined  $\text{Ni}_3\text{S}_2$  composite nanosheets derived from Ni-MOF for high performance sodium-ion battery anodes," *Nano Energy*, vol. 62, pp. 154-163, 2019/08/01/ 2019.
- [142] H. Shuai *et al.*, "Electrochemically exfoliated phosphorene-graphene hybrid for sodium-ion batteries," *Small Methods*, vol. 3, no. 2, p. 1800328, 2019.
- [143] Y. Liu, Y. Fang, Z. Zhao, C. Yuan, and X. W. Lou, "A ternary  $\text{Fe}_{1-x}\text{S}$ @porous carbon nanowires/reduced graphene oxide hybrid film electrode with superior

- volumetric and gravimetric capacities for flexible sodium ion batteries," *Advanced Energy Materials*, vol. 9, no. 9, p. 1803052, 2019.
- [144] H. Qiu *et al.*, "SnO<sub>2</sub> nanoparticles anchored on carbon foam as a freestanding anode for high performance potassium-ion batteries," *Energy & Environmental Science*, 10.1039/C9EE03682B vol. 13, no. 2, pp. 571-578, 2020.
- [145] S. Mu, Q. Liu, P. Kidkhunthod, X. Zhou, W. Wang, and Y. Tang, "Molecular grafting towards high-fraction active nanodots implanted in N-doped carbon for sodium dual-ion batteries," *National Science Review*, 2020.
- [146] J. Pan *et al.*, "SnP<sub>2</sub>O<sub>7</sub> covered carbon nanosheets as a long-life and high-rate anode material for sodium-ion batteries," *Advanced Functional Materials*, vol. 28, no. 43, p. 1804672, 2018.
- [147] L. Pan, H. Huang, M. Zhong, and M. Niederberger, "Hydrogel-derived foams of nitrogen-doped carbon loaded with Sn nanodots for high-mass-loading Na-ion storage," *Energy Storage Materials*, vol. 16, pp. 519-526, 2019/01/01/ 2019.
- [148] W. Chen *et al.*, "High-performance flexible freestanding anode with hierarchical 3D carbon-networks/Fe<sub>7</sub>S<sub>8</sub>/graphene for applicable sodium-ion batteries," *Advanced Materials*, vol. 31, no. 8, p. 1806664, 2019.
- [149] J. Zhou *et al.*, "Few-layer bismuthene with anisotropic expansion for high-areal-capacity sodium-ion batteries," *Advanced Materials*, vol. 31, no. 12, p. 1807874, 2019.
- [150] A. Chojnacka, X. Pan, P. Jeżowski, and F. Béguin, "High performance hybrid sodium-ion capacitor with tin phosphide used as battery-type negative electrode," *Energy Storage Materials*, vol. 22, pp. 200-206, 2019/11/01/ 2019.

- [151] X. Ren *et al.*, "Tailored plum pudding-like Co<sub>2</sub>P/Sn encapsulated with carbon nanobox shell as superior anode materials for high-performance sodium-ion capacitors," *Advanced Energy Materials*, vol. 9, no. 16, p. 1900091, 2019.
- [152] J. Qin *et al.*, "Graphene networks anchored with Sn@graphene as lithium ion battery anode," *ACS Nano*, vol. 8, no. 2, pp. 1728-1738, 2014/02/25 2014.
- [153] Y. Zhang *et al.*, "Graphene-encapsulated CuP<sub>2</sub>: A Promising anode material with high reversible capacity and superior rate-performance for sodium-ion batteries," *Nano Letters*, vol. 19, no. 4, pp. 2575-2582, 2019/04/10 2019.
- [154] Y. Zheng, T. Zhou, C. Zhang, J. Mao, H. Liu, and Z. Guo, "Boosted charge transfer in SnS/SnO<sub>2</sub> heterostructures: toward high rate capability for sodium-ion batteries," *Angewandte Chemie*, vol. 128, no. 10, pp. 3469-3474, 2016.
- [155] S. Yao *et al.*, "Ultrathin Sb<sub>2</sub>S<sub>3</sub> nanosheet anodes for exceptional pseudocapacitive contribution to multi-battery charge storage," *Energy Storage Materials*, vol. 20, pp. 36-45, 2019/07/01/ 2019.
- [156] J. Pan *et al.*, "Layered-structure SbPO<sub>4</sub>/reduced graphene oxide: An advanced anode material for sodium ion batteries," *ACS Nano*, vol. 12, no. 12, pp. 12869-12878, 2018/12/26 2018.
- [157] X. Fan *et al.*, "Superior stable self-healing SnP<sub>3</sub> anode for sodium-ion batteries," *Advanced Energy Materials*, vol. 5, no. 18, p. 1500174, 2015.
- [158] F. Zhang, J. Zhu, D. Zhang, U. Schwingenschlögl, and H. N. Alshareef, "Two-dimensional SnO anodes with a tunable number of atomic layers for sodium ion batteries," *Nano Letters*, vol. 17, no. 2, pp. 1302-1311, 2017/02/08 2017.

- [159] E. Pan *et al.*, "Conformal hollow carbon sphere coated on Sn<sub>4</sub>P<sub>3</sub> microspheres as high-rate and cycle-stable anode materials with superior sodium storage capability," *ACS Applied Energy Materials*, vol. 2, no. 3, pp. 1756-1764, 2019/03/25 2019.
- [160] L. Ran *et al.*, "Biomimetic Sn<sub>4</sub>P<sub>3</sub> anchored on carbon nanotubes as an anode for high-performance sodium-ion batteries," *ACS Nano*, vol. 14, no. 7, pp. 8826-8837, 2020/07/28 2020.
- [161] S. Li, Z. Zhao, C. Li, Z. Liu, and D. Li, "SnS<sub>2</sub>@C hollow nanospheres with robust structural stability as high-performance anodes for sodium ion batteries," *Nano-Micro Letters*, vol. 11, no. 1, p. 14, 2019/02/21 2019.
- [162] D.-c. Zuo, S.-c. Song, C.-s. An, L.-b. Tang, Z.-j. He, and J.-c. Zheng, "Synthesis of sandwich-like structured Sn/SnO<sub>x</sub>@MXene composite through in-situ growth for highly reversible lithium storage," *Nano Energy*, vol. 62, pp. 401-409, 2019/08/01/ 2019.
- [163] S. Wang *et al.*, "SnS<sub>2</sub>/Sb<sub>2</sub>S<sub>3</sub> heterostructures anchored on reduced graphene oxide nanosheets with superior rate capability for sodium-ion batteries," *Chemistry – A European Journal*, vol. 24, no. 15, pp. 3873-3881, 2018/03/12 2018.
- [164] Y. Liu, C. Yang, Q. Zhang, and M. Liu, "Recent progress in the design of metal sulfides as anode materials for sodium ion batteries," *Energy Storage Materials*, vol. 22, pp. 66-95, 2019.
- [165] J. Wang, X. Yue, Z. Xie, A. Abudula, and G. Guan, "MOFs-derived transition metal sulfide composites for advanced sodium ion batteries," *Energy Storage Materials*, vol. 41, pp. 404-426, 2021.

- [166] J. Shi *et al.*, "NS co-doped C@SnS nanoflakes/graphene composite as advanced anode for sodium-ion batteries," *Chemical Engineering Journal*, vol. 353, pp. 606-614, 2018.
- [167] F. Xie, L. Zhang, Q. Gu, D. Chao, M. Jaroniec, and S.-Z. Qiao, "Multi-shell hollow structured  $\text{Sb}_2\text{S}_3$  for sodium-ion batteries with enhanced energy density," *Nano Energy*, vol. 60, pp. 591-599, 2019/06/01/ 2019.
- [168] X. M. Lin *et al.*, "Synthesis and operando sodiation mechanistic study of nitrogen-doped porous carbon coated bimetallic sulfide hollow nanocubes as advanced sodium ion battery anode," *Advanced Energy Materials*, vol. 9, no. 40, p. 1902312, 2019.
- [169] W. Zhang *et al.*, "A novel chitosan–vanadium-titanium-magnetite composite as a superior adsorbent for organic dyes in wastewater," *Environment International*, vol. 142, p. 105798, 2020/09/01/ 2020.
- [170] W. He, H. Tian, F. Xin, and W. Han, "Scalable fabrication of micro-sized bulk porous Si from Fe–Si alloy as a high performance anode for lithium-ion batteries," *Journal of Materials Chemistry A*, 10.1039/C5TA04857E vol. 3, no. 35, pp. 17956-17962, 2015.
- [171] J. Sheng, L. Yang, Y.-E. Zhu, F. Li, Y. Zhang, and Z. Zhou, "Oriented SnS nanoflakes bound on S-doped N-rich carbon nanosheets with a rapid pseudocapacitive response as high-rate anodes for sodium-ion batteries," *Journal of Materials Chemistry A*, 10.1039/C7TA06577A vol. 5, no. 37, pp. 19745-19751, 2017.

- [172] J. Ru *et al.*, "Covalent assembly of MoS<sub>2</sub> nanosheets with SnS nanodots as linkages for lithium/sodium-ion batteries," *Angewandte Chemie International Edition*, vol. 59, no. 34, pp. 14621-14627, 2020.
- [173] L. Fu *et al.*, "Lithium pre-cycling induced fast kinetics of commercial Sb<sub>2</sub>S<sub>3</sub> anode for advanced sodium storage," *Energy & Environmental Materials*, vol. 2, no. 3, pp. 209-215, 2019.
- [174] M. Wang *et al.*, "Stable lithium sulfur battery based on in situ electrocatalytically formed Li<sub>2</sub>S on metallic MoS<sub>2</sub>-carbon cloth support," *Small Methods*, vol. 4, no. 9, p. 2000353, 2020.
- [175] T. D. Pham, A. Bin Faheem, and K.-K. Lee, "Design of a LiF-rich solid electrolyte interphase layer through highly concentrated LiFSI-THF electrolyte for stable lithium metal batteries," *Small*, vol. 17, no. 46, p. 2103375, 2021.
- [176] T. Takamuku, A. Nakamizo, M. Tabata, K. Yoshida, T. Yamaguchi, and T. Otomo, "Large-angle X-ray scattering, small-angle neutron scattering, and NMR relaxation studies on mixing states of 1,4-dioxane-water, 1,3-dioxane-water, and tetrahydrofuran-water mixtures," *Journal of Molecular Liquids*, vol. 103-104, pp. 143-159, 2003/03/01/ 2003.
- [177] V. Gutmann and V. Gutmann, *The donor-acceptor approach to molecular interactions*. Springer, 1978.
- [178] B. J. Mhin, S. Lee, S. J. Cho, K. Lee, and K. S. Kim, "Zn(H<sub>2</sub>O)<sup>2+</sup><sub>6</sub> is very stable among aqua-Zn(II) ions," *Chemical Physics Letters*, vol. 197, no. 1, pp. 77-80, 1992/09/04/ 1992.

- [179] Y. Dong *et al.*, "Non-concentrated aqueous electrolytes with organic solvent additives for stable zinc batteries," *Chemical Science*, 10.1039/D0SC06734B vol. 12, no. 16, pp. 5843-5852, 2021.
- [180] S. De, S. M. Ali, A. Ali, and V. G. Gaikar, "Micro-solvation of the  $Zn^{2+}$  ion—a case study," *Physical Chemistry Chemical Physics*, 10.1039/B902422K vol. 11, no. 37, pp. 8285-8294, 2009.
- [181] R. Pathak *et al.*, "Fluorinated hybrid solid-electrolyte-interphase for dendrite-free lithium deposition," *Nature Communications*, vol. 11, no. 1, p. 93, 2020/01/03 2020.
- [182] K. Chen *et al.*, "A copper-clad lithiophilic current collector for dendrite-free lithium metal anodes," *Journal of Materials Chemistry A*, 10.1039/C9TA11237E vol. 8, no. 4, pp. 1911-1919, 2020.
- [183] Z. Xing *et al.*, "Highly reversible zinc-ion battery enabled by suppressing vanadium dissolution through inorganic  $Zn^{2+}$  conductor electrolyte," *Nano Energy*, vol. 90, p. 106621, 2021/12/01/ 2021.
- [184] Y. Wang, Y. Fan, D. Liao, Y. Wu, Y. Yu, and C. Hu, "Highly  $Zn^{2+}$ -conductive and robust modified montmorillonite protective layer of electrodes toward high-performance rechargeable zinc-ion batteries," *Energy Storage Materials*, vol. 51, pp. 212-222, 2022/10/01/ 2022.
- [185] H. Yan, S. Li, Y. Nan, S. Yang, and B. Li, "Ultrafast zinc-ion-conductor interface toward high-rate and stable zinc metal batteries," *Advanced Energy Materials*, vol. 11, no. 18, p. 2100186, 2021.

- [186] J. H. Park *et al.*, "Self-assembling films of covalent organic frameworks enable long-term, efficient cycling of zinc-ion batteries," *Advanced Materials*, vol. 33, no. 34, p. 2101726, 2021.
- [187] J. Hao *et al.*, "Designing dendrite-free zinc anodes for advanced aqueous zinc batteries," *Advanced Functional Materials*, vol. 30, no. 30, p. 2001263, 2020.
- [188] M. Chamoun *et al.*, "Hyper-dendritic nanoporous zinc foam anodes," *NPG Asia Materials*, vol. 7, no. 4, pp. e178-e178, 2015/04/01 2015.
- [189] Y. Jiao *et al.*, "Engineering polymer glue towards 90% zinc utilization for 1000 hours to make high-performance Zn-ion batteries," *Advanced Functional Materials*, vol. 31, no. 49, p. 2107652, 2021.
- [190] A. Bayaguud, X. Luo, Y. Fu, and C. Zhu, "Cationic surfactant-type electrolyte additive enables three-dimensional dendrite-free zinc anode for stable zinc-ion batteries," *ACS Energy Letters*, vol. 5, no. 9, pp. 3012-3020, 2020/09/11 2020.
- [191] X. Guo *et al.*, "Alleviation of dendrite formation on zinc anodes via electrolyte additives," *ACS Energy Letters*, vol. 6, no. 2, pp. 395-403, 2021/02/12 2021.
- [192] K. Zhao *et al.*, "Stabilizing zinc electrodes with a vanillin additive in mild aqueous electrolytes," *ACS Applied Materials & Interfaces*, vol. 13, no. 40, pp. 47650-47658, 2021/10/13 2021.
- [193] Q. Zhang *et al.*, "The three-dimensional dendrite-free zinc anode on a copper mesh with a zinc-oriented polyacrylamide electrolyte additive," *Angewandte Chemie International Edition*, vol. 58, no. 44, pp. 15841-15847, 2019.



- [194] W. Lu, C. Zhang, H. Zhang, and X. Li, "Anode for zinc-based batteries: Challenges, strategies, and prospects," *ACS Energy Letters*, vol. 6, no. 8, pp. 2765-2785, 2021/08/13 2021.
- [195] G. Zhang *et al.*, "Rich alkali ions preintercalated vanadium oxides for durable and fast zinc-ion storage," *ACS Energy Letters*, vol. 6, no. 6, pp. 2111-2120, 2021/06/11 2021.
- [196] Y. Zhao *et al.*, "Inhibiting grain pulverization and sulfur dissolution of bismuth sulfide by ionic liquid enhanced poly(3,4-ethylenedioxythiophene):poly(styrenesulfonate) for high-performance zinc-ion batteries," *ACS Nano*, vol. 13, no. 6, pp. 7270-7280, 2019/06/25 2019.
- [197] D. Li, L. Cao, T. Deng, S. Liu, and C. Wang, "Design of a solid electrolyte interphase for aqueous Zn batteries," *Angewandte Chemie International Edition*, vol. 60, no. 23, pp. 13035-13041, 2021.

## CURRICULUM VITAE

### EDUCATION

**South Dakota State University**, Brookings, SD

Ph.D. in electrical Engineering Jan. 2019 – May. 2023

**University of Chinese Academy of Sciences**, Beijing, China

M.S. in Materials Physics and Chemistry Sep. 2013 – Jun. 2016

**Zhejiang University**, Hangzhou, China

B.E. in Materials Science and Engineering Aug. 2009 – Jul. 2013

### PUBLICATIONS

[1] **W. He**, Y. Ren, B. S. Lamsal, P. Kharel, J. Pokharel, J. J. Wu, Y. Cao and Y. Zhou (2023). "Decreasing water activity using the tetrahydrofuran electrolyte additive for highly reversible aqueous zinc metal batteries." ACS Applied Materials & Interfaces, vol. 15, no. 5, pp. 6647-6656, 2023.

[2] **W. He**, K. Chen, R. Pathak, M. Hummel, B. S. Lamsal, Z. Gu, P. Kharel, J. J. Wu and Y. Zhou (2021). "Achieving high pseudocapacitance anode by an in situ nanocrystallization strategy for ultrastable sodium-ion batteries." ACS Applied Materials & Interfaces, vol. 13, no. 19, pp. 22577-22585, 2021.

[3] **W. He**, K. Chen, R. Pathak, M. Hummel, K. M. Reza, N. Ghimire, J. Pokharel, S. Lu, Z. Gu and Q. Qiao (2021). "High-mass-loading Sn-based anode boosted by

pseudocapacitance for long-life sodium-ion batteries." *Chemical Engineering Journal* 414: 128638.

[4] **W. He**, Y. Liang, H. Tian, S. Zhang, Z. Meng and W.-Q. Han (2017). "A facile in situ synthesis of nanocrystal-FeSi-embedded Si/SiO<sub>x</sub> anode for long-cycle-life lithium ion batteries." *Energy Storage Materials* 8, 119-126.

[5] **W. He**, H. Tian, X. Wang, F. Xin and W. Han (2015). "Three-dimensional interconnected network GeO<sub>x</sub>/multi-wall CNT composite spheres as high-performance anodes for lithium ion batteries." *Journal of Materials Chemistry A* 3(38): 19393-19401.

[6] **W. He**, H. Tian, F. Xin and W. Han (2015). "Scalable fabrication of micro-sized bulk porous Si from Fe–Si alloy as a high performance anode for lithium-ion batteries." *Journal of Materials Chemistry A* 3(35): 17956-17962.

[7] **W. He**, H. Tian, S. Zhang, H. Ying, Z. Meng and W. Han (2017). "Scalable synthesis of Si/C anode enhanced by FeSi<sub>x</sub> nanoparticles from low-cost ferrosilicon for lithium-ion batteries." *Journal of Power Sources* 353: 270-276.

[8] Pathak, R., K. Chen, A. Gurung, K. M. Reza, B. Bahrami, J. Pokharel, A. Baniya, **W. He**, F. Wu and Y. Zhou (2020). "Fluorinated hybrid solid-electrolyte-interphase for dendrite-free lithium deposition." *Nature communications* 11(1): 1-10.

[9] Chen, K., R. Pathak, A. Gurung, K. M. Reza, N. Ghimire, J. Pokharel, A. Baniya, **W. He**, J. J. Wu and Q. Q. Qiao (2020). "A copper-clad lithiophilic current collector for dendrite-free lithium metal anodes." *Journal of Materials Chemistry A* 8(4): 1911-1919.

[10] Meng, Z., H. Tian, S. Zhang, X. Yan, H. Ying, **W. He**, C. Liang, W. Zhang, X. Hou and W.-Q. Han (2018). "Polyiodide-Shuttle restricting polymer cathode for rechargeable lithium/iodine battery with ultralong cycle life." ACS applied materials & interfaces 10(21): 17933-17941.

[11] Pokharel, J., A. Gurung, A. Baniya, **W. He**, K. Chen, R. Pathak, B. S. Lamsal, N. Ghimire and Y. Zhou (2021). "MOF-derived hierarchical carbon network as an extremely-high-performance supercapacitor electrode." Electrochimica Acta 394: 139058.

[12] Tian, H., S. Zhang, Z. Meng, **W. He** and W.-Q. Han (2017). "Rechargeable aluminum/iodine battery redox chemistry in ionic liquid electrolyte." ACS Energy Letters 2(5): 1170-1176.

## **BOOK CHAPTER**

- K. Chen, R. Pathak, **W. He** and Y. Zhou. "Composite lithium metal anodes for solid-state battery applications." Green Sustainable Process for Chemical and Environmental Engineering and Science (pp. 81-92), 2022

## **CONFERENCE PRESENTATIONS**

- **He, W.**; Zhou, Y. Ultrastable Sn-based anode enabled by a self-nanocrystallization strategy for sodium-ion batteries. ECS Meeting Abstracts 2021, MA2021-01 (6), 387.